Lappeenranta
University of Technology

Janne Heikkinen

VIBRATIONS IN ROTATING MACHINERY ARISING FROM MINOR IMPERFECTIONS IN COMPONENT GEOMETRIES

Thesis for the degree of Doctor of Science (Technology) to be presented with due permission for public examination and criticism in Auditorium 1383 at the Lappeenranta University of Technology, Lappeenranta, Finland on the 21th of November, 2014, at noon.

Acta Universitatis
Lappeenrantaensis 595

Supervisors Professor Aki Mikkola
Department of Mechanical Engineering
Lappeenranta University of Technology
Finland

Professor Jussi Sopanen
Department of Mechanical Engineering
Lappeenranta University of Technology
Finland

Reviewers Professor Arend L. Schwab
Mechanical Engineering (3mE)
Delft University of Technology
The Netherlands

Professor Pierangelo Masarati
Dipartimento di Ingegneria Aerospaziale
Politecnico di Milano
Italy

Opponents Professor Arend L. Schwab
Mechanical Engineering (3mE)
Delft University of Technology
The Netherlands

Professor Pierangelo Masarati
Dipartimento di Ingegneria Aerospaziale
Politecnico di Milano
Italy

ISBN 978-952-265-667-4
ISBN 978-952-265-668-1 (PDF)
ISSN-L 1456-4491
ISSN 1456-4491

Lappeenranta University of Technology
Yliopistopaino 2014

Abstract

Janne Heikkinen
Vibrations in Rotating Machinery Arising from Minor Imperfections in Component Geometries
Lappeenranta, 2014
110 pages

Acta Universitatis Lappeenrantaensis 595
Dissertation. Lappeenranta University of Technology

ISBN 978-952-265-667-4
ISBN 978-952-265-668-1 (PDF)
ISSN-L 1456-4491
ISSN 1456-4491

Vibrations in machines can cause noise, decrease the performance, or even damage the machine. Vibrations appear if there is a source of vibration that excites the system. In the worst case scenario, the excitation frequency coincides with the natural frequency of the machine causing resonance. Rotating machines are a machine type, where the excitation arises from the machine itself. The excitation originates from the mass imbalance in the rotating shaft, which always exists in machines that are manufactured using conventional methods. The excitation has a frequency that is dependent on the rotational speed of the machine. The rotating machines in industrial use are usually designed to rotate at a constant rotational speed, the case where the resonances can be easily avoided. However, the machines that have a varying operational speed are more problematic due to a wider range of frequencies that have to be avoided.

Vibrations, which frequencies equal to rotational speed frequency of the machine are widely studied and considered in the typical machine design process. This study concentrates on vibrations, which arise from the excitations having frequencies that are multiples of the rotational speed frequency. These vibrations take place when there are two or more excitation components in a revolution of a rotating shaft. The dissertation introduces four studies where three kinds of machines are experiencing vibrations caused by different excitations.

The first studied case is a directly driven permanent magnet generator used in a wind power plant. The electromagnetic properties of the generator cause harmonic excitations in the system. The dynamic responses of the generator are studied

using the multibody dynamics formulation. In another study, the finite element method is used to study the vibrations of a magnetic gear due to excitations, which frequencies equal to the rotational speed frequency. The objective is to study the effects of manufacturing and assembling inaccuracies. Particularly, the eccentricity of the rotating part with respect to non-rotating part is studied since the eccentric operation causes a force component in the direction of the shortest air gap. The third machine type is a tube roll of a paper machine, which is studied while the tube roll is supported using two different structures. These cases are studied using different formulations. In the first case, the tube roll is supported by spherical roller bearings, which have some wavinesses on the rolling surfaces. Wavinesses cause excitations to the tube roll, which starts to resonate at the frequency that is a half of the first natural frequency. The frequency is in the range where the machine normally operates. The tube roll is modeled using the finite element method and the bearings are modeled as nonlinear forces between the tube roll and the pedestals. In the second case studied, the tube roll is supported by freely rotating discs, which wavinesses are also measured. The above described phenomenon is captured as well in this case, but the simulation methodology is based on the flexible multibody dynamics formulation. The simulation models that are used in both of the last two cases studied are verified by measuring the actual devices and comparing the simulated and measured results. The results show good agreement.

Keywords: Permanent magnet machine, Vibration, Subcritical vibration, Multibody dynamics, Simulation

UDC 534.1:534.4:629.3.027:519.62:621.314.24:004.942

Tiivistelmä

Janne Heikkinen
Pienten geometristen epätarkkuuksien aiheuttamat värähtelyt pyörivissä koneissa
Lappeenranta, 2014
110 sivua

Acta Universitatis Lappeenrantaensis 595
Väitöskirja. Lappeenrannan teknillinen yliopisto

ISBN 978-952-265-667-4
ISBN 978-952-265-668-1 (PDF)
ISSN-L 1456-4491
ISSN 1456-4491

Koneiden käytönaikaiset värähtelyt voivat aiheuttaa melua, suorituskyvyn heikkenemistä tai pahimmillaan jopa koneen vikaantumisen. Koneiden värähtelyt vaativat värähtelylähteen, joka herättää koneen värähtelemään. Pahimmillaan heräte sopivalla taajuudella johtaa koneen resonointiin, joka tarkoittaa värähtelyä koneen ominaistaajuudella. Pyörivät koneet on konetyyppi, jossa heräte värähtelyyn on poikkeuksetta olemassa koneessa itsessään. Heräte syntyy pienestä massaepäkeskisyydestä, joka aiheuttaa koneen pyörimisnopeudesta riippuvan pyörivän voimakomponentin. Tämä herätekomponentti voi sattua samalle taajuudelle koneen ominaistaajuuden kanssa, jolloin yksittäinen komponentti ja sitä kautta koko kone alkaa värähdellä. Usein teollisuuskäytössä olevat koneet on suunniteltu pyörimään vakionopeudella, jolloin käytönaikaiset resonanssit on helppo välttää. Sen sijaan koneet, joiden pyörimisnopeus vaihtelee käytön mukaan, ovat hankalampia laajemman pyörimisnopeusalueen ja sitä kautta laajemman herätetaajuusalueen vuoksi.

Koneiden pyörimisnopeutta vastaavat värähtelyt on laajasti tutkittu aihe ja näitä värähtelyjä osataan välttää koneensuunnittelussa. Tässä tutkimuksessa perehdytään tarkemmin värähtelyihin, jotka syntyvät herätteistä, joiden taajuudet ovat pyörimisnopeutta vastaavan taajuuden monikertoja. Nämä taajuudet syntyvät, kun koneen yhden pyörähdyksen aikana vaihtuva voimakomponentti vaikuttaa koneeseen kahdesti tai useammin. Väitöskirjassa esitellään neljä tutkittua tapausta kolmesta erityyppisestä koneesta, joissa eri herätteet aiheuttavat koneiden käytönaikaisia värähtelyjä.

Ensimmäinen konetyyppi on tuulivoimalan suoravetoinen kestomagneettigeneraattori, jonka sähkömagneettisista ominaisuuksista syntyy käytön aikana herätteitä, joiden taajuus on pyörimisnopeuden monikertoja. Analysoinnissa käytetään monikappaledynamiikkaa, jonka avulla tutkitaan generaattorin sähkömagneettisista herätteistä syntyvien värähtelyiden vasteita. Toisessa tutkimuksessa tutkitaan pyörimisnopeutta vastaavalla taajuudella syntyvästä herätteestä aiheutuvia värähtelyitä kestomagneettivaihteen vasteessa elementtimenetelmän keinoin. Tutkimuksessa simuloidaan valmistus- ja asennusepätarkkuuksista aiheutuvaa epäkeskisyyttä koneen pyörivän osan ja pyörimättömän osan välillä, joka aiheuttaa voimakomponentin pienimmän komponenttien välillä olevan etäisyyden suuntaan. Kolmantena konetyyppinä on paperikoneen putkimainen tela, jota tutkitaan, kun se on tuettuna kahdella eri tuentatavalla. Kumpaakin tuentatapaa tutkitaan eri mallinnusmenetelmällä. Ensimmäisessä tapauksessa tela on tuettu pallomaisilla rullalaakereilla, joiden laakerikehillä on mitattu pientä aaltomaisuutta. Laakerin aaltomaisuus aiheuttaa herätteitä pyörivälle telalle, joka alkaa värähdellä resonanssissa taajuudella, joka on puolet telan ensimmäisestä ominaistaajuudesta, ja joka on koneen käytönaikasella pyörimisnopeusaluetta vastaavalla taajuusalueella. Tela mallinnetaan elementtimenetelmällä ja laakerit mallinnetaan epälineaarisin jousin telan ja tuennan välissä. Toisessa tapauksessa tela on tuettu yksinkertaisilla vapaasti pyörivillä kiekoilla, joiden aaltomaisuus on mitattu laakereiden tapaan. Edellä kuvattu värähtelyilmiö saadaan simuloitua tässä tapauksessa käyttäen mallinnusmenetelmänä joustavaa monikappaledynamiikka. Molemmat paperikoneen telan simulointimallit on verifioitu suorittamalla mittaukset olemassa oleville koelaitteille ja vertailemalla simuloituja tuloksia mitattuihin.

Hakusanat: Kestomagneettikone, Värähtely, Alikriittinen värähtely, Monikappaledynamiikka, Simulointi

UDC 534.1:534.4:629.3.027:519.62:621.314.24:004.942

Preface

The research work of this thesis was carried out during the years 2010–2014 in the laboratory of Machine Design at Lappeenranta University of Technology, and in the Turbomachinery Laboratory at Texas A&M University, TX, USA. The research was funded by the Doctoral Program of Concurrent Mechanical Engineering (DPCME) among other funding from industrial and Tekes-projects.

Acknowledgements

First of all I want to thank Professor Aki Mikkola for offering me a possibility to join the community of multibody dynamics for pursuing the doctoral degree. I admire your actions to promote our team and Lappeenranta University of Technology in your incredibly wide and top-level network.

I express my gratuity also for Professor Jussi Sopanen whose contribution in the field of rotating machinery was a solid base for this research project. The continuous, respectful support and guidance of both professors indicated a clear path to follow from the very beginning to the point where I am at the moment.

The comments by the preliminary examiners and also the opponents of the public examination, Professor Pierangelo Masarati from Politecnico di Milano, and Professor Arend L. Schwab from Delft University of Technology, are highly appreciated.

I want to thank Professor Dara W. Child from Texas A&M University for hosting my research exchange in one of the top league research groups in the field of rotor dynamics and Mr. Siavash Pakdelian from Texas A&M University for collaboration in the research project.

Thanks to all the members of Laboratory of Machine Design over the years. I feel privileged to be part of this particular research group. Special thanks to Mr. R. Scott Semken for the mind-opening discussions over the years. The contribution of members of Laboratory of Electrical Drives is also acknowledged.

The research project and the life at the university in general are supported by number of people. I want to express my deepest gratuities to the ladies who are and were always willing to help in a straightforward manner: Eeva Häyrinen, Anna-Kaisa Partanen, and Kaija Tammelin.

The financial support of LUT foundation, Walter Ahlström foundation, and The Finnish Association of Consulting Firms SKOL is highly acknowledged.

I will be eternally grateful to my parents and sisters for offering me a stable, supporting, and loving home. Thanks for my friends for all the unforgettable moments with barrels of beer and tons of meat. Noora, the mother of my child, without you I wouldn't be where I am. You made it all possible and I am grateful for your love and support through our years. Finally, Nuutti, my son, my life would be joyless and grey without your unconditional love, respect and admiration.

Lappeenranta, November 2014

Janne Heikkinen

Symbols

$\mathbf{0}$	Zero matrix
a_e	Semi-major axis
A	Cross section area
A_L	Loaded distance
A_0	Initial distance between the inner and outer raceway curvature centers
$\mathbf{A}^i$	Rotation matrix of body i
$\boldsymbol{a}$	Coefficent vector
b_c	Semi-width of contact between two cylinders
b_e	Semi-minor axis
$\boldsymbol{b}$	Coefficent vector
B	Magnetic flux density
B_B	Bearing width
$\mathbf{B}$	Second partial derivate of the shape matrix $\mathbf{N}$
$\boldsymbol{B}$	Magnetic field
c_c^{max}	Maximum damping constant
c_d	Bearing clearance
c_i	Damping coefficient
c_k	Amplitude of roundness error
C_p	Power coefficent of a turbine blade
$\mathbf{C}$	Damping matrix
$\mathbf{C}_F$	Full damping matrix containing damping and gyroscopic matrices
$\mathbf{C}_g$	Gyroscopic matrix
$\mathbf{C}_m$	Modal damping matrix
$\mathbf{C}_{\boldsymbol{q}}$	Jacobian matrix
$\boldsymbol{C}$	Vector of constraints
d	Diameter
d_c	Penetration depth when the maximum damping constant, c_c^{max}, is achieved
d_e	Pitch diameter
d_r	Roller diameter
d_s	Distance between race surfaces
D_i	Diameter of cylinder i
$\mathbf{D}$	First partial derivate of the shape matrix $\mathbf{N}$
$e_{x,y,z}$	Displacement in xyz-coordinate system
e_c	Exponent of the force-deflection relationship
E	Young's modulus

E'	Effective modulus of elasticity
$\boldsymbol{E}$	Electric field
f	Frequency
f_s	Rotational speed frequency
F	Force
F_c	Contact force
F_{cn}	Normal load
F_{cj}^i	Contact force for roller i in row j
F_{rad}	Radial force
F_{tan}	Tangential force
F_{ax}	Axial force
F_{sh}	Shear force
F^b	Total bearing force
$\boldsymbol{F}$	Force vector
$\boldsymbol{F}_{EM}$	Electromagnetic force vector
$\boldsymbol{F}_g$	Gravitational force vector
$\boldsymbol{F}^i$	External force vector
$\boldsymbol{F}_m$	Modal force vector
G	Gear ratio
$\bar{\mathbf{G}}^i$	Transformation matrix of body i
$\mathbf{I}$	Identity matrix
I_d	Transverse moment of inertia
I_p	Polar moment of inertia
J_i	Inertia of ith body
k	Number of harmonic order
k_c	Stiffness coefficient
k_e	Elliptic parameter
k_i	Stiffness of body i
$\mathbf{K}$	Stiffness matrix
$\mathbf{K}_m$	Mass normalized stiffness matrix
l	Length
l_r	Length of needle in needle roller bearing
L	Lagrangian
L_i	Length of cylinder i
m	Mass of the rotor
m_{mg}	Magnet mass
m_{ub}	Mass unbalance
$\mathbf{M}$	Mass matrix
$\mathbf{M}_m$	Mass normalized mass matrix
n_z	Number of rows in bearings
N	Number of rolling elements in each row

$\mathbf{N}$	Shape matrix
O-1	Inner raceway curvature center
O-2	Outer raceway curvature center
p	Number of poles
$\boldsymbol{p}^i$	Vector of modal coordinates of body i
$\dot{\boldsymbol{p}}^i$	First time derivative of modal coordinates of body i
P	Particle in a body
P_w	Power
q	Electric charge
$\boldsymbol{q}$	Vector of generalized coordinates
$\dot{\boldsymbol{q}}$	First time derivative of generalized coordinates
$\ddot{\boldsymbol{q}}$	Second time derivative of generalized coordinates
$\boldsymbol{Q}$	Mass unbalance vector
$\boldsymbol{Q}_e$	Vector of generalized external forces
$\boldsymbol{Q}_E$	Force vector that includes the descriptions of both conservative and non-conservative forces
$\boldsymbol{Q}_v$	Quadratic velocity vector
r	Radius
r_r	Radius of the roller sphericality
r_{rot}	Rotor radius
r_t	Turbine radius
$\boldsymbol{r}^i$	Location of particle in body i
$\dot{\boldsymbol{r}}^{iP}$	Velocity of particle P in body i
R	Curvature sum
R_d	Curvature difference
R_x	Effective radii of curvature in the principal x plane
R_y	Effective radii of curvature in the principal y plane
$\boldsymbol{R}^i$	Translation vector of local coordinate system of body i
$\dot{\boldsymbol{R}}^i$	First time derivative of the translational coordinates of the reference frame of body i
t	Time
T	Kinetic energy
T_q	Torque
$\boldsymbol{T}_d$	Dynamic torque vector
T_d	Dynamic torque of node i
T_n	Rated torque
$\boldsymbol{T}_s$	Vector containing excitation torque amplitudes
T_w	Torque from wind
$\bar{\boldsymbol{u}}_0^i$	Position vector of a particle in undeformed body in local frame
$\bar{\boldsymbol{u}}_f^i$	Position vector of a particle in deformed body from the initial position of a particle in undeformed body in local frame

$\bar{\boldsymbol{u}}^i$	Position vector of a particle in deformed body in local frame
$\tilde{\bar{\boldsymbol{u}}}^i$	Skew symmetric form of a displacement vector $\bar{\boldsymbol{u}}^i$
v	Velocity
v_w	Wind speed
$\boldsymbol{v}_c$	Velocity vector of conductor
V	Potential energy
x_c	Distance between contacting bodies
x_{c0}	Contact distance
X_i	Response amplitude
$\boldsymbol{X}$	Vector of response amplitudes
z	Number of needles in needle roller bearing

Greek letters

α	Initial angular position of the unbalance mass from the positive x-axis
β	Coefficient
β_j^i	Attitude angle of roller i in row j
γ	Attitude angle of rolling element
Δx	Relation between contact distance and distance between contacting bodies due to penetration
δ_{zj}^i	Displacement for roller i in row j in axial direction
δ_{rj}^i	Displacement for roller i in row j in radial direction
δ_0	Total deflection between roller and race
δ_{cc}	Total deflection between two cylinders
$\delta_{w_j^i}$	Elastic deformation of a rolling element i in row j in a bearing having some roundness error
$\delta_{\beta_j^i}$	Elastic deformation of a rolling element i in row j in a bearing
ζ	Second kind of elliptic integral
θ	Rotational degree of freedom
θ_x	Rotation of a body about x-axis
θ_y	Rotation of a body about y-axis
$\boldsymbol{\theta}^i$	Vector of generalized orientation coordinates
$\dot{\boldsymbol{\theta}}^i$	First time derivative of the orientation coordinates of the reference frame of body i
θ_w	Blade pitch angle
$\boldsymbol{\lambda}$	Vector of Lagrange multipliers
λ_w	Tip speed ratio
μ_0	Vacuum permeability
μ_r	Relative permeability
ν	Poisson's ratio

ρ	Mass density
ϕ_i	Phase angle
ϕ_j^i	Loaded contact angle of roller i in row j
ϕ_{aux}	Auxiliary angle
ϕ_0	Free contact angle
ϕ_k	Phase angle of the roundness error of k^{th} order
$\boldsymbol{\phi}_i$	Mode shape vector of mode i
$\boldsymbol{\Phi}$	Mode shape matrix
$\boldsymbol{\Phi}_n$	Mass normalized mode matrix
τ_p	Pole pitch
ω_f	Angular frequency of the excitation torque
$\bar{\omega}^i$	Angular velocity of a body i
ω_i	Angular eigenfrequency of mode i
Ω	Angular velocity
ξ	First kind of elliptic integral
ξ_i	Damping factor of mode i

Abbreviations

CAD	Computer Aided Design
DAE	Differential Algebraic Equation
DD	Directly Driven
DOF	Degrees of Freedom
EOM	Equation of Motion
FEM	Finite Element Method
FFRF	Floating Frame of Reference Formulation
FFT	Fast Fourier Transform
ODE	Ordinary Differential Equation
PM	Permanent Magnet
PMSG	Permanent Magnet Synchronous Generator
SRB	Spherical Roller Bearing
TROMAG	Trans-Rotary Magnetic Gear

Luku 1

Introduction

A complete rotating machine consists of several components from the rotating rotor shaft and bearings (Figure 1.1) to the supporting structure. Traditionally single components of the drive train are analyzed separately. However, all of these components affect the overall performance of the machine and all of the interactions between individual components have to be considered when analyzing results.

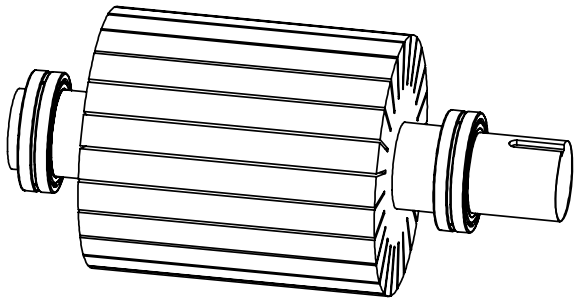

Kuva 1.1. Simplified sketch of a conventional slotted electric machine rotor with bearings and key slot

Multiple methods have been developed over times to study the behavior of rotating machines. Rotating systems have their typical characteristics that differ from the non-rotating mechanisms and machines, which is the reason for separating the rotor dynamics into another branch of science. The special characteristics of rotating systems had already been investigated by the late 19^{th} century [7]. The research became more active in the early 20^{th} century [7] and the modeling methods were developed further.

The extensive research in the field of rotor dynamics set a basis for the development

of rotating machinery. The fundamentals of the rotor dynamics was studied in the last century and the recent research has focused on the applications and the special features of the rotating systems. The special field of rotor dynamics has inspired many researchers and research groups to develop their own software to study rotating systems. An extensively used modeling method in the software is the Finite Element Method (FEM). Some of the commercial Finite Element software packages such as ANSYS, have included the analysis of the rotor dynamics in their software product. In general, typical rotor dynamic analysis can be performed by using the existing commercial software. However, the commercial analysis tools have their boundary constraints regarding the modifications of the equations and some special types of analysis, particularly analysis in the time domain, may need some additional modifications that have to be implemented into the equations of motion.

1.1 Motivation for the Study

Building a rotating system, as with any other mechanical system, requires practical manufacturing and assembling methods. The commonly used manufacturing tolerances cause a number of imperfections in mechanical systems. The common imperfections are, for example, uneven mass or stiffness distribution of the rotor, geometric roundness errors, and the defects of the bearing rings or rolling elements. These kinds of imperfections are harmful since they can cause unwanted vibrations in the rotor system.

The vibrations can occur in the rotational speed frequency or multiples of it. The vibrations arising from the multiples of the rotational speed frequency can be referred to as superharmonic resonances. Superharmonic resonances are sometimes referred to as subcritical resonances since they occur at the subcritical rotational speed. In some applications, such as in paper machines, subcritical resonances are of practical significance since they may be within the operating speed range and can influence the quality of the final product. The resonances can be harmful for the rotating machine itself and might lead into dynamic critical responses. Imperfections in the system may cause mechanical excitations through contacts. Additionally, the electromagnetic excitations may arise from the geometric inaccuracies that lead to unbalanced residual forces in the system. Electrical machines have excitations from the electromagnetic operation, *i.e.* rotor and stator harmonics, the frequencies of which are multiples of electrical frequency. All of the excitation frequencies, either mechanical or electrical are rotational speed dependent. This doctoral thesis introduces these excitations and their effect on the dynamic performance of the rotating systems by using different methods including the finite element method, and rigid and flexible multibody formulations.

1.2 Rotating Electric Machinery

Electrical machines have a long history. The first electrical motors were developed in the early 19^{th} century after the discovery of Ampère's force law by André-Marie Ampère in 1820. During the 20^{th} century, the induction electric machines became a standard industrial application. Recently, over the past three decades, more effort has been put into the development of Permanent Magnet (PM) machines due to the rapid development of rare earth magnetic materials. Permanent magnets have a feature that ensures that they remain magnetic once they are magnetized. Naturally, they have certain physical limits regarding the allowable temperature and external field currents.

The traditional induction machine has a magnetizing current in both rotor and stator. In a permanent magnet machine, the rotor is magnetized by permanent magnets. By using the permanent magnets, electrical losses due to magnetizing the rotor is prevented. Additionally, omitting the connecting brushes between rotor and stator, the mechanical losses can be reduced and wear on the rotor can be minimized. The drawback in using PM is that they are made out of rare earth materials that are expensive. The most commonly used magnetic material is Neodymium-Iron-Boron (NdFeB).

Permanent magnet electric machines are commonly used in high-end applications such as wind generators and traction motors. When compared with commonly used induction machines, PM machines are more expensive but have advantages such as a higher power/volume ratio, a higher power/mass ratio, and better efficiency [2, 83]. For these reasons, PM machines are used in applications where the size of the machine is limited but high performance is needed. In addition, PM machines are sustainable in terms of parameters and the variation of different parameters is wide without loss in efficiency or performance [4, 57].

1.3 Modeling of Rotating Systems

Rotor dynamics is a field of research that studies the rotating systems using theoretical description of rotating bodies. It differs from the conventional mechanical systems mostly due the rotational speed dependent gyroscopic effect. The typical features of rotor dynamics can be described using the analytical equations that have been developed over time, beginning from 1895 when Föppl published his study [7]. Simple rotor dynamics models are able to study some dynamic features with only a few Degrees of Freedom (DOF), which makes the analysis computationally efficient. However, the oversimplified model looses some accuracy and many times, especially in industrial needs, the analysis toolbox has to be widened to the finite element method. The description of the structure using the FEM is relative

accurate but computationally expensive. Other computational tools can be used to study the rotor dynamics such as rigid or flexible multibody system dynamics.

Traditionally, rotor dynamics is concentrated on rotor-bearing systems without imperfections. The main purpose is to calculate the critical rotational speeds and the stability in the rotational speed range of the machine, as well as study the steady state responses due to unbalanced excitations [59, 42]. The simplest systems are usually analyzed by using a *de Laval–Jeffcott* rotor model that has two lateral degrees of freedom [7]. Some typical characteristics needed in the analysis of rotor dynamics such as internal damping, and the dependence of critical speeds on the rotational frequency, can be taken into account when using the *de Laval–Jeffcott* model. The gyroscopic effect can be included in the inclination rotor model having two rotational degrees of freedom as presented in [33]. The four degrees of freedom model having two lateral and two rotational degrees of freedom gives a more accurate description of the model. However, for more complex analysis, a more accurate method is needed such as the above mentioned finite element method. When using the finite element formulation, rotary inertia, gyroscopic moments, the shear deformation of the shaft, the asymmetry of the rotor, and the bearings can be included in the analysis [50, 51]. The solution of steady state responses in a frequency domain requires the linearization of the nonlinear bearing components. For transient analysis, the finite element equations of motion are solved directly or by employing modal synthesis methods [39, 44] that can be used to decrease the degrees of freedom of the system.

The critical speeds and the stability regions have to be taken into account in the early design phase of rotating machines. In addition, the superharmonic vibrations of the rotor systems should be taken into consideration as well. Imperfections of the rotor are studied and, for example, the twice-running-speed response in horizontally mounted asymmetric rotors is well known [42, 38, 17]. Childs [9] studied the bearing ellipticity which excites the twice-running-speed vibrations. The eccentric operation of the rotor within the bearing clearance in local contact with the stator was studied by Ehrich [14]. Ehrich concluded that the excited rotor system at subcritical speed will respond by bouncing at its natural frequency and referred to the phenomenon as the subcritical superharmonic response. The subcritical superharmonic vibrations are related to the supercritical subharmonic vibrations that are studied for example in [8, 63]. Shi *et. al* [64] showed recently that a vertical rotor-bearing system generates sub-synchronous vibrations below twice-running-speed frequency if the motion of the rotor becomes unstable. However, in the horizontal arrangement when the rotational speeds are relatively low and the bearing loads high, the dynamic behavior of the bearings is almost linear.

Localized and distributed bearing defects in deep groove ball-bearings were studied by Sopanen and Mikkola [70, 71]. The waviness of the ball bearings including the gyroscopic and centrifugal forces were studied, for example, by Jang and Jeong [35,

37, 36]. An extensive study has been carried out by Harsha including investigations related to nonlinear dynamic analyses of ball and rolling-bearings under different conditions such as surface waviness and internal clearance effect [27, 24, 25, 26]. The effect of roller bearing waviness and radial clearance were studied by Liqin *et al.* [47]. Cao and Xiao studied surface waviness, radial clearance, surface defects, and loading conditions on the force and displacement responses of the Spherical Roller Bearing (SRB) system [6].

The effect of geometrical imperfection in electrical machines is well known and was already being studied in the 60's [74]. A severe and frequently occurring imperfection is the eccentricity of the rotor with respect to the stator. Eccentricity means that the air gap between the rotor and stator is uneven. Kim *et al.* [40] studied the dynamic response of the eccentric permanent magnet rotor in an analysis where the magnetic forces were coupled with the mechanical model. Boesing *et al.* [3] introduced a valid coupled analysis method to study the vibrations of a interior permanent magnet traction motor under natural electromagnetic excitations in run-up. Vibration characteristics of a high speed PM machine with an unbalanced magnetic pulling force and an eccentric mass force was studied by Fang *et al.* [15]. Dorrel investigated unbalanced magnetic pull of eccentric rotor in an induction motor in 1999 [13]. Tenhunen *et al.* studied extensively the electromechanical system of induction machines including the vibration response analysis [76, 77]. Van der Giet *et al.* compared 2D and 3D coupled electromagnetic and structural dynamics models of a switched reluctance machine [78] and concluded that the computationally less expensive 2D model meets the needed accuracy in most cases.

The economical aspects limits the manufacturing accuracy. The downside of the allowable levels of manufacturing and assembling inaccuracies is the vibration problems arising from the imperfections. The effects of manufacturing tolerances for a permanent magnet cogging torque are studied in [34, 18]. Manufacturing and assembling inaccuracies such as magnet dimension and placement irregularities, lamination anisotropies, stacking methods, rotor eccentricity, and air-gap variation are listed in these references. Coenen *et al.* [11] studied the effect of inaccuracies in permanent magnetic material on cogging torque. The influence of electric sheet metal part manufacturing processes on iron losses in induction machines was studied in [65]. It was shown that the stress zone along the cutting edge of the punching procedure increases the iron losses. The influence of the electrical steel grade on efficiency is studied in [41] where both large-scale low-speed and medium-scale semi-speed machines are modeled by using two electrical steel grades. The results show that the grade of electrical steel can remarkably affect the efficiency of the machine, which is one of the most important factors in the modern machine designing. However, the main function of the machines is to provide a long enough life cycle, which fulfills the customer requirements, and in order to do this it is an unconditional necessity to perform certain analyses, including vibration analysis.

1.4 Scientific Contribution

This doctoral dissertation introduces simulation methods that can be used to model rotating devices that contain imperfections from the manufacturing and assembling processes. The consequences of the imperfections fall into two categories: unbalanced electromagnetic forces that can cause rotating unbalanced residual force in the operation often leading to serious vibration problems, and the geometric inaccuracies such as bearing waviness that excite the rotating system to vibrate. These two categories are studied separately in the published international journal and conference proceedings. The vibrations of the electrical systems are studied in articles [30, 28]. The former presents torsional vibrations of a large-scale directly-driven permanent magnet synchronous wind generator that is modeled using four rotational degrees of freedom. The results indicate that the placing of the permanent magnets is an important design aspect that should be considered carefully. The latter introduces the characteristic vibrations of a permanent magnet gear that converts a low-speed, high-force translation into high-speed, low-torque rotation, or vice versa. The application can be used in wave energy harvesting. It is shown that the manufacturing and/or assembling inaccuracies that cause eccentric operation or roundness errors in the rotating parts can cause large unbalanced electromagnetic forces that may cause some vibration issues in the usage.

The other type of rotating machinery studied is the conventional rotating tube roll that is flexibly coupled to an actuator. The studies are presented in the articles [69, 28]. In both of these articles, the studied device is a paper machine tube roll. In the first study, the tube roll is supported by spherical roller bearings that have some roundness imperfections. Another study introduces the same tube roll, which is supported by disc structures at both ends of the roll. The roll is rolling on the imperfect discs that excites the tube roll to vibrate at subcritical rotational speeds. The simulation results of these studies are verified by comparing them with the measured results from a test rig. The simulation models are validated by measurements to describe the imperfections of the system, and show the existing subcritical vibrations in both cases.

1.4.1 Published Articles

This doctoral dissertation comprises the following publications:

- Heikkinen Janne, Sopanen Jussi, Ruuskanen Vesa, Nerg Janne, 2011, "Dynamic Analysis of a Direct-Driven Permanent Magnet Generator Drive Train Including Flexible Turbine Blades", *Proceedings of the ASME International Design Engineering Technical Conferences IDETC2011*, August 28–31, 2011, Washington, DC, USA

- Heikkinen Janne, Pakdelian Siavash, 2013, "Rotordynamics of a Trans-Rotary Magnetic Gear Rotor", *Proceedings of the ASME 2013 International Mechanical Engineering Congress & Exposition IMECE2013*, November 15–21, 2013, San Diego, CA, USA

- Sopanen Jussi, Heikkinen Janne, Mikkola Aki, 2013, "Experimental Verification of a Dynamic Model of a Tube Roll in Terms of Subcritical Superharmonic Vibrations", Mechanism and Machine Theory, Vol. 64, pp. 53–66

- Heikkinen Janne, Ghalamchi Behnam, Sopanen Jussi, Mikkola Aki, 2014, "Twice-Running-Speed Resonances of a Paper Machine Tube Roll Supported by Spherical Roller Bearings – Analysis and Comparison with Experiments", *Proceedings of the ASME International Design Engineering Technical Conferences IDETC2014*, August 17–20, 2014, Buffalo, NY, USA

The other published articles that falls apart from the core of the thesis.

- Lindh Pia, Heikkinen Janne, Kurvinen Emil, Pyrhönen Juha, Naumanen Ville, 2013, "The Multidisciplinary Design of Rotor Geometry in a Permanent Magnet Traction Motor", International Review of Electrical Engineering, Vol. 8, No. 5

- Lindh Pia, Pyrhönen Juha, Polikarpova Maria, Kurvinen Emil, Heikkinen Janne, Naumanen Ville, "Electrical and mechanical design of a PM traction motor with tooth coils," *15th European Conference on Power Electronics and Applications EPE 2013*, September 3–5, 2013, Lille, France

Luku 2

Rotating Machinery Modeling

A rotating system is a type of application in the family of mechanical systems. Rotating systems can be analyzed using many different methods. One of the methods is to use the traditional analytical rotor dynamics equations. Another option is to use the finite element method, which is able to describe the typical features of the rotating systems in a straightforward manner. A conventional multibody analysis approach can also be used, but it does not include the description of the flexibility of single bodies. By using more advanced and complex methodology in the multibody system analysis, the flexibility of the single components can be described.

The real-world continuous systems, in a mathematical sense, can be divided into an infinite number of differential particles. For this reason, simulation of the systems is based on the discretization of the systems into smaller components that can be numerically defined. The numerical components include certain information depending on the used approach. Simple and frequently used analytical descriptions of rotating systems are ones having 1) two lateral or rotational degrees of freedom, or 2) two lateral and two rotational degrees of freedom. The system having two lateral degrees of freedom is not able to describe the effect of gyroscopic effect in the system due to lack of description of rotational degrees of freedom. Using two rotational degrees of freedom or four degrees of freedom, two lateral and two rotational DOFs, overcomes this problem.

The finite element method is a traditional tool to analyze the structural mechanics and dynamics of the systems. It is also a frequently used method in analyzing rotating systems. The finite element model is defined using usually a large number of finite element that have structural properties and are attached to adjacent finite elements. All the finite elements together form a model that is a relatively accurate

description of the system. In dynamical problems, the finite element method is computationally expensive because of the high number of degrees of freedom that have to be solved. The number of elements in the system matrices increase with respect to the square of degrees of freedom. The dynamics of a system that has more than one body, can be solved when the individual bodies are constrained using the proper mathematical restrictions or special element types. Large and computationally expensive FE models can be optimized by using suitable element types, constrained degrees of freedom, or computational reduction tools.

The rigid multibody simulation approach is based on the concept of replacing the single bodies of the system by an equivalent mathematical model. The components describe the individual bodies of the system or appropriate parts of a single body. The bodies have masses, positions, and orientations that change due to the kinematics of the system. The relative displacement between bodies is defined using constrains that describe joints between bodies. The constrains are mathematical descriptions of the rejected kinematics of the bodies with respect to each other. The single bodies can be under external forces that affect them through the mechanical multibody system through the constrains. In the rigid multibody simulation approach, the external or internal forces do not affect the deformations of the body because each body, in a mathematical sense, is just a point that has a mass, an inertia, a position, and an orientation. The multibody simulation is an effective approach for studying the dynamics of large and complex systems. The analysis of the system that is described by a low number of rigid bodies is computationally efficient. The drawback is that the flexibility of a single body cannot be described, and therefore the accuracy of the results suffers. The rigid body approach cannot consider either the stresses or strains of the loaded system in a straightforward manner.

The base of all dynamic analyses is the Equation of Motion (EOM). The equation of motion can be expressed as follows

$$\mathbf{M}\ddot{\boldsymbol{q}} + \mathbf{C}\dot{\boldsymbol{q}} + \mathbf{K}\boldsymbol{q} = \boldsymbol{F}, \tag{2.1}$$

where $\boldsymbol{q}$ is the vector of generalized coordinates, $\dot{\boldsymbol{q}}$ and $\ddot{\boldsymbol{q}}$ are the first and the second time derivatives of vector of generalized coordinates, respectively, $\mathbf{M}$ is the mass matrix, $\mathbf{C}$ is the damping matrix, $\mathbf{K}$ is the stiffness matrix, and $\boldsymbol{F}$ is the force vector.

The above mentioned matrices can be formed using a number of methods. The structural properties of a single component can be evaluated or observed from measurements, Computer Aided Design (CAD) software, using analytical formulas, or modeling the structure using finite element method, to name a few commonly used methods. Discretization of the model makes the analysis computationally

more efficient but on the other hand some structural properties are lost. The performer of the analysis has to make the decision of the level of discretization and the usable modeling methodology in each particular case.

As an example, the matrices of a rotational four degrees of freedom system are presented. The matrices of this particular system are presented for two reasons: 1) the matrices are small, simple, and easily understandable and 2) a similar kind of system is presented and analyzed in the Chapter 4. Figure 2.1 shows the simplified system having four rotational degrees of freedom. The vector of generalized coordinates $\boldsymbol{q}$ can now be written as vector of θ–angles.

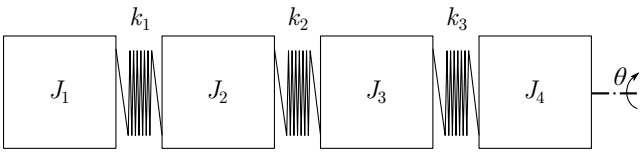

Kuva 2.1. Four degrees of freedom inertia-rotational spring-system

For the structure illustrated in Figure 2.1, the mass matrix $\mathbf{M}$ and the stiffness matrix $\mathbf{K}$ are as follows

$$\mathbf{M} = \begin{bmatrix} J_1 & 0 & 0 & 0 \\ 0 & J_2 & 0 & 0 \\ 0 & 0 & J_3 & 0 \\ 0 & 0 & 0 & J_4 \end{bmatrix} \text{ and} \tag{2.2}$$

$$\mathbf{K} = \begin{bmatrix} k_1 & -k_1 & 0 & 0 \\ -k_1 & k_1 + k_2 & -k_2 & 0 \\ 0 & -k_2 & k_2 + k_3 & -k_3 \\ 0 & 0 & -k_3 & k_3 \end{bmatrix}. \tag{2.3}$$

The determination of the damping matrix $\mathbf{C}$ is not as straightforward as in the case of the mass and stiffness matrices. The damping matrix can be determined using estimated modal damping factors. In this procedure, the undamped eigenvalues and modes of the system must be solved from equation

$$\left(\mathbf{K} - \omega_i^2 \mathbf{M}\right) \boldsymbol{\phi}_i = 0, \tag{2.4}$$

where ω_i is the angular eigenfrequency and $\boldsymbol{\phi}_i$ is the mode shape vector of mode i. The studied structure contains four degrees of freedom and, therefore, four modes can be solved. Without any constrains, the first mode is a rigid body mode with zero frequency. The other three modes are elastic modes with non-zero frequencies.

The mode shape matrix $\mathbf{\Phi}$ can be constructed using the solved mode shape vectors as follows

$$\mathbf{\Phi} = \begin{bmatrix} \boldsymbol{\phi}_1 & \boldsymbol{\phi}_2 & \boldsymbol{\phi}_3 & \boldsymbol{\phi}_4 \end{bmatrix}. \tag{2.5}$$

The system matrices can be mass normalized using the mass normalized modes. In the mass normalization, the mode matrix becomes

$$\mathbf{\Phi}_n = \frac{\mathbf{\Phi}}{\sqrt{\mathbf{\Phi}^{\mathrm{T}}\mathbf{M}\mathbf{\Phi}}}. \tag{2.6}$$

The mass normalized mode matrix $\mathbf{\Phi}_n$ can be now used for normalizing all the system matrices. This can be done for computational reasons: the mass matrix becomes an identity matrix $\mathbf{I}$ and the stiffness matrix becomes a diagonal matrix. The mass normalized mass matrix can be formed as follows

$$\mathbf{M}_m = \mathbf{\Phi}_n^{\mathrm{T}}\mathbf{M}\mathbf{\Phi}_n. \tag{2.7}$$

The corresponding modal stiffness matrix is as follows

$$\mathbf{K}_m = \mathbf{\Phi}_n^{\mathrm{T}}\mathbf{K}\mathbf{\Phi}_n. \tag{2.8}$$

The modal damping matrix $\mathbf{C}_m$ is now also a diagonal matrix, which can be formed using the damping factors ξ_i. The damping matrix elements, c_i, can be defined for the each mode i as follows

$$c_i = 2\xi_i\omega_i. \tag{2.9}$$

2.1 Rotor Dynamics

A rotor can be described using the commonly known Jeffcott rotor model that was widely studied by Jeffcott in 1919 [7]. However, the concept of the model was actually introduced in 1895 by Föppl in [7] where he referred to the model as the *de Laval* rotor. The model contains only two uncoupled degrees of freedom. The model is oversimplified, but it takes into consideration some typical quantitative features of the real rotors. For example, undamped and damped critical speeds, frequency responses and stability regions can be studied using the simple Jeffcott model. The model is practical, for example, in parametric studies [19].

The traditional Jeffcott rotor having two lateral degrees of freedom does not contain any information from the moments of inertia of the system that consequently

suppresses the gyroscopic effect. The gyroscopic moment affects the vibration characteristics by separating a vibration mode of a standing system to two separate spin speed dependent whirling modes: a backward and a forward whirling mode. A simple model that can be used to include the gyroscopic effect is the Jeffcott model having two rotational degrees of freedom. However, the lateral response of the system is lost. In order to study the vibration characteristics of the system, it is reasonable to use a four degrees of freedom model having two translational and two rotational degrees of freedom. Angular velocity around the centerline is taken into account as a parameter Ω in the equation of motion. The stiffness of the rotor system can be the stiffness of the massless shaft, stiffness of the support of a rigid rotor, or combination of these as presented in Figure 2.2 [19]. In the Figure 2.2, C is the geometric center of the shaft where the disc is located, and O is the center of the shaft when Ω is zero.

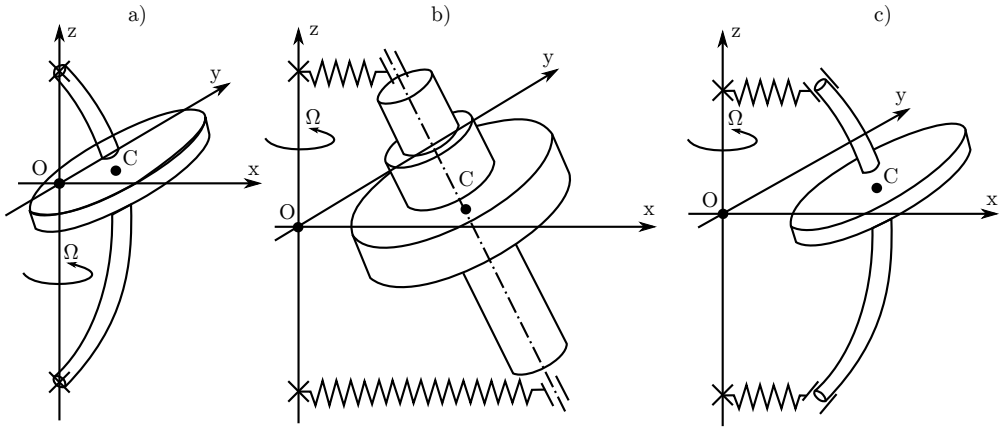

Kuva 2.2. A four degrees of freedom rotor system having a) a flexible massless shaft with a disc on rigid support, b) a rigid rotor on flexible support, and c) a massless flexible shaft with a rigid disc on flexible support.

The equation of motion of the above mentioned undamped 4 DOF system takes the following form

$$\mathbf{M}\ddot{\boldsymbol{q}} + \Omega\mathbf{C}_g\dot{\boldsymbol{q}} + \mathbf{K}\boldsymbol{q} = \boldsymbol{F}, \tag{2.10}$$

where $\mathbf{C}_g$ is the rotational speed dependent gyroscopic matrix.

The Equation 2.10 indicates that the rotational speed dependent gyroscopic moment causes an additional force that has to be compensated by the system. In the equation of motion of 4 DOF system (2.10), the mass matrix of the rotor can be constructed as follows

$$\mathbf{M} = \begin{bmatrix} m & 0 & 0 & 0 \\ 0 & m & 0 & 0 \\ 0 & 0 & I_d & 0 \\ 0 & 0 & 0 & I_d \end{bmatrix}, \tag{2.11}$$

where m is the mass of the rotor, and I_d is the transverse moment of inertia. Gyroscopic matrix can be written as

$$\mathbf{C}_g = \begin{bmatrix} 0 & 0 & 0 & 0 \\ 0 & 0 & 0 & 0 \\ 0 & 0 & 0 & I_p \\ 0 & 0 & -I_p & 0 \end{bmatrix}, \tag{2.12}$$

where I_p is the polar moment of inertia. In the stiffness matrix, the stiffness in x and y directions are uncoupled. Also the translational stiffness in xy-plane is uncoupled from the axial and torsional behavior. The translational stiffness in xz-plane can be derived from the displacements and forces in the xy-plane. Correspondingly the translational stiffness in yz-plane can be derived from the displacements and forces in the yz-plane. The stiffness matrix takes the following form

$$\mathbf{K} = \begin{bmatrix} K_{11} & 0 & 0 & K_{12} \\ 0 & K_{11} & -K_{12} & 0 \\ 0 & -K_{12} & K_{22} & 0 \\ K_{12} & 0 & 0 & K_{22} \end{bmatrix}, \tag{2.13}$$

where the components of the stiffness matrix can be formulated by some common method introduced in mechanical engineering handbooks. The opposite signs in cross-coupled terms in stiffness matrix become from the usage of the same stiffness elements in different coordinate planes. The vector of generalized coordinates in this particular case is as follows

$$\boldsymbol{q} = \begin{bmatrix} x \\ y \\ \theta_x \\ \theta_y \end{bmatrix}, \tag{2.14}$$

The forces on the right hand side of the Equation (2.10) contain the rotational speed dependent force from the unbalanced mass and other external forces such as gravity. The amplitude of the unbalanced mass force is proportional to the square of the angular velocity Ω^2 and the frequency is proportional to the angular velocity Ω. If the rotational speed is zero, the gyroscopic term and the unbalanced force disappears and the system is a regular, undamped four degrees of freedom system.

2.2 The Finite Element Method

The finite element method is frequently used in conventional structural analysis. FEM can be used also in dynamic analyses including rotor dynamic analysis. In rotor dynamics, the finite element method is a convenient method to describe complex real-world machinery. The finite element method divides the studied structure into sequences and elements that connect to other elements at points that are referred to as nodes. Nodes and elements form a mesh that is a discrete and relatively accurate description of the system.

Elements have certain features that have to be defined such as material and element type properties. The element types include all kinds of elements from single point mass elements to one degree of freedom rod elements; as well as two degree of freedom beam and plate elements to three dimensional shell and solid elements. Other special types of elements are, for example, spring elements, constrain elements, and contact elements. The accuracy as well as computational effort is dependent on the model description and thus the element type.

Element are formed using shape functions, which describe the element spatial properties such as cross-couplings of the element properties in different directions and continuity of the element mesh. Usually, beam elements are used in the rotor dynamics analysis. The element can be either two or three dimensional. In most system studies, the linear assumption of geometric displacements is appropriate and the shear deformations of the cross section are negligible.

The equations of motion for the rotating system running at constant rotational speed can be described in matrix form as follows [19].

$$\mathbf{M}\ddot{\boldsymbol{q}} + (\mathbf{C} + \Omega\mathbf{C_g})\dot{\boldsymbol{q}} + \mathbf{K}\boldsymbol{q} = \Omega^2\boldsymbol{Q} + \boldsymbol{F}, \tag{2.15}$$

where $\boldsymbol{Q}$ is the mass unbalance, and force vector $\boldsymbol{F}$ contains other forces such as gravity and bearing forces.

The mass matrix of certain beam elements can be formed using the shape matrix $\mathbf{N}$ as follows

$$\mathbf{M} = \rho A \int_0^L \mathbf{N}^{\mathrm{T}}\mathbf{N}dx, \tag{2.16}$$

where ρ is the mass density of the material and A is the cross section area. Accordingly, the stiffness matrix can be formed using the second partial derivative of the shape matrix $\mathbf{B} = \frac{\partial^2\mathbf{N}}{x^2}$ as follows

$$\mathbf{K} = EI_d \int_0^L \mathbf{B}^{\mathbf{T}}\mathbf{B}dx, \tag{2.17}$$

where E is the Young's modulus of the material. The gyroscopic matrix can be formed from the first partial derivative of the shape matrix $\mathbf{D} = \frac{\partial \mathbf{N}}{\partial x}$ as follows

$$\mathbf{C_g} = \frac{1}{2}\rho I_p \int_0^L \mathbf{D^T} \begin{bmatrix} 0 & 0 & 0 & 0 & 0 & 0 \\ 0 & 0 & 0 & 0 & 0 & 0 \\ 0 & 0 & 0 & 0 & 0 & 0 \\ 0 & 0 & 0 & 0 & 0 & 0 \\ 0 & 0 & 0 & 0 & 0 & 1 \\ 0 & 0 & 0 & 0 & -1 & 0 \end{bmatrix} \mathbf{D} dx. \tag{2.18}$$

The number of elements in matrices increase with respect to the square of DOFs. From a computational perspective, this is expensive and some methods are developed to overcome computational issues. One frequently used method is the modal reduction method where the flexibility of the system is described using the eigenmodes of the system. Eigenmodes describes the vibration characteristics that, in contrast, predict accurately the occurring deformations of the system.

In the finite element method, the matrices easily become very large. It is greatly beneficial to use the modal reduction method in which a limited number of the system eigenmodes are used to describe the structural properties of the model [39]. In this method, the matrices are defined using the mass normalized eigenmodes as introduced in the previous subsection. The number of eigenmodes can be different than the number of degrees of freedom. The main idea is to choose the eigenmodes that contribute most to the characteristic deformations of the system. They can be chosen, for example, based on the minimum relative strain energy of a single mode. Also, all the modes within double the operational frequency should be used. In general, the lowest frequency modes dominate and the higher modes do not contribute significantly to system response.

Vibration modes of the system can be obtained from the Equation (2.4) when proportional damping is assumed and the gyroscopic effects are ignored. The modal mass and stiffness matrices can be formed as presented in Equations (2.7) and (2.8).

The modal damping matrix can be formed using the mass normalized eigenmodes as follows

$$\mathbf{C}_m = \mathbf{\Phi}_n^{\mathrm{T}} \mathbf{C}_F \mathbf{\Phi}_n. \tag{2.19}$$

The full damping matrix $\mathbf{C}_F$ in Equation (2.19) contains the damping matrix $\mathbf{C}$ and the rotational speed dependent gyroscopic matrix $\mathbf{C_g}$. Since the gyroscopic matrix is omitted in the calculation of the eigenvalues in Equation (2.4), the modal gyroscopic matrix has off-diagonal terms. Off-diagonal terms reduce the

computational efficiency, but the reduced matrices are still computationally much more efficient than full matrices.

The modal force vector can be formed as follows

$$\boldsymbol{F}_m = \boldsymbol{\Phi}_n^{\mathrm{T}} \boldsymbol{F}. \tag{2.20}$$

The modal force vector, $\boldsymbol{F}_m$, contains all the force components that were introduced in Equation (2.15). The set of modal coordinates $\boldsymbol{p}_m$ can be formed using the reduced mode matrix and physical generalized coordinates $\boldsymbol{q}$ as follows

$$\boldsymbol{p}_m = \boldsymbol{\Phi}_n^{\mathrm{T}} \boldsymbol{q}. \tag{2.21}$$

The unbalance force components in x and y directions can be written as follows [43]

$$\begin{bmatrix} F_x \\ F_y \end{bmatrix} = m_{ub} r \Omega^2 \begin{bmatrix} \cos(\Omega t + \alpha) \\ \sin(\Omega t + \alpha) \end{bmatrix}, \tag{2.22}$$

where m_{ub} is the mass unbalance, r is the distance of the unbalance mass center to the rotating axis, and α is the initial angular position of the unbalance mass from the positive x-axis.

2.3 Flexible Multibody Dynamics

The flexibility of single bodies can be included in the multibody system analysis. The flexibility can be described, for example, using the vibration characteristics of the bodies. Natural frequencies and the mode shapes of the system are proportional to the flexibility of the body. The vibrations of a body can be solved using the finite element method and eigenvalue analysis. This analysis type results in eigenvalues and eigenmodes which are used in the description of the flexibility. The description of the flexible parts can then be included in the multibody model to improve the accuracy of the simulations. Additionally, deformations, stresses, and strains of a single body can be studied using certain computational tools.

Flexible multibody simulation provides a general approach to the rotor dynamics, and the limitations related to the bearing imperfections such as bearing clearance, bearing ring waviness, or bearing defects can be avoided. Therefore, complete rotor systems including flexible rotors, bearings, and the whole drive train system can be analyzed using the flexible multibody simulation approach. In modeling and analyzing the flexible rotors using the multibody simulation approach, the Floating Frame of Reference Formulation (FFRF) is commonly used method [62]. In the

floating frame of reference formulation, a large reference motion is described using a reference frame, and the deformation is described relative to the frame. The number of variables describing the deformation can be reduced using component mode synthesis, thus computational effort can be significantly reduced without an appreciable loss in accuracy.

In FFRF, deformation of a body is usually described by the superposition of the eigenmodes obtained from a finite element model by using an eigenvalue analysis (Eq. 2.4). The reference motion of the body can be described by the translation and rotation of the local coordinate system in the fixed global coordinate system. Figure 2.3 describes vectors that define the particle position in the global coordinate system. The global position of an arbitrary particle, P, in the flexible body, i, can be expressed as follows [62]

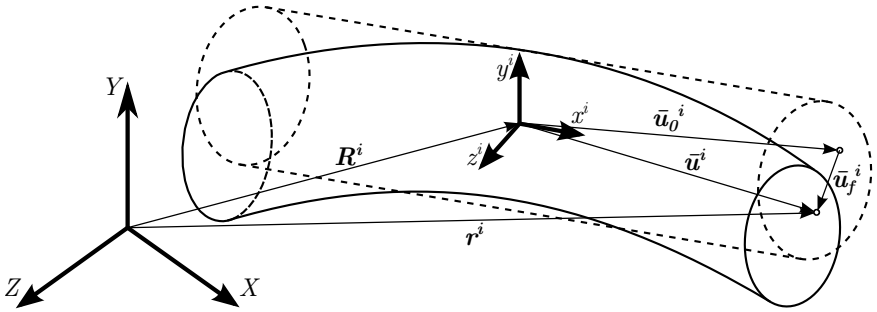

Kuva 2.3. Graphical presentation of defining the global position of an arbitrary particle in a deformed body

$$\boldsymbol{r}^i = \boldsymbol{R}^i + \mathbf{A}^i \left(\bar{\boldsymbol{u}}_0^i + \bar{\boldsymbol{u}}_f^i\right), \tag{2.23}$$

where $\boldsymbol{R}^i$ is translation of the local coordinate system of a body in global coordinate system, $\mathbf{A}^i$ is the rotational matrix of the local coordinate system, $\bar{\boldsymbol{u}}_0^i$ is the position vector that defines the undeformed position of the particle, P, and $\bar{\boldsymbol{u}}_f^i$ is the position vector that defines the deformation of the particle.

Flexible bodies have an infinite number of degrees of freedom that define the position of every particle in the body. For computational reasons, the deformation vector must be defined using a finite number of coordinates. This approximation can be carried out by using the Rayleigh-Ritz or finite element method. Using matrix formulation, the approximation of a deformation vector can be expressed as follows

$$\bar{\boldsymbol{u}}_f^i = \mathbf{N}^i \boldsymbol{p}^i, \tag{2.24}$$

where $\mathbf{N}^i$ is a shape matrix and $\boldsymbol{p}^i$ is the vector of modal coordinates of a body i.

Finite element shape functions compose the shape matrix $\mathbf{N}^i$ [62]. Real-world structures are rather complex and an accurate finite element model contains a large number of variables to be solved in computationally expensive dynamic analyses. For this reason, the complete finite element model is preferred in order to overcome this problem rather that process using methods, such as, sub-structuring or component mode synthesis. A frequently used sub-structuring method in the field of flexible multibody dynamics is the Craig-Bampton method [12]. In the Craig-Bampton method, the structure is separated into interior and boundary degrees of freedom and the so called Craig-Bampton modes are solved. These modes can be used in dynamic analysis in orthogonalized form.

The vector of generalized coordinates of the flexible body, i, can be written as follows

$$\boldsymbol{q} = \begin{bmatrix} \boldsymbol{R}^{i\,\mathrm{T}} & \boldsymbol{\theta}^{i\,\mathrm{T}} & \boldsymbol{p}^{i\,\mathrm{T}} \end{bmatrix}^{\mathrm{T}}, \tag{2.25}$$

where $\boldsymbol{\theta}^i$ is the vector of generalized orientation coordinates. The orientation of the body can described using commonly used Euler angles. Velocity vector of particle P can be obtained by differentiating the Equation (2.23) with respect to time and written in partitioned form as follows

$$\dot{\boldsymbol{r}}^i = \begin{bmatrix} \mathbf{I} & -\mathbf{A}^i \tilde{\bar{\mathbf{u}}}^i \bar{\mathbf{G}}^i & \mathbf{A}^i \boldsymbol{\Phi}^i \end{bmatrix} \begin{bmatrix} \dot{\boldsymbol{R}}^i \\ \dot{\boldsymbol{\theta}}^i \\ \dot{\boldsymbol{p}}^i \end{bmatrix}, \tag{2.26}$$

where $\mathbf{I}$ is the identity matrix, $\bar{\mathbf{G}}^i$ is the transformation matrix that relates angular velocity $\bar{\boldsymbol{\omega}}^i$ of a body and the first time derivative of body fixed Euler angles. $\tilde{\bar{\mathbf{u}}}^i$ is the skew symmetric matrix of vector $\bar{\boldsymbol{u}}^i$. The vector of first time derivatives of the generalized coordinates in the right hand side of the Equation (2.26) describes the velocity of a flexible body.

Dynamic analyses can be solved by using a Lagrangian method. The Lagrangian equation is as follows

$$\frac{d}{dt}\left(\frac{\partial L}{\partial \dot{\boldsymbol{q}}}\right) - \left(\frac{\partial L}{\partial \boldsymbol{q}}\right) + \mathbf{C}_{\boldsymbol{q}}^{\mathrm{T}} \boldsymbol{\lambda} = \boldsymbol{Q}_e \tag{2.27}$$

where $L = T - V$ is the Lagrangian, $\mathbf{C}_{\boldsymbol{q}}$ is the Jacobian matrix, $\boldsymbol{\lambda}$ is the vector of Lagrange multipliers and $\boldsymbol{Q}_e$ is the vector of the generalized external forces. If the Lagrangian, L, is substituted by equations of kinetic and potential energy, T and

V respectively, and the internal and external forces are taken into account, the equation of constrained motion is as follows

$$\mathbf{M}\ddot{\boldsymbol{q}} + \dot{\mathbf{M}}\dot{\boldsymbol{q}} - \frac{1}{2}\left[\frac{\partial}{\partial \boldsymbol{q}}\left(\dot{\boldsymbol{q}}^{\mathrm{T}}\mathbf{M}\dot{\boldsymbol{q}}\right)\right]^{\mathrm{T}} + \mathbf{K}\boldsymbol{q} + \boldsymbol{F}_g + \mathbf{C}\dot{\boldsymbol{q}} + \mathbf{C}_q^{\mathrm{T}}\boldsymbol{\lambda} = \boldsymbol{Q}_e, \tag{2.28}$$

where $\boldsymbol{F}_g$ is the gravitational force vector. Using the following expressions

$$\boldsymbol{Q}_v = -\dot{\mathbf{M}}\dot{\boldsymbol{q}} + \frac{1}{2}\left[\frac{\partial}{\partial \boldsymbol{q}}\left(\dot{\boldsymbol{q}}^{\mathrm{T}}\mathbf{M}\dot{\boldsymbol{q}}\right)\right]^{\mathrm{T}} \tag{2.29}$$

$$\boldsymbol{Q}_E = \boldsymbol{Q}_e - \mathbf{K}\boldsymbol{q} - \boldsymbol{F}_g - \mathbf{C}\dot{\boldsymbol{q}} \tag{2.30}$$

the equation of constrained motion can be written

$$\mathbf{M}\ddot{\boldsymbol{q}} + \mathbf{C}_{\boldsymbol{q}}^{\mathrm{T}}\boldsymbol{\lambda} = \boldsymbol{Q}_E + \boldsymbol{Q}_v. \tag{2.31}$$

The force vector $\boldsymbol{Q}_E$ is the force vector that includes the descriptions of both conservative and non-conservative forces, and $\boldsymbol{Q}_v$ is a vector of the quadratic velocity inertia forces that is a nonlinear function of the generalized coordinates and velocities of the system and it includes the gyroscopic and Coriolis forces.

In multibody dynamics, algebraic equations are used for the description of constraints between bodies. Constraint equations are expressed as follows

$$\boldsymbol{C}\left(\boldsymbol{q}, t\right) = 0, \tag{2.32}$$

where $\boldsymbol{C}$ is the vector of constraints of the system and t is time. Equations (2.31) and (2.32) form a set of Differential Algebraic Equations (DAE) which can be converted to Ordinary Differential Equations (ODE) to solve the dynamic response of the multibody system in the time domain.

In the floating frame of reference formulation, the reference frame describes large reference motions of a body. For this reason, the deformation modes cannot contain any rigid body motions, *i.e.*, motions where displacements occur without deformation. Unconstrained vibration modes have six rigid body modes that represent translations and rotations. These modes can be identified and removed from the eigenmode basis. Another option is to use the vibration modes of a fully constrained structure, such as the cantilever modes of beams. The selection of the deformation modes influences the motion that the reference coordinate system describes. In the case of unconstrained vibration modes, the reference coordinate

system is not rigidly attached to any physical point on a body, and the reference motion is the mean rigid body motion.

This leads to the mean axis frame, which is chosen in such a way that the linear and angular momenta due to deformation are zero [60, 1]. When constrained mode shapes are used, the reference coordinate system is rigidly attached to a specific physical point on a body. An important issue in selecting the deformation modes and reference coordinate system is that the modes defined in one reference coordinate system should not be used in another coordinate system [61]. This might cause difficulties when combining vibration modes and static correction modes, since these modes may be defined using different reference conditions. In the case of an unconstrained system, the description of local deformations caused by constraint forces or externally applied forces is difficult and requires a large number of vibration modes. Additional correction modes can be used as presented in [80, 16, 82].

2.4 Contact Force Calculation

Contact force calculation in simulation is typically based on the penetration of two bodies. The shape of the contact before penetration, when the bodies are just touching each other, is either a point or a line contact. The shapes of the contacting surfaces define the shape of the penetration. In the case of a rolling element being the second body in the penetration interaction, the shape can be, for example, a circle, a rectangle or an ellipse caused by a ball, a cylindrical roll, or a barrel shape roll, respectively, penetrating into a parallel cylindrical surface. The penetration depth, area of penetration surface and the velocity of the penetration define the contact force that counteracts the penetration and tries to push the penetrating bodies to the point or the line contact. Naturally, if the bodies are separated from each other, there is no contact force between.

There are few generated theories for calculation of contact forces. One of the commonly used contact definition methods is the Hertzian contact theory [31]. In the original publication, the contact areas and elastic deformations of two spheres in contact were defined. The theory makes some assumptions regarding the contact definition such as neglected adhesion, elastic deformations, small contact area, and perfectly smooth and frictionless surfaces. However, the theory is widely used and good estimate of the contact description in many cases.

The contact force F_c can be expressed as a function of the contact penetration and penetration velocity as follows [49]

$$F_c = \begin{cases} k_c \left(x_{c0} - x_c\right)^{e_c} - \dot{x_c} c_c^{max}, & x_c \leq x_{c0} - d_c \\ k_c \left(x_{c0} - x_c\right)^{e_c} - \dot{x_c} \left(c_c^{max} - c_c^{max} \left(\Delta x^2 \cdot (3 - 2\Delta x)\right)\right), & x_{c0} - d_c < x_c < x_{c0} \\ 0, & x_c \geq x_{c0} \end{cases}, \tag{2.33}$$

where k_c is the stiffness coefficient, x_{c0} is the contact distance, x_c is the distance between contacting bodies and e_c is the exponent of the force-deflection relationship. In order to avoid discontinuities in the contact force, three conditional equations are used. Parameter d_c is penetration depth when the maximum damping constant, c_c^{max}, is achieved. Δx is the relation between contact distance and distance between contacting bodies due to penetration which can be calculated as follows

$$\Delta x = \frac{x_c - x_{c0} + d_c}{d_c}. \tag{2.34}$$

Two parallel cylinders have a contact area that is rectangular. The force-deflection relationship can be solved from equations

$$b_c = \sqrt{\frac{4F_c \left(1 - \nu^2\right)}{\pi L_1 E} \left(\frac{1}{D_1} + \frac{1}{D_2}\right)^{-1}}, \text{ and} \tag{2.35}$$

$$\delta_{cc} = \frac{2\left(1 - \nu^2\right) F_c}{\pi L_1 E} \left(\frac{2}{3} + \ln \frac{4 D_1 D_2}{b_c^2}\right), \tag{2.36}$$

where b_c is the semi-width of contact and δ_{cc} is the total deflection between the cylinders. F_c is the contact force, L_1 is the length of the cylinder, ν and E are the Poisson's ratio and Young's modulus of the material, respectively, and D_1 and D_2 are the diameters of the cylinders in contact.

2.5 Dynamic Model of a Spherical Roller Bearing

Spherical roller bearings are seeing increasing industrial use due to features they offer such as high load capacity and self-aligning. Increasing attention has intensified the need to understand better the behaviors and dynamic performance of imperfect SRBs. Bearing defects are classified as 1) distributed defects, such as surface roughness, waviness, misaligned races, and off-size rolling elements; and as 2) local defects, such as cracks, pits, and spalls on the rolling surfaces [75, 73].

The simulations of complete machines require computationally efficient bearing calculation. Therefore, the proposed spherical roller bearing model has been simplified. It is assumed that no slipping or sliding occurs between the components

of the bearing that operates under isothermal conditions, and the inner raceway is rigidly fixed to the shaft. Rollers are positioned at an equal-pitched around the inner race and the centrifugal forces are not considered. In addition, there is no bending deformation of the raceways and only nonlinear Hertzian contact deformations are considered at the contacts formed between the rollers and raceways.

2.5.1 The Geometry of Contacting Elastic Solids

Two solids that have different radii of curvature in two directions are in point contact when no load is applied to them. When the two solids are pressed together by a force F, the contact area is elliptical. In the following analysis, it will be assumed that for convex surfaces the curvature is positive, but for concave surfaces the curvature is negative [23].

The geometry between two solids (A and B) in contact can be expressed in terms of the curvature sum R, and curvature difference R_d as follows [5, 22]

$$\frac{1}{R} = \frac{1}{R_x} + \frac{1}{R_y}, \text{ and} \tag{2.37}$$

$$R_d = R\left(\frac{1}{R_x} - \frac{1}{R_y}\right), \tag{2.38}$$

where

$$\frac{1}{R_x} = \frac{1}{r_{Ax}} + \frac{1}{r_{Bx}}, \tag{2.39}$$

$$\frac{1}{R_y} = \frac{1}{r_{Ay}} + \frac{1}{r_{By}}, \tag{2.40}$$

where A and B are corresponding to roller and race, respectively. The variables R_x and R_y represent the effective radii of curvature in the principal x and y planes. When the two solids have a normal load applied to them the result is that the point expands to an ellipse with a_e being a semi-major axis and b_e being the semi-minor axis. The elliptic parameter k_e is defined as [23]

$$k_e = \frac{a_e}{b_e}. \tag{2.41}$$

The elliptic parameter can be defined as a function of the curvature difference R_d and the elliptic integrals of the first ξ and second ζ kinds as [22]

$$k_e = \left[\frac{2\xi - \zeta\,(1 + R_d)}{\zeta\,(1 - R_d)}\right]^{1/2}, \tag{2.42}$$

where

$$\xi = \int_0^{\pi/2} \left[1 - \left(1 - \frac{1}{k_e^2}\right)\sin^2\phi_{aux}\right]^{-1/2} d\phi_{aux}, \text{ and} \tag{2.43}$$

$$\zeta = \int_0^{\pi/2} \left[1 - \left(1 - \frac{1}{k_e^2}\right)\sin^2\phi_{aux}\right]^{1/2} d\phi_{aux}, \tag{2.44}$$

where ϕ_{aux} is an auxiliary angle. Brewe and Hamrock [5] used numerical iteration and curve fitting techniques and found the following approximation formulas for the ellipticity parameter, k_e, and elliptical integrals of the first ξ and second ζ kind as shown below

$$k_e = 1.0339\left(\frac{R_y}{R_x}\right)^{0.6360}, \tag{2.45}$$

$$\xi = 1.0003 + 0.5968\frac{R_x}{R_y}, \tag{2.46}$$

$$\zeta = 1.5277 + 0.6023\ln\left(\frac{R_y}{R_x}\right). \tag{2.47}$$

2.5.2 Spherical Roller Bearing Geometry

The important geometrical dimensions of the spherical roller bearing are shown in Figure 2.4. The parameters can be listed as follows: r_{in} is the inner raceway contour radius, r_{out} is the radius of the outer raceway sphere, ϕ_0 is the free contact angle, c_d is the clearance between the rollers and the race, d_r is the roller diameter, r_r is the radius of the roller contour, d_e is the diameter of the roller race, and B_B is the bearing width. R_{in} and R_{out} are the inner and outer radii of the bearing, respectively.

According to Figure 2.5, the radii of curvature for the roller-inner race contact can be written as

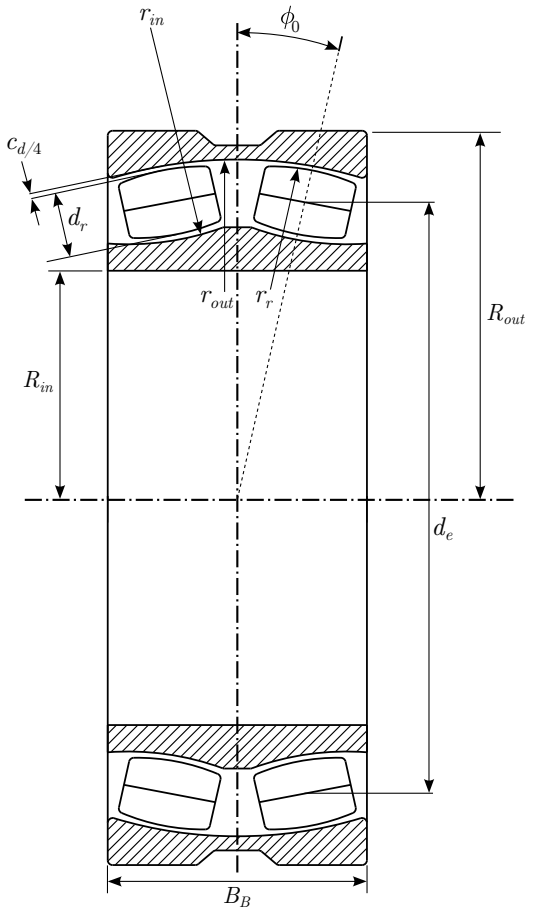

Kuva 2.4. Some of the main dimensions of a spherical roller bearing

$$r_{Ax}^{in} = \frac{d_r}{2}, \tag{2.48}$$

$$r_{Ay}^{in} = r_r, \tag{2.49}$$

$$r_{Bx}^{in} = \frac{d_e - d_r \cos\phi_0 - \frac{c_d}{2}\cos\phi_0}{2\cos\phi_0}, \tag{2.50}$$

$$r_{By}^{in} = -r_{in}. \tag{2.51}$$

Similarly, the equations for the radii of curvature for the roller-outer race contact can be written as

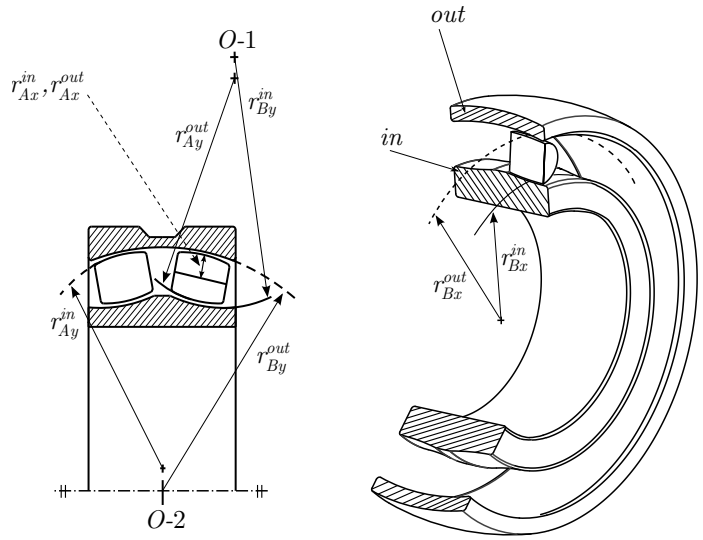

Kuva 2.5. Radii of curvatures between roller, outer race, and inner race

$$r_{Ax}^{out} = \frac{d_r}{2}, \tag{2.52}$$

$$r_{Ay}^{out} = r_r, \tag{2.53}$$

$$r_{Bx}^{out} = -\frac{d_e + d_r \cos\phi_0 + \frac{c_d}{2}\cos\phi_0}{2\cos\phi_0}, \tag{2.54}$$

$$r_{By}^{out} = -r_{out}. \tag{2.55}$$

2.5.3 Contact Deformation in a Spherical Roller Bearing

From the relative displacements between the inner and outer race the resultant elastic deformation of the i^{th} rolling element of the j^{th} row located at angle β_j^i from the x-axis can be determined. The initial distance, A_0, between the inner and outer raceway curvature centers (O-1, O-2) can be written according to Figure 2.5 as follows

$$A_0 = \left|r_{By}^{out}\right| + \left|r_{By}^{in}\right| - d_r - \frac{c_d}{2}. \tag{2.56}$$

The corresponding loaded distance for roller i in row j can be written as follows

$$A_L\left(\beta_j^i\right) = \sqrt{\left(\delta_{zj}^i\right)^2 + \left(\delta_{rj}^i\right)^2}, \tag{2.57}$$

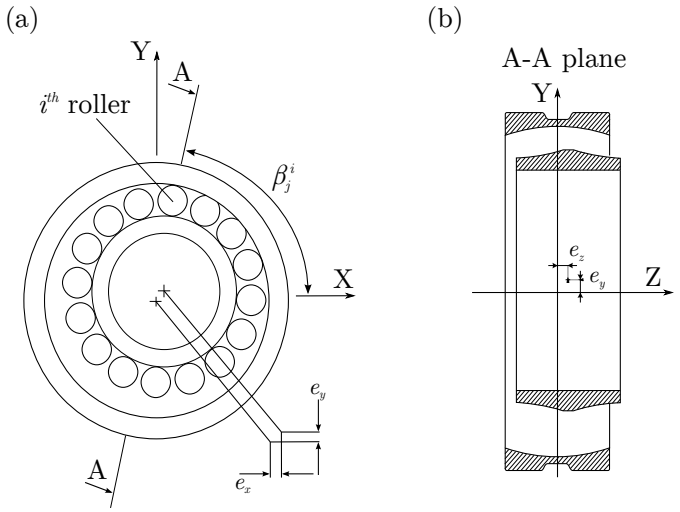

Kuva 2.6. (a) axial and (b) transverse cross-section in the A-A plane of spherical roller bearing

where δ_{zj}^i and δ_{rj}^i are the displacements for roller i in row j in axial and radial directions, respectively. The displacements can be defined as

$$\delta_{zj}^i = A_0 \sin\phi_0 + e_z, \tag{2.58}$$

$$\delta_{rj}^i = A_0 \cos\phi_0 + e_x \cos\beta_j^i + e_y \sin\beta_j^i, \tag{2.59}$$

where e_x, e_y and e_z are displacements in xyz-coordinate system and β_j^i is the attitude angle of roller i in row j as shown in Figure 2.6. It should be noted that the initial contact angle, ϕ_0, is negative for the 1^{st} row and positive for the 2^{nd} row of the bearing.

The distance between race surfaces along the common normal is

$$d_s\left(\beta_j^i\right) = \left|r_{By}^{out}\right| + \left|r_{By}^{in}\right| - A_L\left(\beta_j^i\right). \tag{2.60}$$

The elastic compression becomes

$$\delta_{\beta_j^i} = d_r - d_s\left(\beta_j^i\right). \tag{2.61}$$

The loaded contact angle in each roller element can be defined as

$$\phi_j^i = \tan^{-1}\left(\frac{\delta_{zj}^i}{\delta_{rj}^i}\right). \tag{2.62}$$

2.5.4 Elastic Deformation in a Spherical Roller Bearing

In a single rolling element, the total deflection is the sum of the contact deflections between the roller and the inner and outer races. The deflection between the roller and the race can be approximated as [23]

$$\delta_0 = \left(\frac{F_{cn}}{k_c}\right)^{2/3}, \tag{2.63}$$

where F_{cn} is the normal load and k_c can be calculated by using the elliptic integrals and ellipticity parameter as follows

$$k_c = \pi k_e E' \sqrt{\frac{R\xi}{4.5\zeta^3}}, \tag{2.64}$$

where E' is the effective modulus of elasticity which is defined as

$$\frac{1}{E'} = \frac{1}{2}\left(\frac{1-\nu_A^2}{E_A} + \frac{1-\nu_B^2}{E_B}\right), \tag{2.65}$$

where E and ν are the modulus of elasticity and Poisson's ratio of solids A and B, correspondingly. The total stiffness coefficient for both inner and outer race contact can be expressed as

$$k_c^{tot} = \frac{1}{\left[(k_c^{in})^{-2/3} + (k_c^{out})^{-2/3}\right]^{3/2}}. \tag{2.66}$$

According to Equations (2.61) and (2.66), the contact force for roller i in row j, can be obtained as follows

$$F_{cj}^i = k_c^{tot}\left(\delta_{\beta_j^i}\right)^{3/2}. \tag{2.67}$$

Finally, total bearing forces acting upon the shaft in the x, y, and z directions can be summarized as follows

$$F_x^b = -\sum_{j=1}^{2}\sum_{i=1}^{N} F_{cj}^i \cos\phi_j^i \cos\beta_j^i, \tag{2.68}$$

$$F_y^b = -\sum_{j=1}^{2}\sum_{i=1}^{N} F_{cj}^i \cos\phi_j^i \sin\beta_j^i, \text{ and} \tag{2.69}$$

$$F_z^b = -\sum_{j=1}^{2}\sum_{i=1}^{N} F_{cj}^i \sin\phi_j^i, \tag{2.70}$$

where the variable N is the number of rolling elements in each row.

2.6 Rotor Analysis Types

Traditional research into rotor dynamics is concerned mainly with the stability and natural frequencies of the rotor system. The natural frequencies are changing due to the rotational speed dependent gyroscopic effect, which has to be considered in analyses. The changing vibrations characteristics may affect the critical speeds of the machine. Analyses can be performed in both the frequency and the time domain. The analyses in the frequency domain are computationally more efficient but they cannot provide the results that simulate the actual usage of the machine. Transient analyses in the time domain provide comparable results for evaluating the real-world vibrations in transient conditions, but these kinds of analyses are computationally expensive.

Campbell diagram

A rotor dynamics analysis result that is commonly seen is the Campbell diagram, which relates the rotational speed and the natural frequencies of the system. The frequencies change due to the gyroscopic effect. The support structure of the machine is also taken into consideration, and for example, the changing bearing stiffnesses are considered. The damped natural frequencies cannot be solved using the Equation (2.4) because the variables in that equation are only the mass and the stiffness, and the gyroscopic effect is omitted. Instead, the eigenvalues of the system can be solved from the equation of motion in the state space form

$$\mathbf{A} = \begin{bmatrix} \mathbf{0} & \mathbf{I} \\ -\mathbf{M}^{-1}\mathbf{K} & -\mathbf{M}^{-1}(\mathbf{C}+\mathbf{C_g}) \end{bmatrix}. \tag{2.71}$$

The results of the eigenvalues solved are shown in the chart that has a rotational speed in the x–axis and frequency in the y–axis. The damping ratios of each mode

can also be derived from the results of the eigenvalue analysis. The instability regions of the system occur in the rotational speed where the damping is negative. Negative damping means that the system is self-excited and the vibration amplitude increases as a function of time. This can be obtained from the eigenvalue results as positive real parts of complex eigenvalues.

Steady State Responses

The steady state responses are the responses of the system due to steady excitations. If the response curve is observed in the time domain, the steady state response is that part of the response curve where the transient oscillation vanishes. The steady state solution can be solved from the following relationship

$$\boldsymbol{q}(t) = \boldsymbol{a}\sin\omega_f t + \boldsymbol{b}\cos\omega_f t, \tag{2.72}$$

where the vectors $\boldsymbol{a}$ and $\boldsymbol{b}$ are coefficient vectors, ω_f is the frequency of the excitation. The first and second time derivatives of equation (2.72) are

$$\dot{\boldsymbol{q}}(t) = \omega_f \boldsymbol{a}\cos\omega_f t - \omega_f \boldsymbol{b}\sin\omega_f t, \text{ and} \tag{2.73}$$

$$\ddot{\boldsymbol{q}}(t) = -\omega_f^2 \boldsymbol{a}\sin\omega_f t - \omega_f^2 \boldsymbol{b}\cos\omega_f t. \tag{2.74}$$

Substituting Equations (2.72)–(2.74) into the equation of motion (2.1) and converting the equation in state space form the following can be obtained

$$\begin{bmatrix} \mathbf{K}-\omega_f^2\mathbf{M} & -\omega_f\mathbf{C} \\ \omega_f\mathbf{C} & \mathbf{K}-\omega_f^2\mathbf{M} \end{bmatrix} \begin{bmatrix} \boldsymbol{a} \\ \boldsymbol{b} \end{bmatrix} = \begin{bmatrix} \boldsymbol{F_s} \\ \boldsymbol{F_c} \end{bmatrix}. \tag{2.75}$$

Force vectors $\boldsymbol{F_s}$ and $\boldsymbol{F_c}$ are the components of force vector $\boldsymbol{F}$ that may contain some phase angle. The coefficient vectors $\boldsymbol{a}$ and $\boldsymbol{b}$ are solved as follows

$$\begin{bmatrix} \boldsymbol{a} \\ \boldsymbol{b} \end{bmatrix} = \begin{bmatrix} \mathbf{K}-\omega_f^2\mathbf{M} & -\omega_f\mathbf{C} \\ \omega_f\mathbf{C} & \mathbf{K}-\omega_f^2\mathbf{M} \end{bmatrix}^{-1} \begin{bmatrix} \boldsymbol{F_s} \\ \boldsymbol{F_c} \end{bmatrix}. \tag{2.76}$$

As an example, in case of rotational degrees of freedom the force vector $\boldsymbol{F}$ contains only torsional excitation components in a steady state analysis, which can be expressed as follows

$$\boldsymbol{F} = \boldsymbol{T}_s \sin(\omega_f t), \tag{2.77}$$

where the vector $\boldsymbol{T}_s$ contains the excitation torque amplitudes.

The steady state vibration response can now be solved from Equation (2.72) as follows

$$\boldsymbol{q}(t) = \boldsymbol{a} \sin \omega_f t + \boldsymbol{b} \cos \omega_f t = \boldsymbol{X} \cos \left(\omega_f t - \boldsymbol{\phi} \right), \tag{2.78}$$

where the i^{th} elements of the vectors $\boldsymbol{X}$ and $\boldsymbol{\phi}$ are

$$X_i = \sqrt{a_i^2 + b_i^2}, \text{ and} \tag{2.79}$$

$$\tan \phi_i = \frac{a_i}{b_i}. \tag{2.80}$$

The response amplitudes X_i are the torsional vibration amplitudes and are evaluated at each excitation frequency using the corresponding torque excitation amplitude. The total response is obtained by summing up the responses caused by individual excitations, *i.e.* harmonics. The phase angle ϕ_i describes the phase shift between the excitation torque and the system response.

Whirling Mode Shapes

The orbits of the deformed rotor show the deformation shape and the relative amplitude of each point (node in FEM), with respect to each other. The orbit plots can be observed from the eigenvectors of the eigenvalue analysis. The relative displacement of each point can be defined from the real and imaginary parts of the eigenvector with respect to the phase angle of the rotor. Orbit plots respect the mode shapes of the systems and it can be sketched at each calculated rotational speed. Naturally, the shape of the orbits are dependent on the rotational speeds due to the vibration characteristics.

Transient analysis

In the transient analysis, the equation of motion is solved in the time domain. The equation of motion can be converted into an ordinary differential equation that can be numerically integrated. Typically, numerically accurate integrators such as higher orders of Runge-Kutta methods are used. The results of the analysis are the displacement and velocity vectors at each pre-defined time step. The results in the time domain can be converted into the frequency domain for a better understanding of the vibration characteristics. The conversion can be done using the Fast Fourier Transform (FFT). The transient analysis defines the dynamic response and it can be used to simulate known critical incidents such as exceeding the resonance, or component failure in the drive train.

Luku 3

Non-Ideal Rotating Systems

A set of apparatus come under the category of rotating machines. Rotating machines include drives such as motors and generators, gears, cranks, and all types of driven shafts and rolls. The interest for the dynamics of rotating systems arises from the vibrations of the rotating machinery. The rotating shafts have cyclic loadings that may excite the rotating system to vibrate if the resonance frequency is equal to the rotational speed frequency or multiples of the rotational frequency. Perfectly ideal systems do not suffer from these vibrations, even in the resonance. However, practical rotating systems always contain imperfections and the operational rotational speed has to be away from the resonance frequency.

This doctoral dissertation concentrates on a limited number of machines. These machines can be divided in two subcategories: permanent magnet electric machines, and tubular thin-walled rolls. The PM electric machines studied are a large-scale wind generator, and a special PM trans-rotary magnetic gear. The tubular roll studied is a paper machine tube roll which is supported by two different methods: spherical roller bearings, and disc supports. This chapter introduces the typical characteristics of the permanent magnet electric machines and imperfections that may cause vibration problems in the rotating systems.

3.1 Permanent Magnet Electric Machinery

Rotating electric machinery is old technology and the fundamental principles of the electromagnetics in electric machines have not undergone major changes since the early 20^{th} century. However, the advanced materials, technological advances and industrial needs have changed the family of the electric machines into machines with higher efficiency, better power density, and better performance. One enormous

breakthrough was the development of permanent magnet materials that have provided the opportunity to utilize permanent magnet technology for industrial needs.

Permanent magnet machines can be used in a wide range of rotating applications. The typical characteristics of the PM machines are high torque and power densities, a high torque capability at low speeds, a wide operational speed range, high efficiencies over the speed range, high reliability, and acceptable cost [83, 46, 66]. With these technical advantages PM machines are strong contenders, for example, in renewable energy production, transportation drives, industrial drives, and robots. For example, a large part of the industrial-sized wind generators use permanent magnet technology because of its technological advantages.

A conventional electric machine is an interior rotor machine where a rotor is rotating inside of a stator. In a permanent magnet application, the rotor is magnetized by permanent magnets which produce magnetic flux. When a current carrying conductor is moving in the magnetic field, it produces a force component according Lorentz's force equation

$$\boldsymbol{F}_{EM} = q\left(\boldsymbol{E} + \boldsymbol{v}_c \times \boldsymbol{B}\right), \tag{3.1}$$

where $\boldsymbol{F}_{EM}$ is the electromagnetic force vector, q is the electric charge, $\boldsymbol{E}$ is the electric field, $\boldsymbol{v}_c$ is the velocity vector of the conductor, and $\boldsymbol{B}$ is the magnetic field. In the case of rotating electric machines, it is reasonable to observe the electromagnetic forces in a 2D environment, including radial and tangential force components. The tangential force vector of a magnet leads to a total torque of the machine that can be described by the equation

$$T_q = F_{tan} r p, \tag{3.2}$$

where T_q is the total torque, F_{tan} is the tangential force component of a single pole, r is the radius from the centerline of the rotor to the center of the magnet and p is the number of poles.

The power of the machine P_w is a product of torque and angular velocity of the rotor as follows

$$P_w = T_q \Omega. \tag{3.3}$$

There are both electromagnetic and mechanical forces that have to be taken into consideration. A severe mechanical force type is the mechanical centrifugal force. The centrifugal force of a magnet in a PM machine can be expressed as follows

$$F_{rad} = \frac{m_{mg} v^2}{r}, \tag{3.4}$$

where F_{rad} is the radial centrifugal force, m_{mg} is the mass of the magnet, and v is the tangential speed of the magnet. The centrifugal force of the mechanical unbalance can be derived using the same equation.

The electromagnetic force component in the radial direction can be estimated by several proposed ways. One way is to multiply the tangential force component of an individual magnet by a factor of 10. However, it is most likely too conservative estimation, and the estimated force is much larger than the existing force [48]. Another way is to utilize the Maxwell's equation [55]

$$F_{rad} = \frac{B^2 A}{2\mu_0} \left(1 - \frac{1}{\mu_r}\right) \tag{3.5}$$

where B is the magnetic flux density in the air gap, A is the area in which the flux is affecting which is related to the phase angle of the rotor, μ_0 is vacuum permeability, and μ_r is the relative permeability. The magnetic flux density can be evaluated, roughly, to be 1 Tesla but in order to obtain more accurate force components, an electric finite element analysis must be conducted. The methods introduced for evaluating the electromagnetic radial components give results that are in scale with each other, even though the evaluation is rather imprecise.

Electromagnetic forces vary due to the phase angle and rotational speed of the rotor. There are some harmonic force components that occur during the usage and can be high. These electromagnetic excitations are interesting from a dynamics viewpoint in the sense that the rotational speed corresponding to the resonance frequency of the rotor have to be avoided. The electrical frequency is differs from the mechanical frequency, since the mechanical frequency is $1/60$ of rotational speed in revolutions per minute. The electrical frequency is a product of rotational speed and a pole pair number for the machine. If the number of pole pairs is, for example, 12 and the rotational speed is 600 rpm the electrical and mechanical frequencies are 120 Hz and 10 Hz, respectively. The frequencies of harmonic electromagnetic excitations are multiples of the electromagnetic excitation frequency.

3.2 Imperfections in the Rotating Machinery

The design of rotating machinery is a delicate process where different aspects from different fields of engineering have to be taken into consideration. In addition for engineering requirement, economic issues come into the scope. From an engineering perspective, the performance of the machine is an important aspect. Additionally,

the machine has to be able to withstand all the expected as well as surprising forces and loads that occur during the operational life cycle. The materials, manufacturing and assembling methods have to be chosen so as to fulfill all the engineering and economic requirements; the final result should be a balance between these two aspects.

In the design process of electric machines, an intensive cooperation between electrical and mechanical engineers must occur. From the mechanical design perspective, the important features of the machines are the forces that occur during usage. The machine has to be able to withstand all such forces during the life cycle of the machine. These forces include electromagnetic forces in all directions, mechanical forces such as centrifugal forces as well as thermal loads. The type of the machine defines what the critical forces for the system are. For example, in low-speed machines the electromagnetic radial forces are remarkably higher than the mechanical centrifugal forces. On the other hand, in high-speed machines the mechanical radial force plays a prominent role but the radial pulling force has to be taken seriously into consideration as well.

Because of the low rotational speed (10-20 rpm) and high torque operation, the diameter of a megawatt-range Direct-Driven (DD) Permanent Magnet Synchronous Generator (PMSG) can easily be several meters. The weight of the generator and the wind turbine structure itself are high. The weight of the machine can be reduced by making the rotor structure sparse and as hollow as possible. A sparse structure is liable to external excitations because of decreased structural stiffness. For this reason, the electromagnetic harmonic excitations have to be studied in the design process, and further, if the excitations seem to be crucial or the structure loose, the dynamics of the structure should be studied using transient analysis as presented in [30]. Eccentricity of the machine leads to a highly unbalanced total radial force as introduced in [10].

High-speed machines have large radial force components that are the main focus in the design process from mechanical point of view. A large part of the radial forces arise from the mechanical centrifugal forces. As can be seen from the Equation (3.4), the magnitude of the centrifugal force is affected by the square of the tangential velocity. Additionally, there are radial electromagnetic forces in the system which may be uneven along the airgap circle of the electric machine, and cause a residual radial force component. The combined residual radial force from the mechanical unbalance and radially uneven electromagnetic forces may cause excitations in the rotating system.

The technical specifications of the different machine types can be gathered together in a list that introduces the main differences and details of the machine types that can be examined in designing process. The items are listed as follows:

- the frequency and the magnitude of loading cycles,
- the force components and the torque of the machines,
- bearings and cooling, and
- unbalance and vibration.

These aspects can be studied separately from design and manufacturing perspectives. High rotation speed increases the number of cycles, and this might be severe from a fatigue viewpoint. This aspect must be considered when choosing the manufacturing method. The unbalance of the machine has to be minimized. An eccentrically rotating rotor has unequal force components that may excite resonance during operation. The DD machine type can have a rotor that has a diameter of several meters, although the air gap between the rotor and the stator can be as little as 5 mm. This must be taken into account in tolerances and manufacturing methods. Even if the manufacturing errors are within the tolerances distribution following Gaussian distribution, the design has to be done by assuming the worst case scenario.

3.2.1 Electromagnetic Excitations in Rotating Machinery

Cogging torque and torque ripple are torsional electromagnetic excitations. The cogging torque is the variation in the tangential force when a permanent magnet passes a pole. The frequency of the excitation is rotational speed dependent and proportional to the number of magnetic poles in the machine. The magnitude of the cogging force is a result of the magnetic pulling force and it is independent on the electrical loading of the machine. Torque ripple on the other hand, depends on the electrical loading of the machine. The electrical loading generates harmonic electromagnetic force components from the stator current. The excitation frequency is dependent on the pole number and the rotational speed when the magnitude of the excitation depends on the current power in the stator side of the machine. Both of these excitations occur at multiples of the electrical frequency, *i.e* electrical harmonics.

In ideal rotating machines, the air gap between the rotor and the stator is perfectly round and equal in length along the circle and the length of the machine, and the radial force components are evenly balanced around the air gap. However, most electromechanical systems have some imperfections arising from manufacturing and assembling imperfections. For example, the cylindrical components are not perfectly round, and the rotor and stator are not perfectly concentric, so the radial force components do not balance perfectly. If the axis of rotation of the rotor is not collinear with the centerline of the stator, there is a resultant transverse force

between the rotor and stator. Furthermore, if the axis of rotation of the rotor is not collinear to the rotor centerline, or the rotor is not perfectly round; a harmonic excitation develops as the rotor rotates. These phenomena are referred to as static and dynamic eccentricity, respectively.

Higher order roundness imperfections have a similar kind of effect as the eccentricity. The unbalanced forces excite the system to rotate if the higher force component rotate along the rotational speed of the rotor. For example, the second order roundness error, namely ellipticity, causes excitation twice in a revolution meaning that the excitation frequency is double the rotational speed frequency. These excitations may cause problems in the operational speed range if the machine dynamics is designed in terms of the rotational speed frequency. In addition, the higher order roundness imperfections exist but the amplitudes of the errors become increasingly lower.

3.2.2 Rotating Component Imperfections

The rotating components may contain several types of imperfections that may cause problems in terms of vibrations. In conventional bearing, the rotating elements, balls or rolls, rotate between rings. The rings of the bearings may have defects such as grooves or cracks. More importantly, even if the defect cannot be recognized the bearing rings may contain some roundness errors. These errors are similar to the above introduced roundness errors in electric machines. However, in this case the varying load from the bearing is directly propagated to the rotating shaft. Naturally, excitations in the shaft leads to the vibration problems in the resonance.

The roundness error profile of a circle can be expressed in the form of a Fourier cosine series as follows

$$R\left(\alpha\right) = \sum_{k=1}^{n} c_k \cos\left(k\gamma + \phi_k\right) , \tag{3.6}$$

where c_k is the amplitude, ϕ_k is the phase angle of the roundness error of k^{th} order, k is the harmonic order of roundness error, and γ is the attitude angle of the rolling element. The amplitudes and phase angles of the harmonic components can be obtained from measurements by analyzing the results with the FFT.

The effect of the waviness of the bearing ring can be included in the elastic deformation of roller i in row j, (2.61) as follows

$$\delta_{w_j^i} = \delta_{\beta_j^i} + \sum_{k=1}^{n} c_k^{in} \cos\left[k\left(\beta_j^i - \theta_{in}\right) + \phi_k\right] , \tag{3.7}$$

where c_k^{in} is the amplitude of the roundness error in bearing inner ring of k^{th} order, θ_{in} is the phase angle of bearing inner ring.

Luku 4

Rotating Machinery: Case Studies

This chapter presents the essential findings of the doctoral thesis research. The results are divided into subsections according to the cases studied. The first case is the directly driven wind generator construction where the torsional vibrations of the structure in terms of placing of the magnets on the rotor were studied in detail [30]. The second studied case is the vibration analysis of a trans-rotary magnetic gear rotor [29]. The third set of results combines the studies that concentrated on the tube roll with different support structures [69, 28]. The results demonstrate the effects of different manufacturing and assembling imperfections, and the electromagnetic forces in the rotating machinery in terms of vibration.

4.1 Large Permanent Magnet Wind Generator: Torsional Vibration Analysis

A torsional vibration analysis can be applied to evaluate the effect of the cogging torque and torque ripple of a permanent magnet synchronous generator on the mechanical vibration of the whole wind turbine installation. The objective was to evaluate the severity of the cogging torque and the torque ripple in direct-driven wind turbines. The mechanical drive train model of the wind turbine installation consisted of a turbine hub and flexible blades, a torque transmission shaft and PMSG. Two different permanent magnet generator rotor constructions of a 4.5 MW direct-driven PMSG were analyzed. Both of the studied PMSG designs were based on an existing PMSG, the details of which are presented in [56]. The cogging torque and the torque ripple at the rated torque operation were calculated with the help of a detailed electromagnetic finite element analysis for the both permanent magnet generator rotor constructions. Their effects on the steady state and transient state mechanical responses were analyzed.

The mechanical drive train of the generator was distinguished in discrete inertia components that were connected with torsional springs. Figure 4.1 presents the schematic figure of the simplified model. In principle, the model is the same as that presented in Figure 2.1.

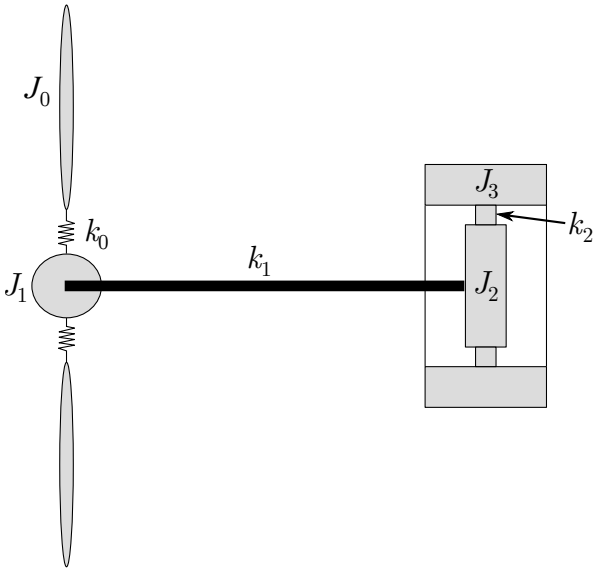

Kuva 4.1. Simplified four degrees of freedom system representing a large-scale wind turbine

The analyzed system consisted of a wind turbine rotor, a torque transmission shaft and a PMSG. The main design parameters of the permanent magnet synchronous generator are given in Table 4.1. As shown in this table, the nominal rotational speed of the generator in rpm was the same as the rated electrical frequency, *i.e.*, 1 rpm corresponds to 1 Hz. This was due to the number of the pole pairs that was 60. The analyzed rotor structures are illustrated in Figure 4.2 and their descriptions are as follows: a) a generator rotor with rectangular rotor surface magnets placed in two rows that were shifted by half a stator slot pitch from each other, b) a generator rotor with rectangular magnets buried inside a rotor lamination stack shaped to produce a sinusoidal air gap flux density and placed in two rows that were shifted by a half stator slot pitch from each other. The generator parameters are identical to those given in Table 4.1 in both of the cases studied.

The turbine structure was modeled using four torsional degrees of freedom connected by torsional springs. The parameters of the mechanical model are presented in Table 4.2. Parameters k_2, J_2, and J_3 were evaluated by using a detailed structural finite element model of the rotor. Other parameters k_1, k_2, J_1 and J_2 were estimations based on literature [58, 45] or given by the turbine supplier.

Taulukko 4.1. Main parameters of the 4.5 MW direct-driven PMSG

Parameter	Value
Number of pole pairs	60
Number of phases	3
Number of stator slots	360
Number of slots per pole and phase	1
Nominal rotational speed	15.2 rpm
Rated frequency	15.2 Hz
Rated output power	4.5 MW
Rated output torque	2.9 MNm

Taulukko 4.2. Model parameters of the 4-DOF model

Parameter	Symbol	Value
Turbine blades stiffness	k_1	$3.5 \cdot 10^8$ Nm/rad
Turbine shaft stiffness	k_2	$3.8 \cdot 10^8$ Nm/rad
Rotor spring stiffness	k_3	$5.5 \cdot 10^9$ Nm/rad
Turbine blade's moment of inertia	J_1	$9.9 \cdot 10^6$ kgm^2
Turbine hub's moment of inertia	J_2	$1.1 \cdot 10^6$ kgm^2
Rotor's inner part moment of inertia	J_3	5770 kgm^2
Rotor's outer part moment of inertia	J_4	97030 kgm^2
Modal damping coefficient of mode 1	ξ_1	2 %
Modal damping coefficient of mode 2	ξ_2	2 %
Modal damping coefficient of mode 3	ξ_3	2 %
Turbine radius	r_t	45 m

The cogging torque and torque ripple values were calculated for both generator constructions by applying a three-dimensional time-stepping finite element analysis. The torque ripple calculations were performed at the load angle corresponding to the rated torque operation. The FLUX-3D software package by Cedrat Ltd was applied in the calculations. The three-dimensional approach was selected because it automatically takes the effects of the edge fields into account, which, in fact, leads to a more accurate main flux calculation. The drawback in adopting the three-dimensional approach is that it is computationally extremely expensive. The time step size in the analyzes was selected in such a way that at each time step the rotor rotates 0.05 mechanical degrees to cover the effect of high order torque harmonics.

The calculated cogging torque and torque ripple amplitudes at different excitation frequencies are shown in Table 4.3. Only amplitudes larger than 0.1 % of the rated

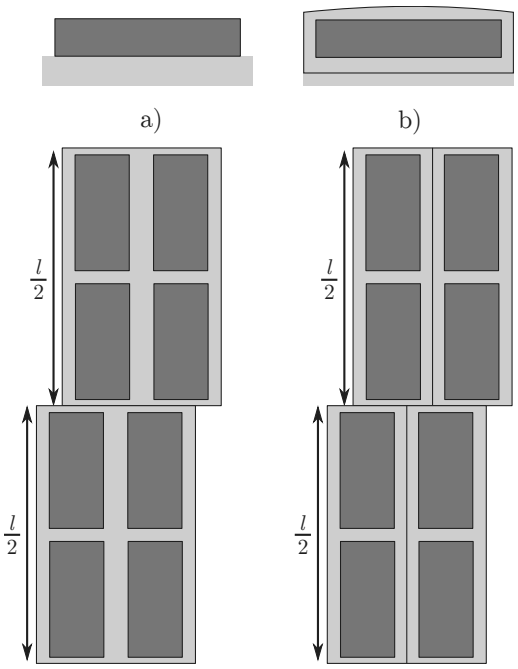

Kuva 4.2. The magnet configurations that were studied. Parameter l is the axial length of the generator rotor.

torque are shown and were considered in the analyses. The cogging torque is independent of the generator load. On the other hand, the ripple depends on the generator loading, which means that the generator has to generate some electricity in order to have any torque ripple. The cogging torque components are introduced as per unit values of the nominal rated torque. The torque ripple is proportional to the load torque of the generator that varies depending on the operational conditions.

The frequency of the excitation component doubled when the magnets were placed in two rows that were shifted from each other. The effect of the shape of the air gap magnetic flux density on the cogging torque can be seen by comparing the cogging torques of cases A and B in Table 4.3. In case A, where rectangular rotor surface magnets were used, the magnetic flux density of the permanent magnets was rectangular resulting in a high cogging torque. In case B, the rotor magnets were buried inside a shaped lamination stack producing a more sinusoidal air gap flux density distribution resulting in a cogging torque that was reduced to one tenth in comparison to case A.

During operation, the torque of the generator was assumed to vary as a function of the rotation speed according to Figure 4.3. The power production starts at the

Taulukko 4.3. Torsional excitations of the studied magnet configurations. In the analysis, values under 0.1 % of the rated torque were not considered.

		Case A	**Case B**
		Cogging Torque	
Harmonic	f(Hz)	Torque %	Torque %
12	182.4	1.76	0.17
		Torque Ripple	
Harmonic	f(Hz)	Torque %	Torque %
2	30.4	< 0.1	0.11
4	60.8	0.18	< 0.1
6	91.2	1.79	0.83
8	121.6	0.24	< 0.1
10	152.0	0.34	< 0.1
12	182.4	1.17	0.32
14	212.8	0.18	< 0.1
16	243.2	0.11	< 0.1
18	273.6	< 0.1	0.11

cut-in speed of 4 rpm. The maximum torque at the cut-in speed is $0.125T_n$. The torque is assumed to increase linearly until the nominal rotational speed 15.2 rpm is achieved and the torque is half of the rated torque T_n. In reality, the torque is proportional to the square of the wind speed but the linear assumption simplifies the model. The obtained results will be on safe side, since the linear model gives larger torque values than the parabolic model. The speed is kept constant and the rated torque $T_n = 2.9$ MNm is obtained at the rated speed of 15.2 rpm. When the rated speed is reached, the torque of the generator is regulated by controlling the load angle of the generator. Above the rated speed, the power is kept constant by reducing the torque until a cut-out speed of 22 rpm is achieved.

The undamped natural frequencies of the system were solved using Equation (2.4). The frequencies of the three modes are 2.86 Hz, 9.86 Hz and 165 Hz, respectively. The first mode at frequency of zero is the torsional rigid body mode since the system was unconstrained. The natural frequencies and excitation frequencies which are multiples of the rotational speed frequency f_s are illustrated in Figure 4.4. It can be seen that all excitation frequencies cross the two lowest natural frequencies (2.86 Hz and 9.86 Hz) at speeds below 5 rpm. These resonances must be passed during the start-up from the zero to the operational rotational speed. Several excitation frequencies coincide with the third natural frequency in the operational speed range, resulting in a number of possible resonances. The severity of these resonances must be determined in the steady state analysis.

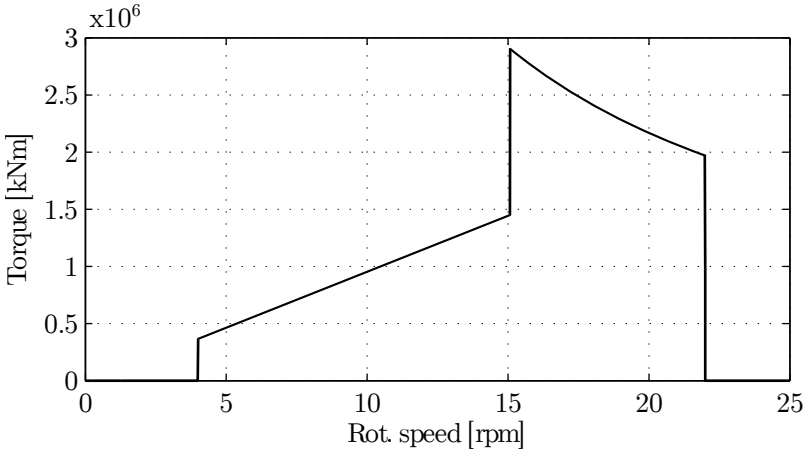

Kuva 4.3. Output torque of the generator as a function of rotor rotating speed. The product of output torque and the rotational speed defines the output power of the generator. The rotational speed can be adjusted also by the pitch angle of the turbine blades.

The main phenomenon that the simplified model was required to capture was the resonances caused by the cogging torque and the torque ripple. According to the parameters shown in Table 4.2, the inertia of the whole turbine (J_1 and J_2 combined) was more than 100 times greater than the inertia of the generator (J_3 and J_4 combined). Since 90 % of the turbine inertia was in the blades, the flexible turbine blades were affecting most in the smallest frequencies. If the whole main turbine was modeled as one inertia, the natural frequencies of the system would be 9.3 Hz and 165 Hz, respectively [72].

4.1.1 Steady State Analysis

The steady state responses were solved at each rotation speed and for each harmonic excitation torque component according to the theory discussed in Chapter 2. The total response of the system was obtained by summing up the individual harmonic responses. The results are given as the dynamic torques of the turbine blades (inertia J_1) and the outer part of the rotor (inertia J_4). The rotational speed of the turbine was varied with an increment of 0.01 rpm. The dynamic torque can be solved from the following equations [7].

$$\boldsymbol{T}_d(t) = \mathbf{K}\boldsymbol{\theta}(t) + \mathbf{C}\dot{\boldsymbol{\theta}}(t) \tag{4.1}$$

Now the vectors of $\boldsymbol{\theta}$ can be substituted using Equation 2.78 and the following torque vectors can be defined

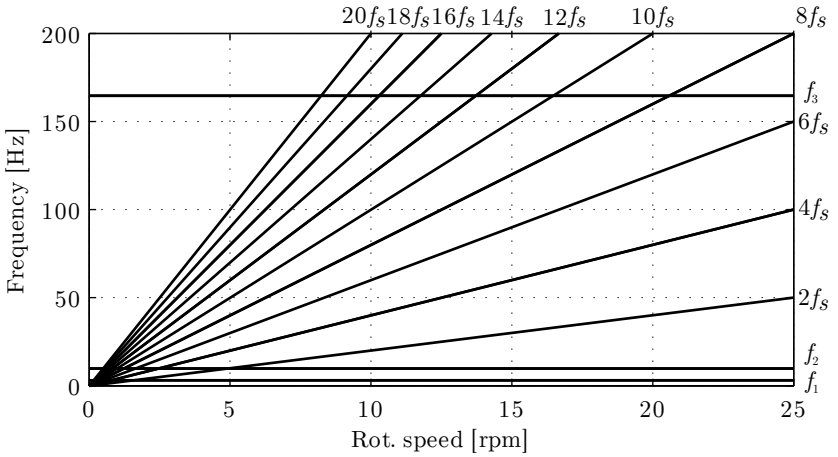

Kuva 4.4. Frequency interference diagram of the system. The resonances occur at the rotational speeds where rotational speed dependent harmonic excitation components exceed natural frequencies.

$$\begin{aligned} \boldsymbol{T}_{ds} &= \mathbf{K}\boldsymbol{a} - \omega_f \mathbf{C}\boldsymbol{b} \\ \boldsymbol{T}_{dc} &= \mathbf{K}\boldsymbol{b} + \omega_f \mathbf{C}\boldsymbol{a} \end{aligned} \tag{4.2}$$

The dynamic torque in nodal point i can be defined as follows

$$T_d^i = \sqrt{(T_{vs}^i)^2 + (T_{vc}^i)^2} \tag{4.3}$$

In the case of the generator rotor construction with rectangular surface mounted magnets, the dynamic torques at the nodal points can be seen in Figure 4.5. The largest amplitudes occur at the rotation speed range of 0 to 3 rpm. The strongest resonance in the turbine rotor occurs at a rotation speed of 0.24 rpm and in the outer part of the generator rotor at a speed of 0.82 rpm. Both of these are caused by the combined cogging torque and torque ripple at the frequency of $12f_s$. As can be seen from Figure 4.5, the peaks of the torque in the resonance are extremely sharp. It is inconvenient to evaluate the absolute value of the highest torque because the length of the used time steps makes a difference to the highest values. Despite this, a reasonable approximation for the magnitude of the vibration can be made. Resonances may cause vibrations and noise during start-up, but probably will not break the drive train components if start-up is rapid and the resonance region is passed within a short period of time. One resonance occurs within the operating speed range at 13.72 rpm. This is caused by the cogging torque and the torque ripple at the frequency of $12f_s$ passing the third resonance frequency which can be observed from the frequency interference diagram (Figure 4.4). For these reasons,

the generator rotor construction with rectangular rotor surface magnets is not an optimal design. However, it may be acceptable under certain conditions.

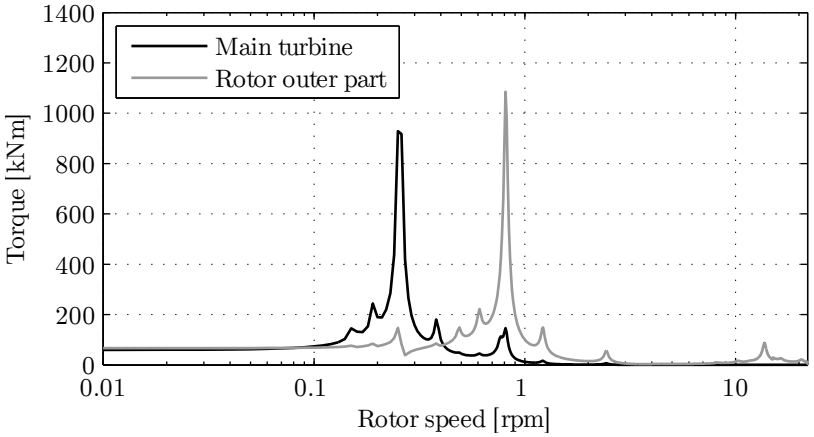

Kuva 4.5. Dynamic torques of the turbine blades and the outer part of the rotor derived from the steady state solution over the rotational speed range in the case of the generator construction with rectangular, surface mounted permanent magnets. Dynamic torque responses at the low rotational speeds dominate the overall behavior.

Figure 4.6 shows the dynamic torques at the nodal points in the case of the generator rotor construction with rectangular magnets buried inside a rotor lamination stack shaped in a way that the no-load air gap flux density is sinusoidal. The largest amplitudes occur at the rotation speeds of 0.24 rpm for the turbine rotor and at 0.82 rpm for the outer part of the generator rotor, similar to the case of rectangular shape surface mounted PMs. Resonances are caused by the cogging torque at the frequency of $12f_s$. Two smaller vibration amplitudes are also found in the operating speed range at 4.93 rpm and this is caused by $2f_s$ torque ripple and at 13.72 rpm caused by the cogging torque and the torque ripple at the frequency $12f_s$. When the amplitudes of the dynamic nodal torque in the two mentioned cases are compared, it can be concluded that the generator rotor construction with rectangular magnets buried inside a shaped lamination stack causes vibrations, the amplitudes of which are about ten-fold smaller than the amplitudes of the generator rotor construction with surface magnets in two rows. Furthermore, it can be concluded that the construction with buried magnets does not cause vibration problems because of the low torque amplitudes.

4.1.2 Transient Analysis

A start-up of the wind turbine from standstill to operating speed was also investigated. The driving torque was the torque from the wind that is calculated using

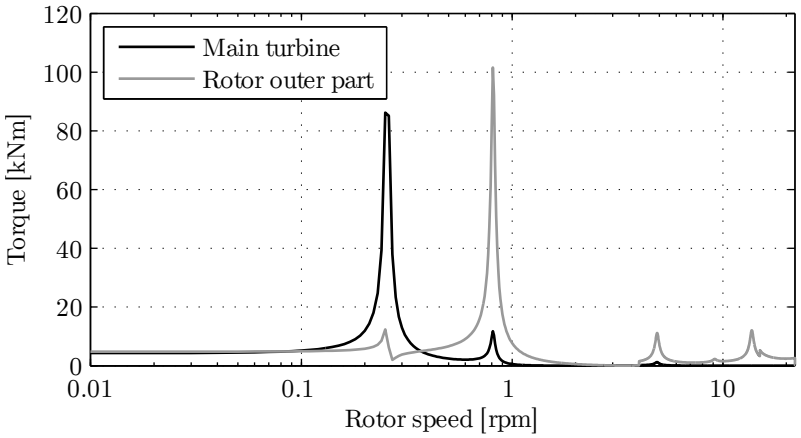

Kuva 4.6. Dynamic torques of the turbine blades and the outer part of the rotor derived from the steady state solution over the rotational speed range in the case of the generator construction with rectangular, surface mounted permanent magnets. Dynamic torque responses at the low rotational speeds dominate the overall behavior.

the equation [81]

$$T_w = \frac{0.5\rho\pi r_t^3 v_w^2 C_p(\theta_w, \lambda_w)}{\lambda_w} \tag{4.4}$$

where ρ is the mass density of air, r_t is the turbine radius, v_w is the wind speed, and C_p is the power coefficient, which depends on the blade pitch angle θ_w and the tip speed ratio λ_w defined as follows

$$\lambda_w = \frac{\Omega r_t}{v_w} \tag{4.5}$$

where Ω is the angular velocity of the turbine hub. The power coefficient C_p can be expressed as follows

$$C_p(\theta_w, \lambda_w) = 0.22\left(\frac{116}{\beta} - 0.4\theta_w - 5\right)e^{-\frac{12.5}{\beta}} \tag{4.6}$$

where the coefficient β

$$\beta = \left(\frac{1}{\lambda_w + 0.08\theta_w} - \frac{0.035}{\theta_w^3 + 1}\right)^{-1} \tag{4.7}$$

In all simulations, the mass density of the air was assumed to be 1.225 kg/m^3. Furthermore, the blade pitch angle θ_w was assumed to decrease linearly from 26° to 0° in 30 seconds from the start. One critical situation is when the wind speed is low, resulting in a low accelerating torque. Therefore, all simulations were performed at the cut-in wind speed of the turbine 3.5 m/s. In analyses, the wind speed was increased linearly from zero to 3.5 m/s within two seconds from the start point and then kept constant. The numerical integrator used in this study was the MATLAB integrator *ode45* that is based on the fourth-order Runge-Kutta [21] method with a time step of $1.0{\cdot}10^{-3}$ seconds.

Figure 4.7 shows the rotational speed of the turbine during the simulated start-up in the case of the generator rotor construction with rectangular magnets buried inside a rotor lamination stack shaped so that the no-load air gap flux density is sinusoidal. A constant rotation speed of 4 rpm is achieved after an acceleration period of 30 seconds. A rotational speed 4 rpm is the cut-in speed of the generator, which means that at slower rotation speeds, the rotor is rotating but power is not being produced and the dynamic load torque in the generator is equal to zero. Some resonance can be detected when the rotation speed is close to 0.82 rpm, which equals the rotation speed of the resonance peak in the steady state analysis shown in Figure 4.6.

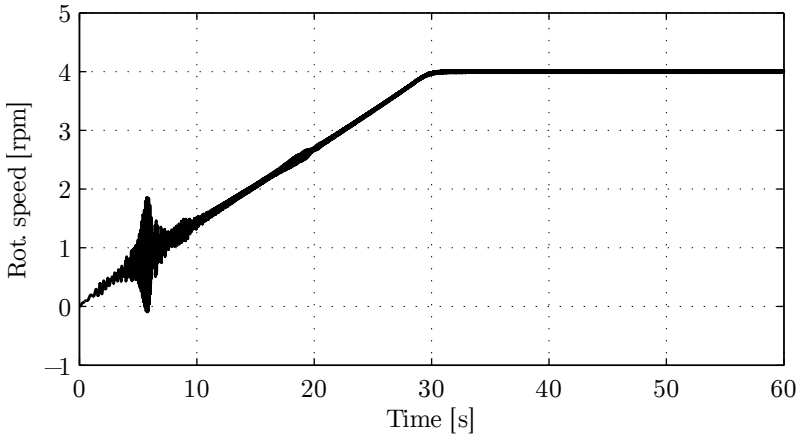

Kuva 4.7. Rotation speed of the rotor of the generator during start-up in the case of the generator construction with rectangular surface magnets placed in two rows. Passing some resonances causes disturbance in the acceleration from stand still to the operational speed.

The dynamic torque of the turbine rotor blades and the outer part of the generator rotor during start-up in the case of the generator rotor construction with rectangular surface magnets installed in two rows are shown in Figure 4.8. A resonance can be seen in both observed components. The maximum resonance amplitude of the

turbine blades is 250 kNm. The maximum resonance amplitude of the generator rotor is 600 kNm. Figure 4.9 shows the corresponding results in the case of the generator rotor construction with rectangular magnets buried inside the rotor lamination stack producing a sinusoidal air gap flux density. Resonance can be seen when the rotor passes the rotation speeds of 0.24 rpm and 0.82 rpm the resonance amplitudes being 40 kNm and 55 kNm for the blades and the rotor outer part, respectively.

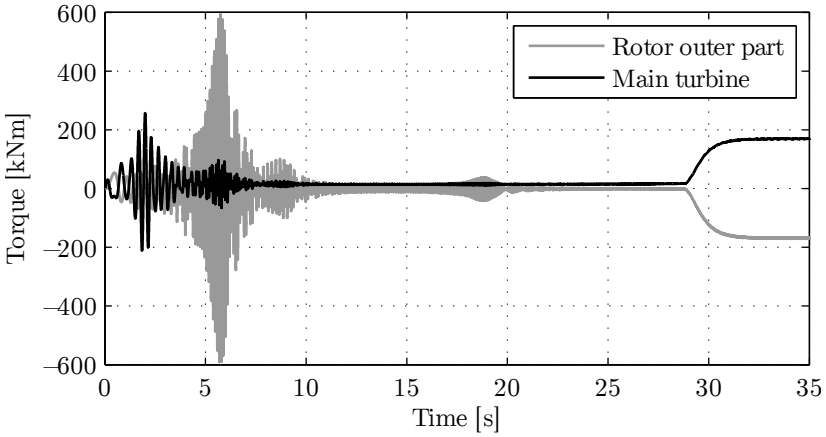

Kuva 4.8. Dynamic torque of the turbine blades and the generator rotor outer part during start-up at the wind speed of 3.5 m/s. Generator construction with rectangular surface magnets. Within the first 25 seconds, the generator does not produce any torque since the rotational speed of the generator is below the cut-in speed. Once the cut-in speed is achieved, the generator starts to produce torque and after 35 seconds the dynamic torques in both shown components are constant. Passing the resonances causes significant dynamic torque into the system.

In the case of rectangular surface magnets, the resonances are significant. However, the worst resonances are passed in less than 10 seconds, and therefore, any mechanical damage to the drive train is improbable. A more detailed analysis, such as a fatigue life calculation, should be performed before this magnet construction can be accepted. If the magnets are buried inside the lamination stack, the torsional vibration amplitudes decrease remarkably.

The results show the second studied permanent magnet generator constructions, namely the generator rotor with rectangular magnets buried inside a rotor lamination stack producing a sinusoidal air gap flux density, placed in two rows that were shifted by half a stator slot pitch from each other, is suitable for the studied system. The generator rotor construction with a rectangular rotor surface magnet construction placed in two rows that were shifted by half stator slot pitch from each other is barely acceptable. However, a more detailed analysis of this

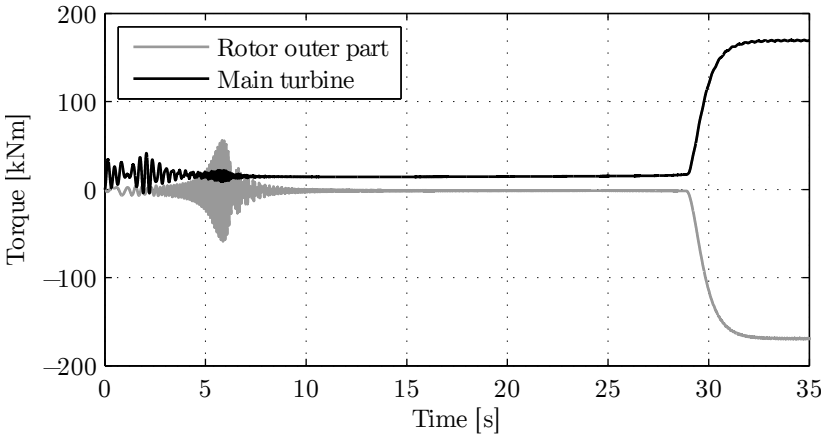

Kuva 4.9. Dynamic torque of the turbine blades and the generator rotor outer part during start-up at the wind speed of 3.5 m/s. Generator construction with rectangular magnets buried inside a rotor lamination stack producing sinusoidal air gap flux density at no load. Within the first 25 seconds, the generator does not produce any torque since the rotational speed of the generator is below the cut-in speed. Once the cut-in speed is achieved, the generator starts to produce torque and after 35 seconds the dynamic torques in both shown components are constant. Passing the resonances causes only minor dynamic torque into the system.

construction should be performed. It was noticed that the resonance caused by the excitation torque should occur at the lowest possible speed. In the case of the system studied, this means that the cogging torque at $12f_s$ is not as harmful as the one occurring at $6f_s$. This observation favors permanent magnet skewing, or using at least two sets of magnets, as is the case in this study.

4.2 Trans-Rotary Magnetic Gear: Vibration Analysis

A Trans-Rotary Magnetic Gear (TROMAG) has been introduced recently as a reliable and efficient way to convert low-speed, high-force, and small-displacement translation into high-speed low-torque rotation, or vice versa. An attractive potential area of application is wave energy harvesting. In principle, a TROMAG consists of a rotor and translator, both formed by attaching multiple helical arrays of permanent magnets to a cylindrical ferromagnetic base structure to establish helical magnetic poles having a pole pitch of τ_p as presented in Figure 4.10.

A sketch of the idealized TROMAG being studied is presented in Figure 4.11. The operating principles and design aspects of the device have been described in [54, 52, 53]. Table 4.4 presents a few of the most relevant parameters and the principal system dimensions. Depending on how the inner and outer ferromagnetic

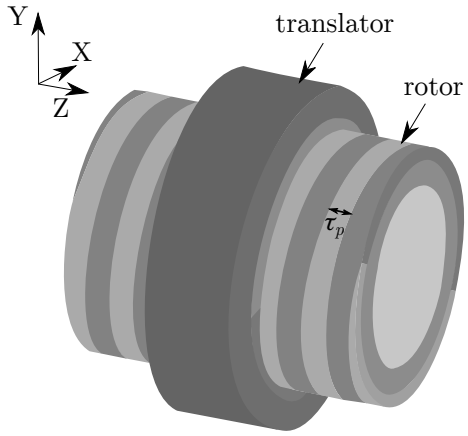

Kuva 4.10. The main principle of the TROMAG

components are mechanically fixed or left free to move, the translator of the idealized TROMAG can be on the inside or the outside. An inner rotor and outer translator were assumed here.

The inner rotor was supported by roller bearings on each end and flexibly coupled to the generator drive train. The bearings must be capable of withstanding high frequency pulsating loads and changes in rotational direction. Moreover, the bearings must be capable of supporting the large radial forces that result from small deviations in rotor-to-translator concentricity. The outer translator moves axially along the rotor surface supported by linear bearings. An effective length of 4 meters was chosen for the translator to provide a 2 meter stroke resulting in an effective rotor length that was also 2 meters.

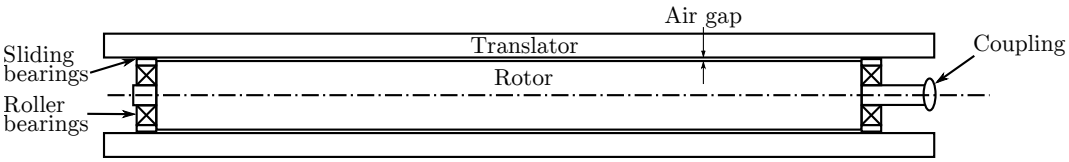

Kuva 4.11. The studied TROMAG configuration

Rotor-to-translator magnet interaction produces spatial forces between the rotor and translator magnets. The force components working radially to pull the rotor and translator surfaces together will be referred to here as radial forces, F_{rad}, the force components working circumferentially will be referred to as tangential forces, F_{tan}, and the components acting axially will be referred to as axial forces, F_{ax}. In the idealized TROMAG, the highest radial force components occur when rotor

Taulukko 4.4. Properties of the studied TROMAG

Quantity	Value
Translator length	4000 mm
Outer diameter of the rotor including PMs	200 mm
Rotor length	2000 mm
Translator yoke thickness	20 mm
Rotor yoke thickness	20 mm
Magnet material	NdFeB
Magnet coercivity	834 kAm
Magnet remanent flux density	1.1 T
Magnet thickness on translator and rotor	5 mm
Pole pitch	10 mm
Air gap length	2 mm
Number of poles	2

and translator magnets of equal width are aligned. When they are not aligned, magnetic forces act between adjacent rotor and translator magnets to bring them into alignment. These are referred to as shear forces, F_{sh}, shown in Figure 4.12. Tangential and axial forces can be considered as the components of the shear force F_{sh}. The tangential and axial forces can be described using the trigonometric relation presented in Equation (4.8):

$$\begin{aligned} F_{tan} &= F_{sh} \cos \varepsilon \\ F_{ax} &= F_{sh} \sin \varepsilon \end{aligned} \tag{4.8}$$

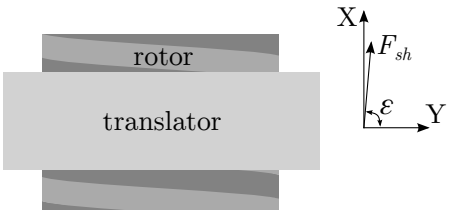

Kuva 4.12. Direction of the shear force

TROMAG torque production is a result of the tangential forces arising from the axial displacement of the translator through the permanent magnet interaction. The ratio of the axial force to torque is defined as the gear ratio G and is obtained as follows

$$G = \frac{F_{ax}}{T_q} = \frac{2\pi}{p \cdot \tau_p}\,, \tag{4.9}$$

where p is the number of poles and τ_p is the pole pitch. Since the torque equals the product of tangential force, F_{tan} and rotor outer radius, r_{rot}, the angle ε can be obtained from the following relation.

$$\varepsilon = \tan^{-1}\left(\frac{2\pi r_{rot}}{p\tau_p}\right). \tag{4.10}$$

The analytical approach taken here to examine axial and tangential electromagnetic force components was described in detail by Wang et al. [79]. In this method, the shear force is considered in a simplified 2D environment and Laplace and Poisson equations are analytically solved to obtain the flux density distribution. The flux density values are then used to calculate the shear force components based on Lorentz force law. Although the model is 2D, the results are very close to those obtained from 3D finite element analysis. On the other hand, for further accuracy, computationally expensive 3D finite element analysis is used for accurate calculation of the radial force component arising from the eccentricity.

In the idealized TROMAG studied, the translator was a long and slender hollow cylinder, which is prone to bending under unbalanced radial loads. Holm et al. investigated static bending deformation of the rotor by modeling a rotor as a simply supported beam with uniformly distributed load [32]. Loading cases assumed an uneven air gap with a resultant magnetic pulling force towards the area of the smallest gap. The rotor diameter, which affects the overall magnitude of the magnetic force and the flexibility of the rotor, was also varied. The conclusion was that increasing the diameter of the rotor makes it stiffer and more able to withstand bending forces.

Vibrations of an idealized TROMAG were studied using the finite element method. The tangential forces of PM interaction were interpolated in polynomial form for the dynamic analysis. PM interaction can be considered as the stiffness between the rotor and the translator. The equilibrium point, where no torque or axial shear force is produced, is where the permanent magnets of the rotor and the translator are aligned. Translator displacement results in a displacement difference between the rotor and translator that produces the tangential force components, *i.e.*, torque.

The analytically defined total tangential force of the system is presented in Figure 4.13 as a function of axial displacement. In the analytic calculation, the rotor was kept stationary while the translator was displaced axially. The number of poles is two, which has a major effect on the tangential force component, which can be determined from Equation (4.8).

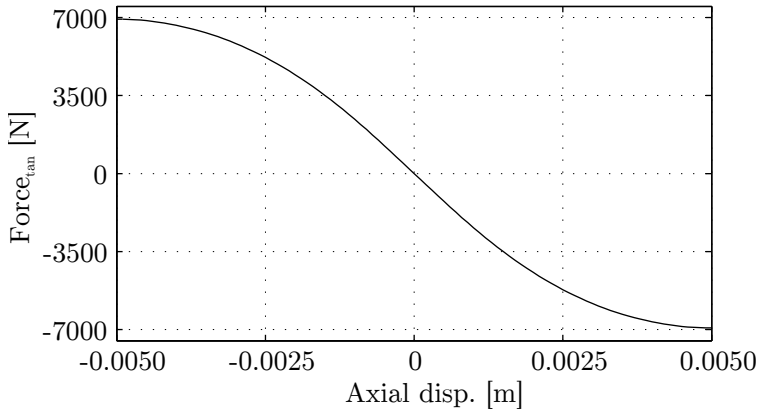

Kuva 4.13. Analytically defined total tangential force of the PM interaction as a function of axial displacement. Close to the equilibrium point the force-axial displacement-ratio is close to linear.

The maximum tangential force of the TROMAG with 2 poles is about 7000 N for a 200 mm rotor diameter, which is equivalent to 700 Nm torque. Increasing the number of poles would result in lower gear ratios, lower rotational speeds, and higher tangential forces.

The radial force was calculated for the system using 3D finite element analysis. The analyzed device was the one with 10 % eccentric rotor. The residual total force in the direction of shortest air gap as a function of the axial displacement is presented in Figure 4.14.

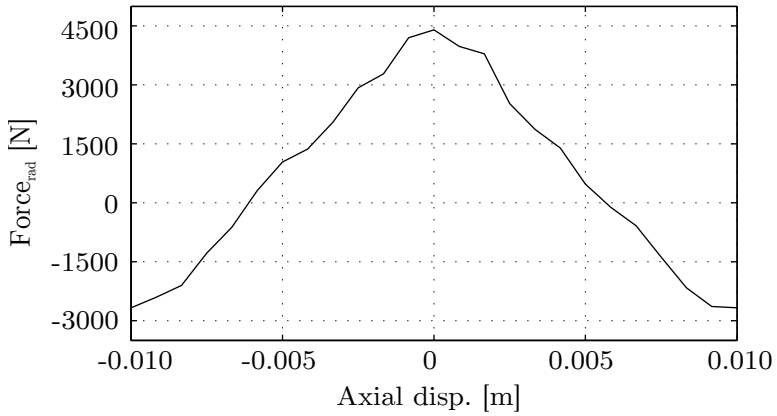

Kuva 4.14. Residual radial force of the PM interaction as a function of axial displacement using FEA

4.2.1 Steady State Vibration

The operational speed range in the analyses was between 0–6000 rpm. The natural frequencies of the system were solved within the operational frequency range. The resulting Campbell diagram is shown in Figure 4.15. The system is close to symmetrical, and the deviation between forward and backward whirling modes is almost negligible. The operating speed exceeds natural frequencies at around 5400 rpm.

In addition to the Campbell diagram, steady state response due to the unbalanced mass of the rotor was studied. Figure 4.16 presents the unbalance response within the operational frequency range. A high response peak is revealed where the operating speed exceeds the natural frequency of the system. Forward and backward whirling modes are coupled in the response curve, and a clear deviation cannot be seen although it is evident that the forward whirling mode would dominate the steady state response due to an unbalanced mass force.

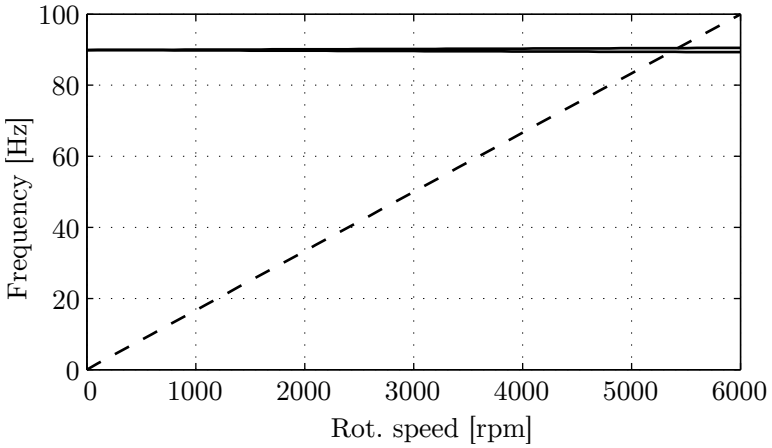

Kuva 4.15. Campbell diagram of the TROMAG. Within the studied rotational speed range, the first set of whirling modes are exceeded at the rotational speed around 5400 rpm.

4.2.2 Transient Translational Vibration

The extended study of translational vibrations of the TROMAG is presented in [29]. The transient analysis was performed using a modal reduction method. A total of 7 modes were used covering the frequency range between 0-1000 Hz without rigid body modes. Three bending mode pairs and one torsional mode were included. Table 4.5 shows the selected modes. In the transient analysis, the external forces were varied to simulate each of the studied eccentricity cases. A

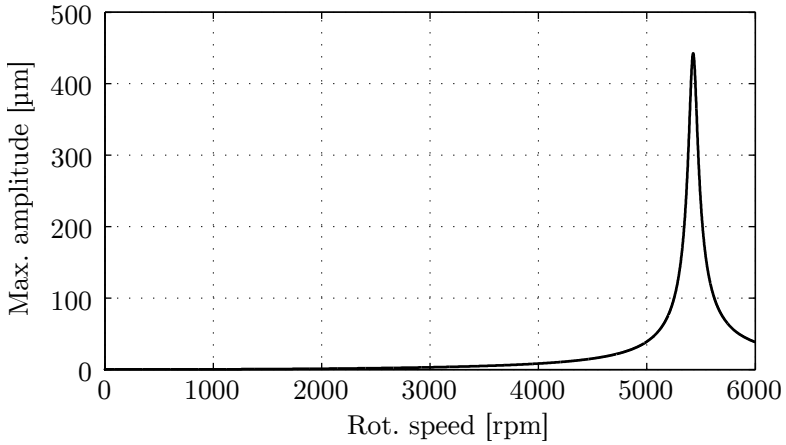

Kuva 4.16. Steady state unbalance response in the middle of the TROMAG rotor

transient analysis without eccentricity was carried out and the results were used as a benchmark.

The dynamically and statically eccentric rotors were studied. The maximum unbalance mass defined by the ISO 1940 standard was used for mechanical excitation. The used unbalance grade was G2.5. The mass unbalance was equally distributed to the nodes of finite element model of the rotor. Transient analyzes began at the equilibrium position with zero angular velocity and zero acceleration. Sinusoidal driving torque was applied to the end node. Rotational speed oscillated between zero and 6000 rpm.

Taulukko 4.5. Modes that are used in modal reduction; (b) indicates bending modes and (t) torsional mode.

Mode #	**Frequency [Hz]**
1/2	206/206 (b)
3/4	530/530 (b)
5	670 (t)
6/7	959/959 (b)

Figure 4.17 shows the rotational speed as a function of time. The transient response of a half working cycle in the middle of the rotor is shown in Figure 4.18, where only force acting upon the system was the mass unbalance. The rotor was concentric with the translator, and there were no unbalanced radial magnetic forces. Resonance was reached by the rotor twice in each half working cycle; once during acceleration and once during deceleration. System acceleration was high,

and the greatest excitation occurred when rotational speed was near the natural frequency of the rotor. The calculated excitation amplitude, 0.18 mm, is not large enough to cause the rotor to impact the translator, which for the concentric rotor case would occur with amplitudes in excess of 2 mm.

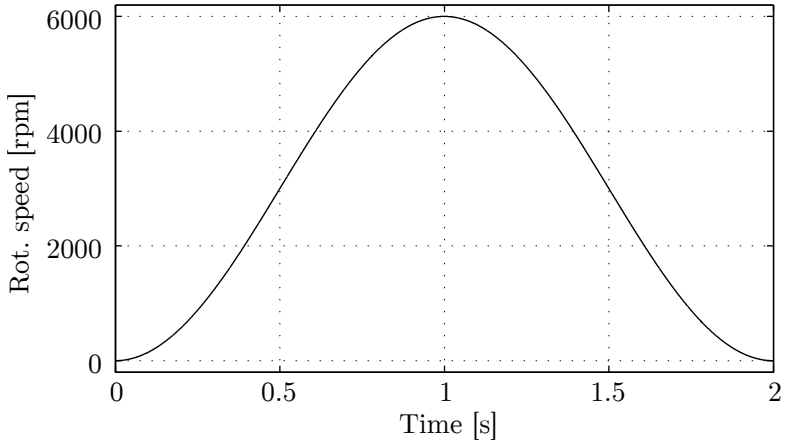

Kuva 4.17. The rotational speed of the TROMAG rotor in the simulation

In practice, rotor or translator eccentricity is likely. An eccentric translator produces a stationary force component pulling towards the area of the smallest gap. The load is similar to the gravity body load, which results in a bending deformation, but is not rotational speed dependent. The load itself does not cause harmonic excitation. On the other hand, a dynamically eccentric rotor, that is a rotor with an offset between its axis and the system centerline, results in a force component that rotates with the rotor. The rotating force component results in harmonic excitation with a frequency equal to the frequency of the rotational speed, which results in more unwanted vibration than that seen with the eccentric translator.

Figure 4.19 shows the predicted response of the rotor with 10 % static eccentricity in the rotor that equals distance of 0.2 mm. The static unbalanced electromagnetic force causes some bending for the rotor at the zero rotational speed. Once the rotor hits the resonance the amplitude of the vibration response is 0.25 mm that is not critical for the system even though the static eccentricity will close the air gap another 0.2 mm.

Figure 4.20 shows the predicted response of the rotor with 10 % dynamic eccentricity. The dynamically eccentric rotor leads to high excitation forces that excite the system to vibrate even at lower rotational speeds below the resonance frequency. The magnitude of this magnetic excitation is independent of the rotational speed. Reaching resonance, the harmonic magnetic excitations produce deformations that are a decade larger than in the case of static eccentricity being 2 mm and large

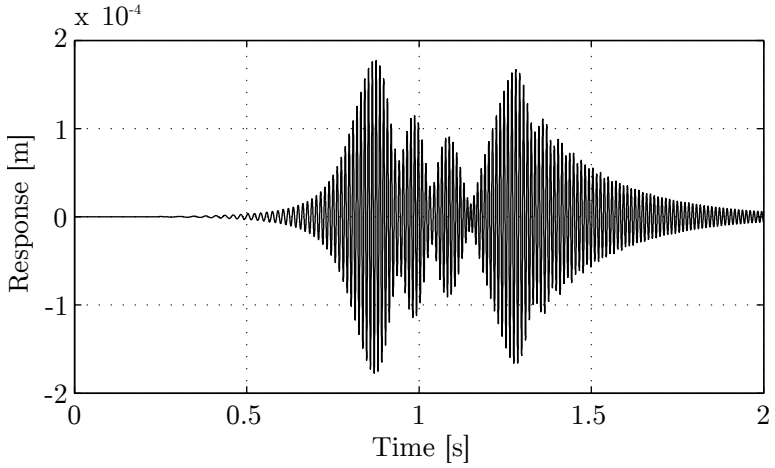

Kuva 4.18. Vertical response of the transient analysis in the middle of the unbalanced TROMAG rotor with centric rotor. Rotational speed exceeds the natural frequency twice in the analyzed time span that can be seen as vibrations in the response curve.

enough for the rotor to begin to impact the translator; a situation that would be destructive to the device.

4.2.3 Transient Torsional Vibration

In simulated operation of the idealized TROMAG, when the translator was forced into linear motion, interaction between the permanent magnets of the translator and rotor caused the rotor to rotate. The rotor responded to the linear motion of the translator according to the helical arrangement of the permanent magnets. The number of poles affects both the rotational speed and the torque. Figure 4.21 shows the rotational speed for TROMAG configurations with two, four, and eight poles. In the torsional vibration study, the half working cycle was increased to four seconds. There was no external torque, *i.e.* generator, in the system in order to demonstrate the characteristic features of a permanent magnet interaction in such applications.

The results indicate that the increasing pole number results in a lower rotational speed and a higher frequency and lower amplitude of the oscillation. This is the result of the higher torque capability of the higher pole number configurations. If PM interaction is considered analogous to a spring between the translator and the rotor, the magnitude of the torque-to-displacement ratio corresponds to the stiffness of the spring. Lower stiffness combined with the higher rotational speed resulted in larger oscillation amplitudes. When the torque increased and the rotational speed decreased for configurations with a higher number of poles, oscil-

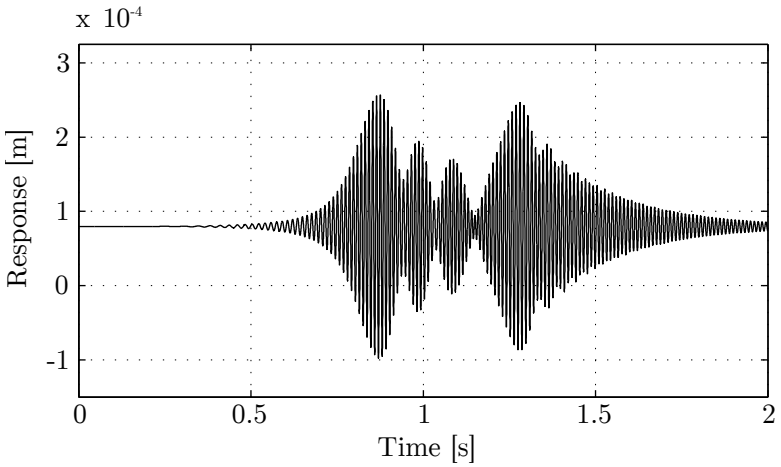

Kuva 4.19. Response of the transient analysis in the middle of the rotor in the vertical direction with 10 % statically eccentric unbalanced rotor. Rotational speed exceeds the natural frequency twice in the analyzed time span that can be seen as vibrations in the response curve.

lation amplitude decreased. Both increasing oscillation frequency and decreasing oscillation amplitude corresponded to increasing torque-to-displacement ratio.

The air gap was also a variable for the system analyses. A smaller air gap resulted in higher forces and vice versa. The studied air gap lengths were 1 mm, 2 mm, and 3 mm. The effect of force variation due to air gap variation was studied in terms of the resulting vibration characteristics.

The difference between expected and simulated angular displacements were calculated that revealed the oscillation of the system more clearly than in Figure 4.21. The oscillation curves were translated into the frequency domain using discrete Fourier transformation and Hanning window averaging. Figure 4.22 shows the resulting amplitude spectra where the vibrations can be seen as clear peaks. The results in the frequency domain clearly show the nominal vibration frequency for each case. Nominal vibration frequency increased as the air gap decreased, indicating a more intensive pulling force due to the shorter air gap. The analogy between the magnet interaction and mechanical spring is applicable in the sense of the PM force indicating the stiffness of the spring. Additionally, higher torque values corresponded to smaller torsional vibrations as seen from the amplitudes of the rigid torsional vibrations.

The effect of the external load was also studied in terms of characteristic frequencies. The response curves for configurations with and without external loading, two poles, and 2 mm air gap in the frequency domain are presented in Figure 4.23.

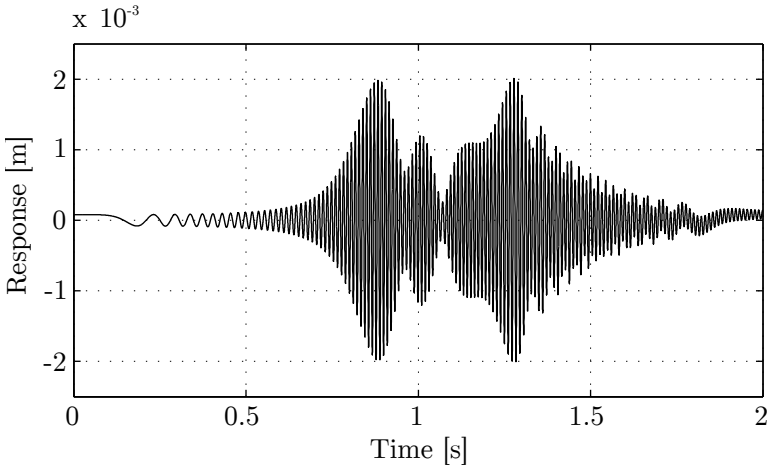

Kuva 4.20. Response of the transient analysis in the middle of the rotor in the vertical direction with 10 % dynamically eccentric unbalanced rotor. Rotational speed exceeds the natural frequency twice in the analyzed time span that can be seen as vibrations in the response curve.

Including external loading and presenting the results in the frequency domain results in a response curve, which does not show a clear peak representing an oscillation at a certain frequency. This is because of the non-linear tangential force as a function of displacement that was presented in Figure 4.13. For zero external load, the displacement difference between the angular displacement of the rotor and the linear displacement of the translator is small. A small displacement difference means the force-displacement ratio stays within the linear range close to the zero displacement difference. The reason for sinusoidal variation in the amplitude spectrum of the loaded case is the short period of simulated time having only a half working cycle, resulting in incomplete periods of oscillation frequencies that would be required to perform a better Fourier transformation. However, it can be seen that the oscillation in the loaded case sweeps a certain range of frequencies below the frequency of the response peak in the unloaded case.

4.3 Paper Machinery Tube Roll: Twice-Running-Speed Vibration

A paper machine tube roll was studied using two different kinds of support systems. The first supporting system included spherical roller bearings on both ends, which were placed in bearing housing standings on pedestals. Another supporting structure was pedestals with freely rotating discs. The shaft of the tube roll rotated freely on the discs and could be lifted off. The discs were connected

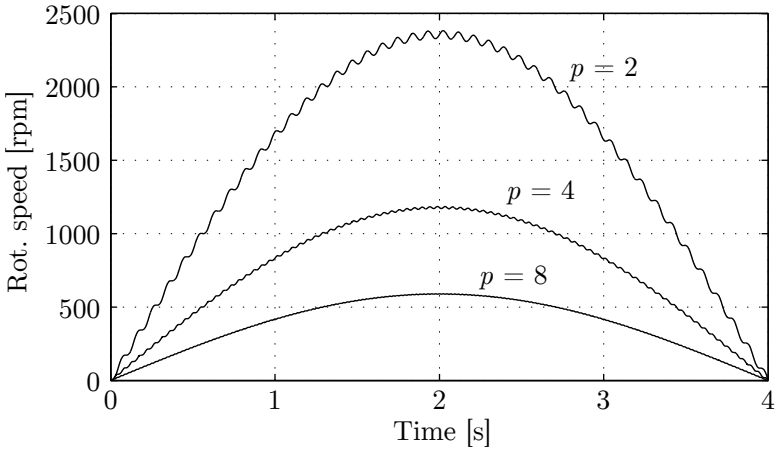

Kuva 4.21. The rotational speeds of the rotor with different pole numbers p. The higher number of poles decreases the rotational speed but serves higher torque capability.

into the pedestal with needle roller bearings.

The components of both supporting methods had some imperfections that caused vibrations in the systems. Both the bearings and the discs had roundness errors in the contacting surfaces that caused vibration problems during usage. These roundness error were measured and emulated in the simulation models as accurately as possible. The roundness imperfection cause excitations, the frequencies of which are multiples of the rotational speed frequency. These excitation may excite the rotor vibrations in the subcritical rotational speed range. In these studies, the twice-running speed frequencies were studied in detail. The order of roundness error indicates the number of excitations in a revolution, *e.g.*, the first order roundness error is the eccentricity, the second order error ellipticity, the third order error triangularity and so on. Figure 4.24 demonstrates the roundness error profiles of three lowest orders. The simulation results were validated by comparing them with the measured results from the tube roll test rig.

A schematic figure of the studied paper machine tube roll is shown in Figure 4.25. The measurement equipment consisted of a PC-based data collection system, laser sensors fitted with amplifiers, a connection panel and a guide trail in which the sensors were installed. The measurement results for the middle of the roll in the vertical and horizontal directions were considered. The locations of the measurement points are shown in Figure 4.25. The angular velocity of the rotor is obtained using a pulse sensor.

The thickness definition of the shell of the tube roll was based on measurements carried out on the real structure. The thickness of the shell of the roll varied between 17.86–19.59 mm, while the average thickness was 18.72 mm. The thickness of the

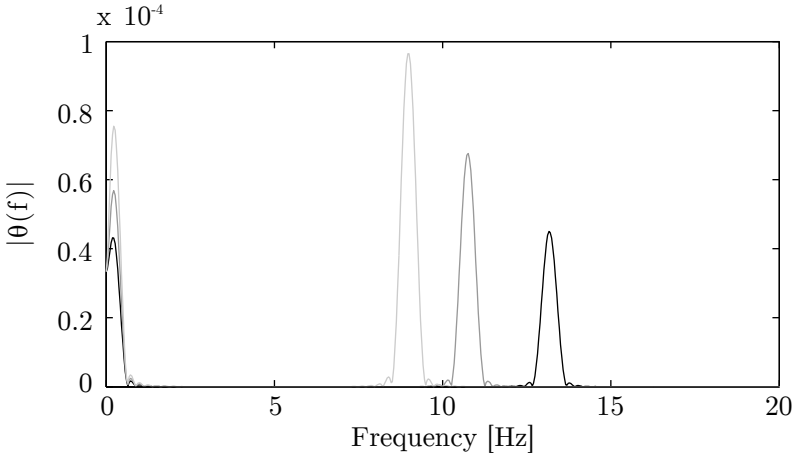

Kuva 4.22. Amplitude spectrums of simulated torque curves. The black line indicates 1 mm, the semi-grey line 2 mm, and the light-grey 3 mm air gap. Longer air gap results in smaller force that can be observed from the higher amplitude peak in lower frequency in the amplitude spectrum.

shell was measured along the whole length of the shell. The thickness varied along the length and the rotation angle of the tube roll. The variation of the thickness of the shell causes imperfect mass and stiffness distribution. The imperfect mass distribution causes unbalance excitations, while the imperfect stiffness distribution causes a twice-running-speed (2X) resonance in which the variation in bending stiffness, together with gravity, excites the symmetrical modes.

4.3.1 Simulation Models

In the first case studied, the roller test rig was modeled using the finite element method in MATLAB. The simulation model included a flexible symmetrical tube roll, the supports of the spherical roller bearings, and nonlinear contact forces between the roll and the bearings. The asymmetry of the roll was not taken into account in order to simplify the model and decrease the computational effort. On the other hand, it was assumed that the excitations from the bearings were the main reason for the twice-running-speed resonance. The model parameters, such as thickness of the tube, were the measured averages from the test rig.

In the finite element model, Timoshenko beam elements having six degrees of freedom in a node were used. Axial displacements and rotation around x-axis was constrained in all rotor nodes and only the radial translations of the bearing housings were free. The finite element model comprised 21 nodes on the rotor having 4 DOFs per node and additional mass elements to describe the support

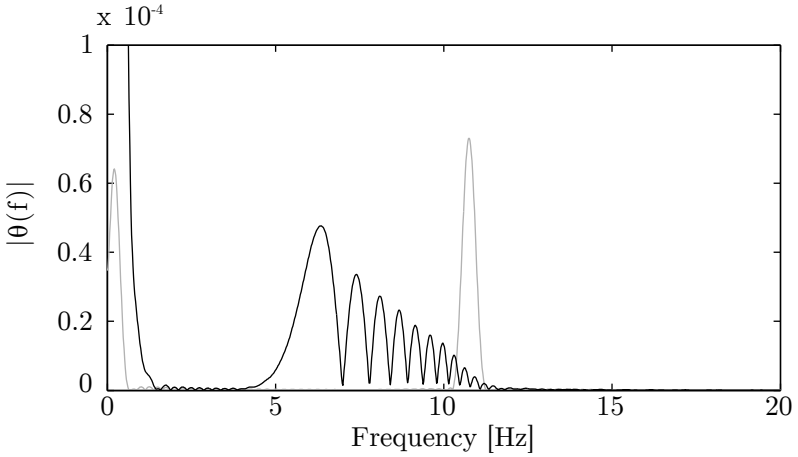

Kuva 4.23. Amplitude spectrums of simulated torque curves. The black line is the response of the fully loaded system and the semi-grey line is the unloaded system. External load cause variation in vibration frequency.

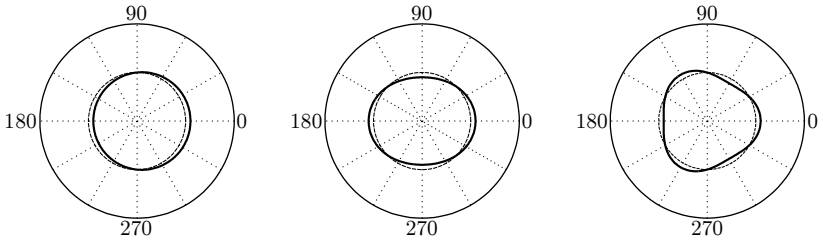

Kuva 4.24. Roundness error profiles from first to third orders respectively from the left

of the bearing housing resulting in a total of 88 DOFs. In transient analysis, large matrices are computationally expensive. Therefore, the number of DOFs to be solved were reduced using the modal reduction. The eigenvalue analysis was performed for the full finite element model. A total of eight flexible modes were considered: two pairs of rotor bending modes, and four pedestal modes where the pedestals, described as mass points and springs, have rigid motion with respect to the rest of the system. By using these modes, the effects of the pedestal flexibility and the rotor bending were considered. The corresponding frequencies of the natural vibrations are presented in Table 4.6.

The disc supported roller test rig was modeled in a commercial multibody simulation software MD Adams [49]. The simulation model included a flexible non-ideal tube roll, the support of the roll and nonlinear contact forces between the roll and the support. A more detailed description of the model can be found in Sopanen's

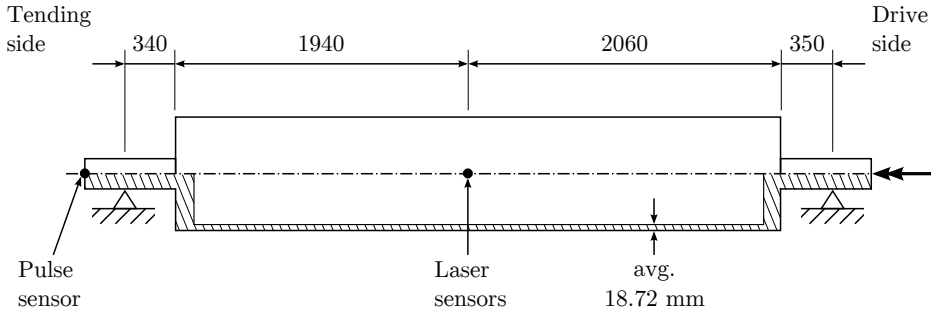

Kuva 4.25. The locations of the measurement points in millimeters. The section view of the tube roll is presented below the centerline.

Taulukko 4.6. Modes of the tube roll FE-model that are used in modal reduction

Mode type	**Frequency [Hz]**	
(b) = bending mode pair	78.2/78.2	(b)
(p) = pedestal rigid body mode	112.0/112.0	(p)
	209.6/209.6	(b)
	321.3/321.3	(p)

dissertation [68]. MD Adams uses the floating frame of reference approach in describing the flexibility of the system. The flexible parts of the system model were modeled using the finite element software ANSYS. The element type that was used in the modeling was eight-node brick-shaped solid elements with rotational degrees-of-freedom (namely SOLID73 in ANSYS). The variation in shell thickness was taken into account in the finite element model by moving nodes at the inner surface of the shell, since the outer surface was machined to achieve high quality of the end product.

Adams uses the Craig-Bampton sub-structuring method in model reduction. The used Craig-Bampton modes were solved using the finite element model. A total of 56 fixed interface modes and 12 static correction modes were used in Craig-Bampton representation. The set of modes were orthogonalized and the free-free modes and boundary modes obtained. A total of 22 bending and longitudinal modes and two boundary modes were selected from this set. The frequencies of the selected orthogonalized modes of the roll model which were used in the dynamic analysis are shown in Table 4.7. It can be seen that the first two bending mode pairs in Tables 4.6 and 4.7 are close to each other even though the model in the first studied case was very rough and the model in second case, instead, was very accurate.

Taulukko 4.7. The selected orthogonalized Graig-Bampton modes of the tube roll FE-model

Mode type	**Frequency [Hz]**	
(b) = bending mode pair	77.76/77.90	(b)
(l) = longitudinal mode	199.95/200.17	(b)
(s) = boundary mode pair	279.64/279.74	(b)
	348.53/348.65	(b)
	464.54	(l)
	523.26/523.54	(b)
	778.75/779.04	(b)
	982.45	(l)
	1054.41/1054.60	(b)
	1301.37/1301.65	(b)
	1460.24/1460.94	(b)
	1595.25/1596.37	(b)
	11941.95/11982.07	(s)

Contact Forces

In the spherical roller bearings supported rotor system, the contact forces affected between the pedestal and the rotor. The pedestals and the rotor were modeled as mass points and finite elements, respectively. The forces between bearing rings and the rollers came from the elastic deformations. The shape of the penetration was elliptic. The description of the geometric parameters of the spherical roller bearing are introduced in more detailed in [20], whereas the main parameters of the supporting spherical roller bearing are listed in the Table 4.8.

In another studied case, the support was modeled using two flexible and three rigid parts, as shown in Figure 4.26. The flexibility of the frame part and the attachment plate was described using the same approach that is used for the roll. The parts of the model were connected using spring-damper forces and kinematical constraints. A more detailed description of the modeling of the support is given in Reference [67].

The two supporting disks in Figure 4.26 were connected to the attachment plate by needle roller bearings. Neither the linear springs nor the constraint equations can be used to model this kind of support, because the roll can be lifted off the support freely. Therefore, contact forces between the roll and the support rollers have to be defined. Table 4.9 shows the contact parameters.

Taulukko 4.8. The numerical values used in the contact parameter calculation

Material:	
Free contact angle ϕ_0	8.07°
Roller diameter d_r	17.5 mm
Inner raceway contour radius r_i	93.5 mm
Outer raceway contour radius r_o	93.52 mm
Roller contour radius r_r	93.5 mm
Bearing width B_B	52 mm
Clearance c_d	41 µm
Pitch diameter d_e	165 mm
Number of rows n_z	2
Number of rolling elements in one row N	25
Young's modulus E	206 GPa
Poisson's ratio ν	0.3

Imperfections in the Systems

In the case of the spherical roller bearings supported rotor, the imperfections of the rotor were not included in the model. Even though the rotor imperfections were not modeled the subcritical vibrations could be studied since the waviness of the bearings contributed mainly to these vibrations. The waviness components of the spherical roller bearings inner rings in both rolling rows at both ends were measured and presented in Table 4.10. In the simulation model, attention was paid to the waviness components of 2^{st} to 4^{th} orders only because the amplitudes of higher components were insignificantly small. The second order waviness had the highest amplitudes. The phases of different orders of waviness were close in both rolling sides on both the tending and serving sides which increased the overall effect of waviness.

The modeling imperfection in the disc supported tube roll model were imperfections of the tube roll and the roundness errors of the supporting discs. The measured roundness profiles of the discs and the shaft are shown in Table 4.11. In the simulation model, attention was paid to the harmonic components of the 1^{st} to 4^{th} orders. It can be noted that the first order harmonic waviness dominated the overall waviness. In general, the roundness errors of the disks were distinctly smaller than those of the shafts. In addition, since the diameter of the discs were different than the diameter of the shaft and the roll could be freely lifted of from the discs, the phase angles of the discs could not be accurately defined in a straightforward manner. Therefore, the roundness error of the disks is modeled without the phase angles. The accuracy of the measurements was ± 1 µm for the shaft and ± 0.2

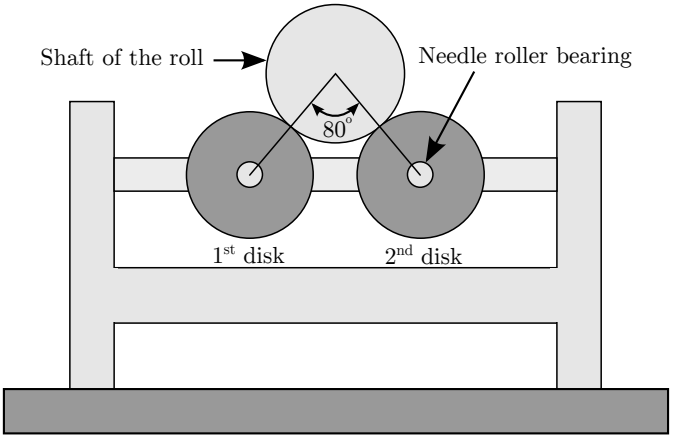

Kuva 4.26. The model of the roll and the support and the used in the simulation. Light gray colored parts are flexible and dark gray colored parts are rigid bodies.

µm for the disks. The imperfections of the tube roll were included in the finite element model that was used to define the Craig-Bampton modes.

4.3.2 Simulation Results

The simulation results of both cases studied can be compared and evaluated with respect to each other. Both simulation cases were also measured and the results can be compared with the measurements, as well. The objective of the comparison is 1) to study the effect of the supporting system to the twice running speed vibrations and 2) investigate and analyze the modeling methodology and its usability in modeling imperfect rotating devices, as well as studying the subcritical vibrations.

Response Curves

The amplitudes of the twice-running-speed response for simulation cases and measurement in horizontal direction are shown in Figure 4.27. The maximum amplitudes in horizontal direction in simulations occur at the rotation speeds between 15.4 and 15.6 in the case of the spherical roller bearings supported tube roll, and 14.6 and 15.0 Hz in the case of the disk supported tube roll.

When the results of the spherical roller bearing supported system are compared it can be seen that the responses are comparable. The frequency of the peaks are differing by 0.2 Hz which, naturally, is affected by the fact that the rotational speed increment is 0.2 Hz in both simulation and measurements. The actual peak most likely occur between the points studied, even though the shapes of the curves in both the simulated and measured cases indicate that the peak resonance is

Taulukko 4.9. The numerical values used in the contact parameter calculation

Material:	
Young's Modulus E	$2.06{\cdot}10^{11}$ Pa
Poisson's ratio ν	0.3
Contact coefficients:	
Contact stiffness coefficient k_c	0.2146 kN/ µm $^{1.2173}$
Exponent e_c	1.2173
Contact damping coefficient c_c^{max}	$2.5{\cdot}10^{-5}$ s$\cdot k_c$
Penetration depth d_c	5.0 µm
Cylinder-Cylinder contact:	
Length L_1	25.0 mm
Diameter D_1	115.0 mm
Diameter D_2	125.0 mm
Needle Roller Bearing:	
Length of the needle l_r	24.0 mm
Diametral play c_d	50.0 µm
Number of needles z	26

actually close to the observed peak value. The amplitudes of the responses differ between the simulation and the measurement. The amplitude of the simulated response curve is close to 280 µm whereas the amplitude in the measured case is 210 µm. Nonetheless, the results demonstrate that the relatively coarse finite element model combined with the modal reduction method is applicable method in simulating the twice-running-speed resonances of rotating systems.

The simulated and measured frequencies, in case of disk supported system, differ by 0.4 Hz although it can easily be seen that the peak of the simulated response curve, in reality, would occur below the observed peak value due to the shape of the curve. The measured maximum amplitude in the horizontal direction vary between 290 and 305 µm.

The results of the disk supported roll have a better agreement in response amplitudes but the frequencies are closer to each other in the case of the SRB supports. The reasons for the difference are hard to evaluate. The rotor model itself was more accurate since the imperfections of the tube were considered in the disk supported case, although they were not included in the other case. In addition, the pedestal was modeled using an accurate finite element model that corresponds well with the test rig. Most likely, the difference comes from the description of the support. If the response curves of both cases studied are compared then the frequencies of the response peak seem highly affected by the support system components since the frequencies of the peak responses clearly differ among the cases studied. It is also noticable that in both cases the simulated response curves has higher frequencies

Taulukko 4.10. Bearing inner ring waviness components of orders $2nd$ to $4th$

	Tending side			
	Inner rolling race		**Outer rolling race**	
k	Amplitude c_k[µm]	Phase ϕ_k[rad]	Amplitude c_k[µm]	Phase ϕ_k[rad]
2	5.11	6.1348	4.67	6.0895
3	1.04	4.0991	1.66	3.6675
4	1	2.7613	0.47	2.5983

	Drive side			
	Inner rolling race		**Outer rolling race**	
k	Amplitude c_k[µm]	Phase ϕ_k[rad]	Amplitude c_k[µm]	Phase ϕ_k[rad]
2	2.41	6.2240	2.7	6.0404
3	0.91	0.4465	0.9	0.6302
4	0.21	1.5940	0.39	3.3379

and larger amplitudes. The shapes of the each curve are comparable with each other and this indicates that the damping in the simulation models is accurately defined. It can be said that both of the simulation models can accurately predict the twice-running-speed resonances.

Spectrum Maps

The simulation results of the vibrations can also be compared to the measurement results by using spectrum maps of the displacements. The spectrum maps include the frequency of the twice-running-speed resonance as ranging between 14 and 18 Hz in case of SRB supported tube roll, and 10 and 20 Hz in case of disk supported tube roll. The spectrum maps are presented in linear and logarithmic scale for both vertical and horizontal directions. The spectrum maps of the spherical roller bearing supported system are presented at first, and then the results of the disk supported system.

The measured and simulated spectrum maps of the SRB supported tube roll in the horizontal direction in the linear scale are depicted in Figure 4.28. The corresponding spectrum maps in the logarithmic scale are shown in Figure 4.29. The vertical spectrum maps are shown in Figures 4.30 and 4.31 having the linear and the logarithmic scale, respectively.

The simulated spectrum maps show all modeled excitations. The measured tube roll was balanced to meet the standards, but there some imbalance remains, as can be noted from the first harmonic component of the displacement. All excitations from the bearings can be seen as clear responses in the figures with the logarithmic

Taulukko 4.11. The measured roundness errors of the shafts and disks

Shaft of the Roll				
	Drive side		**Tending side**	
k	Amplitude c_k[µm]	Phase ϕ_k[rad]	Amplitude c_k[µm]	Phase ϕ_k[rad]
1	31.89	0.6021	43.38	5.2360
2	2.75	0.0349	4.05	0.0873
3	0.50	1.4312	0.35	1.1170
4	0.20	1.3963	0.25	0.2443

Disks				
	Drive side		**Tending side**	
	Amplitude c_k[µm]		Amplitude c_k[µm]	
k	First disk	Second disk	First disk	Second disk
1	2.50	4.00	2.00	2.00
2	0.20	0.25	0.15	0.15
3	0.10	–	–	–

z-axes. This indicates that the simulation model is able to account for the bearing roundness errors of the 2^{nd} to 4^{th} orders.

The amplitudes of the horizontal second harmonics are greater than those of the vertical ones in all cases (simulated or measured). This is caused by the support of the roll, the stiffness of which in the horizontal direction is less than that in the vertical direction. When the simulated and measured results are compared, the twice-running-speed resonance can be found at the expected rotational speed in both the horizontal and vertical directions. The response amplitude in the horizontal direction is greater in the simulated case than in the measured one. In the vertical direction, the measured amplitude of the response is as much as three times higher than the experimentally measured one in the resonance. The difference is most likely caused by the description of the pedestal supporting the bearing housing. In the simulated case, the resonance is found in both the vertical and horizontal directions at the rotational speed frequency that is close to the measured rotational speed frequency in the resonance. However, the amplitude of the vibration is not achieved accurately in the vertical direction. Some of the difference in the resonance amplitudes can be attributed to the rotational speed increment of 0.2 Hz, which means that most likely the exact resonance frequency of the system has not been found, and the amplitude is diminished from the actual resonance peak in both the simulation and the experimental measurements. Nevertheless, it can be concluded that the simulation model is capable of accurately predicting the system disturbances originating from the waviness of the bearings.

The measured and simulated spectrum maps of the horizontal displacements in the case of the disk supported tube roll are shown in Figures 4.32 and 4.33 in linear

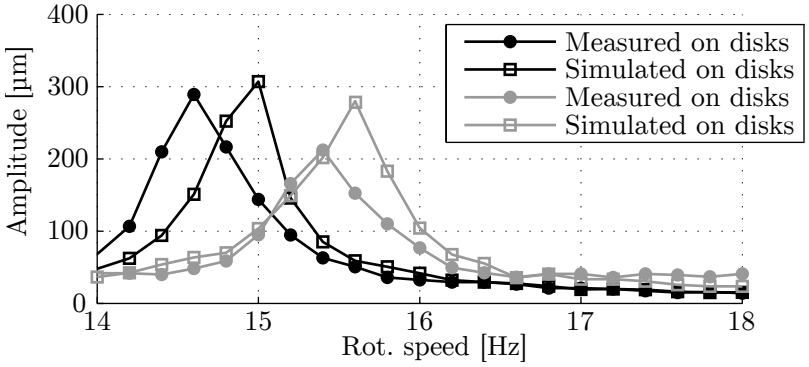

Kuva 4.27. Simulated and measured twice-running speed response amplitudes as functions of rotational speeds studied. Black lines are the response amplitudes of the disk supported tube roll, and grey lines are the response amplitudes of the SRB supported tube roll.

and logarithmic scale, respectively. Similarly, the corresponding spectrum maps in vertical directions are shown in Figures 4.34 and 4.35 in the linear and logarithmic scale, respectively. All the modeled excitations can be seen in the simulated spectrum maps as well. The first harmonic component of the displacement can be clearly seen as response that is arising from the mass imbalance. However, the amount of imbalance does not affect the higher harmonic components, and thus, unbalance is not considered in this study. The amplitudes of the horizontal second harmonics are greater than those of the vertical ones in all the simulation cases as well as in the measurements which can be observed from the response curves as well. This is caused by the support of the roll and the second order waviness of the shaft. It can be seen in Figure 4.26 that the angle between the disks is 80°. When the elliptical shaft rotates on this kind of a support, the first contact is in the upper phase and the second one in the lower phase of waviness, which causes larger excitation in the horizontal than in the vertical direction; furthermore, the support is more flexible in horizontal direction. The horizontal twice-running-speed resonance can also be seen from the spectrum maps of the vertical displacements as a disturbance in the spectrum.

A three-times-running-speed resonance (3X-resonance) and higher orders can be clearly observed from the figures having logarithmic scales. These resonances can be seen clearly in both the simulated and measured spectra, although the measured results in the linear scale do not reveal the resonance and the measured response magnitudes of the higher order resonances are less than those simulated. The simulated resonance amplitudes are large in comparison to the twice-running-speed resonance, because the third-order amplitudes of the waviness are less than 1 µm, whereas the second-order amplitudes are 2-4 µm. The reason for the high response

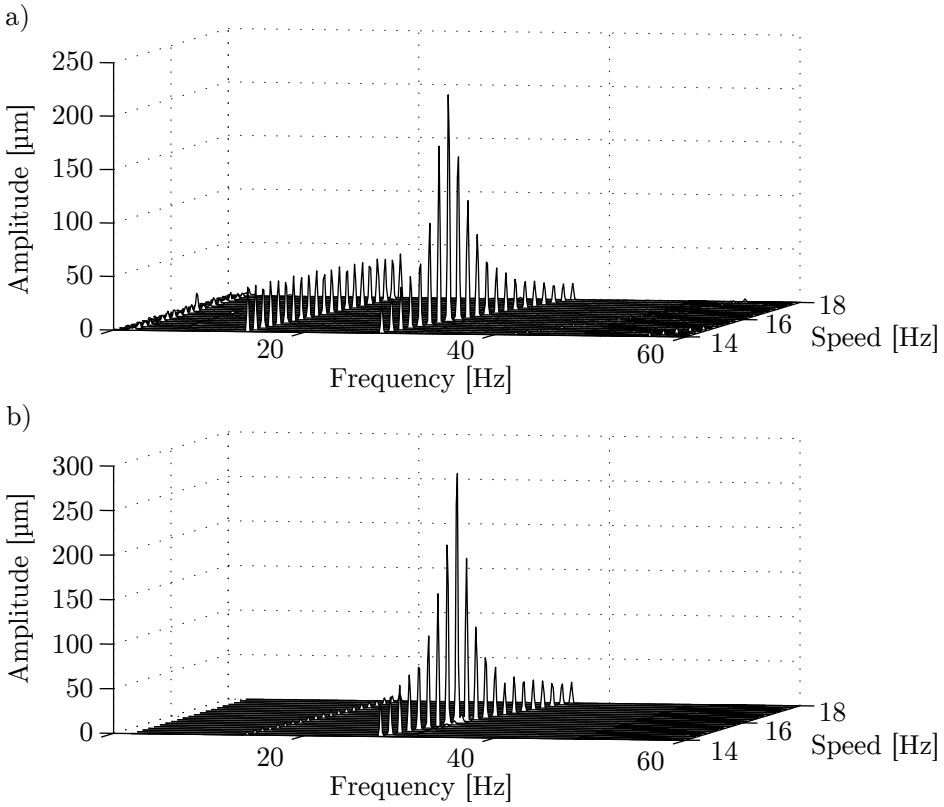

Kuva 4.28. a) Measured and b) simulated vibrations of the SRB supported tube roll in the horizontal direction in the linear scale

in the simulation results is probably caused by the type of support of the roll. When the triangular shaft rotates on this kind of a support, both contacts are near the upper phases of waviness. After the roll has rotated 30°, both contacts of the roll are in the lower phases waviness, respectively. This causes a larger movement in the vertical direction than does equal-sized second-order waviness.

When the support cases are compared it can be seen that that all the excitation components from the 1^{st} to 4^{th} orders can be observed. In the second case studied, the eccentricity was included in the descriptions of disks and shaft waviness that was neglected in the first studied case. In general, the simulated response spectra has more clear responses of higher orders of imperfections when compared with the measured spectra. The higher order resonances can also be seen from the measured spectra, but the amplitudes are not very high. On the other hand, in the measured response spectra shown in the logarithmic scale, there are clear noise signals included that have some effect on the clarity of the curves.

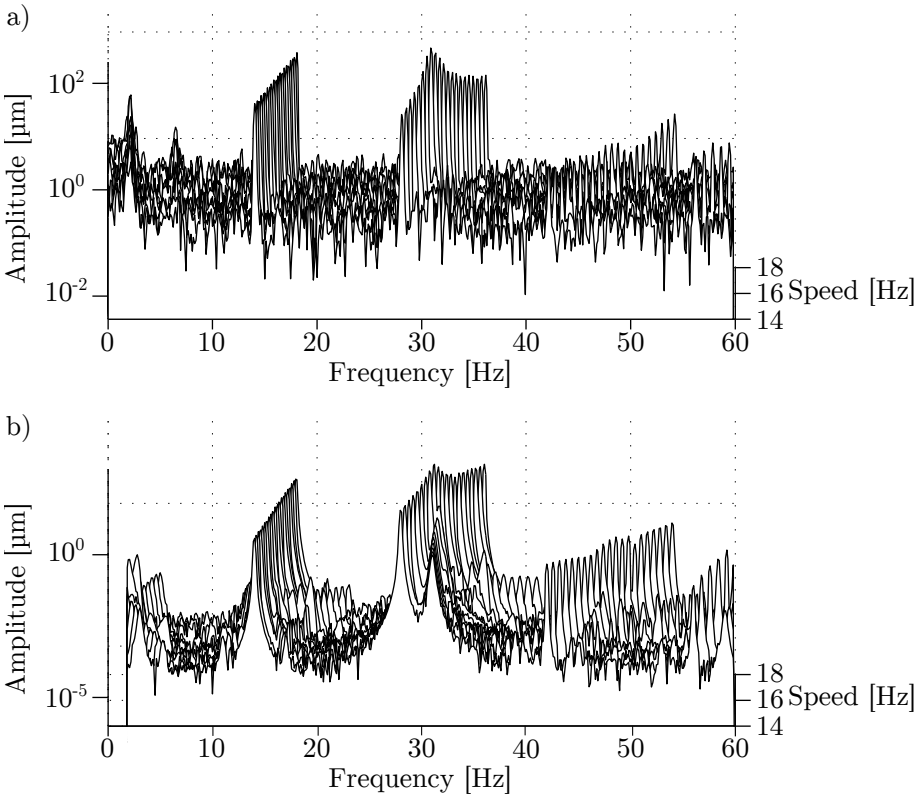

Kuva 4.29. a) Measured and b) simulated vibrations of the SRB supported tube roll in the horizontal direction in the logarithmic scale

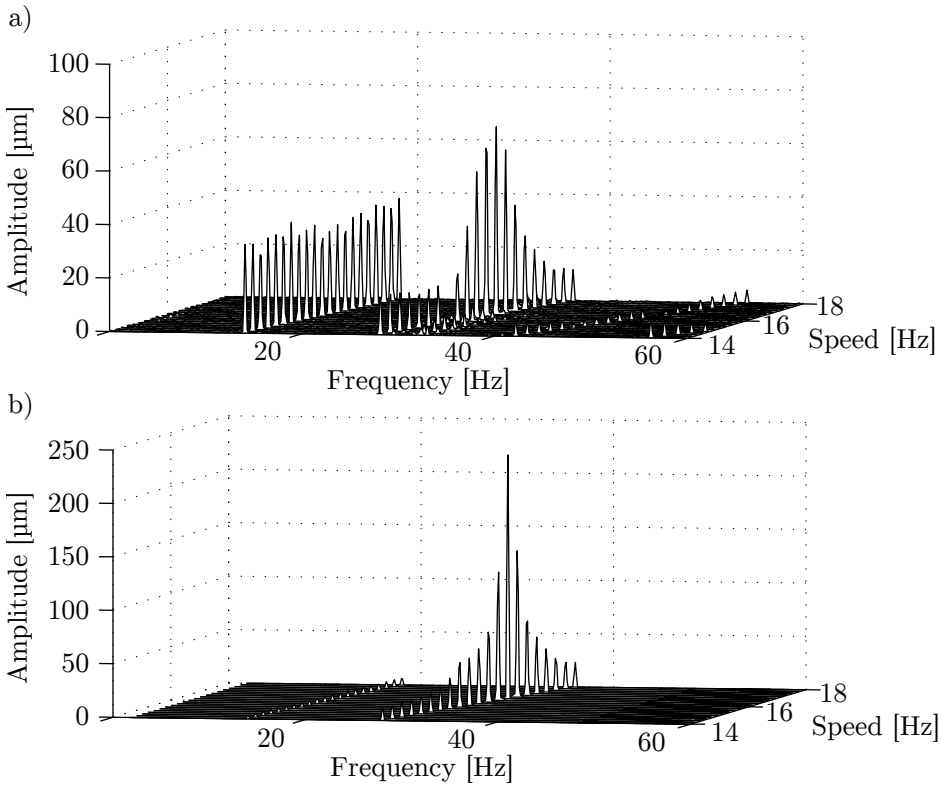

Kuva 4.30. a) Measured and b) simulated vibrations of the SRB supported tube roll in the vertical direction in the linear scale

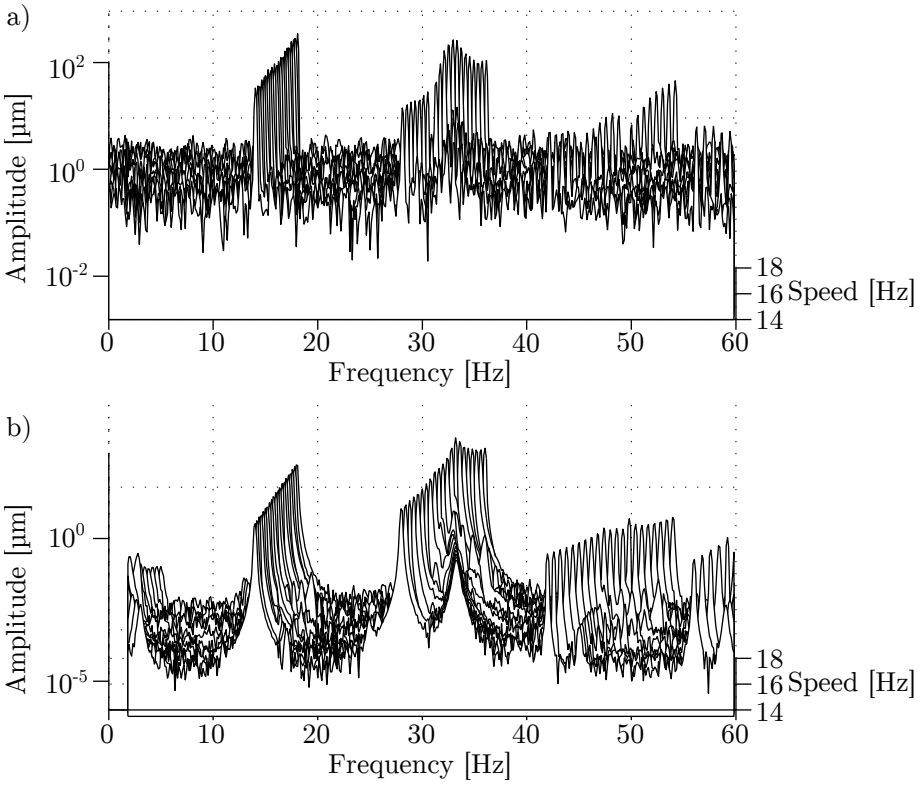

Kuva 4.31. a) Measured and b) simulated vibrations of the SRB supported tube roll in the vertical direction in the logarithmic scale

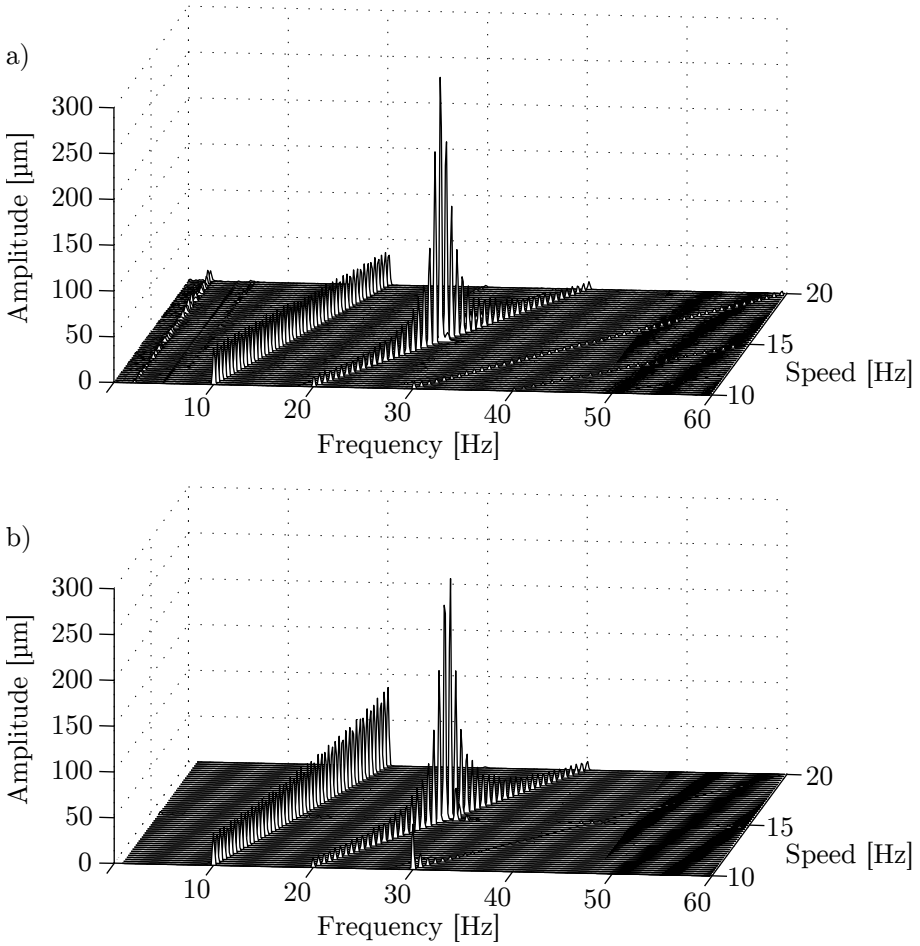

Kuva 4.32. a) Measured and b) simulated vibrations of the disk supported roll in the horizontal direction in the linear scale

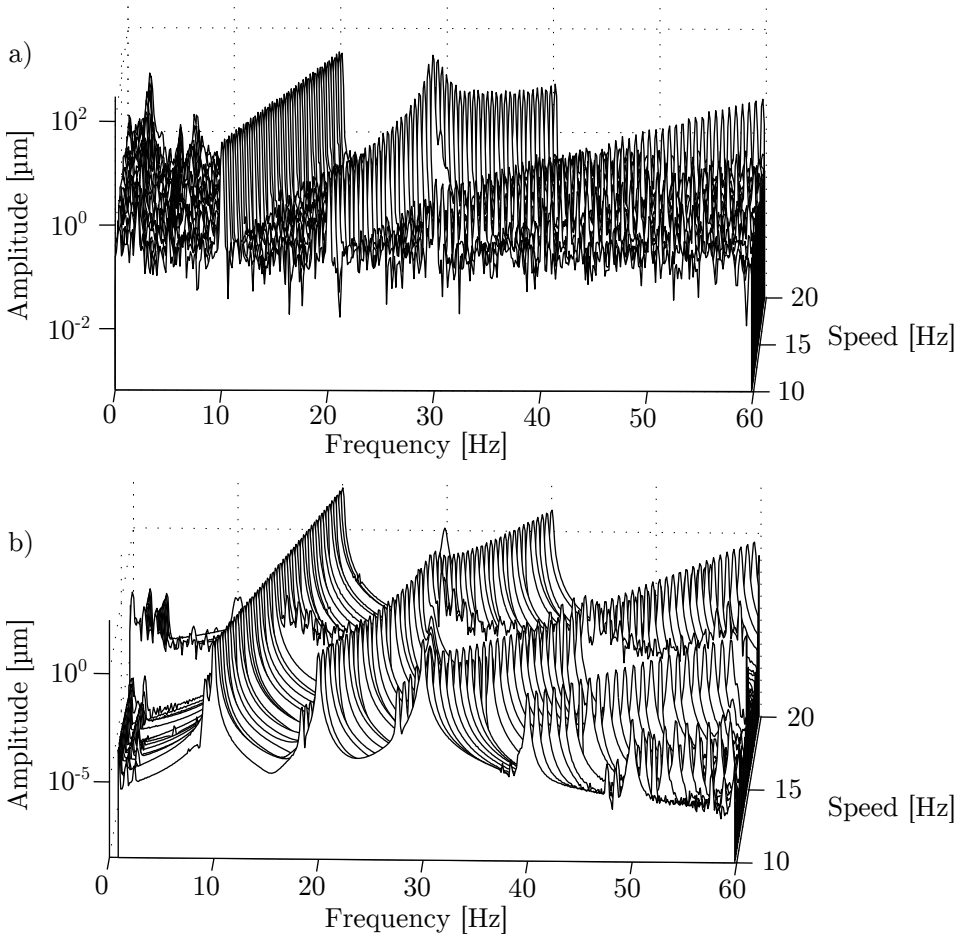

Kuva 4.33. a) Measured and b) simulated vibrations of the disk supported roll in the horizontal direction in the logarithmic scale

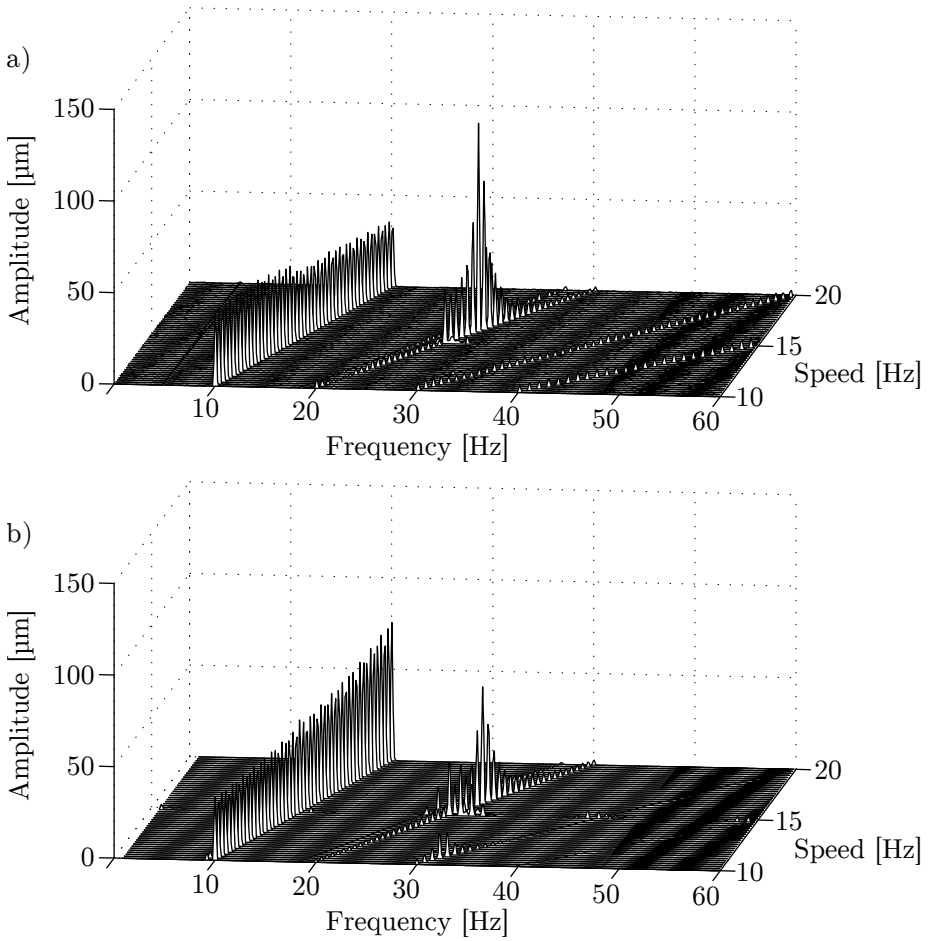

Kuva 4.34. a) Measured and b) simulated vibrations of the disk supported roll in the vertical direction in the linear scale

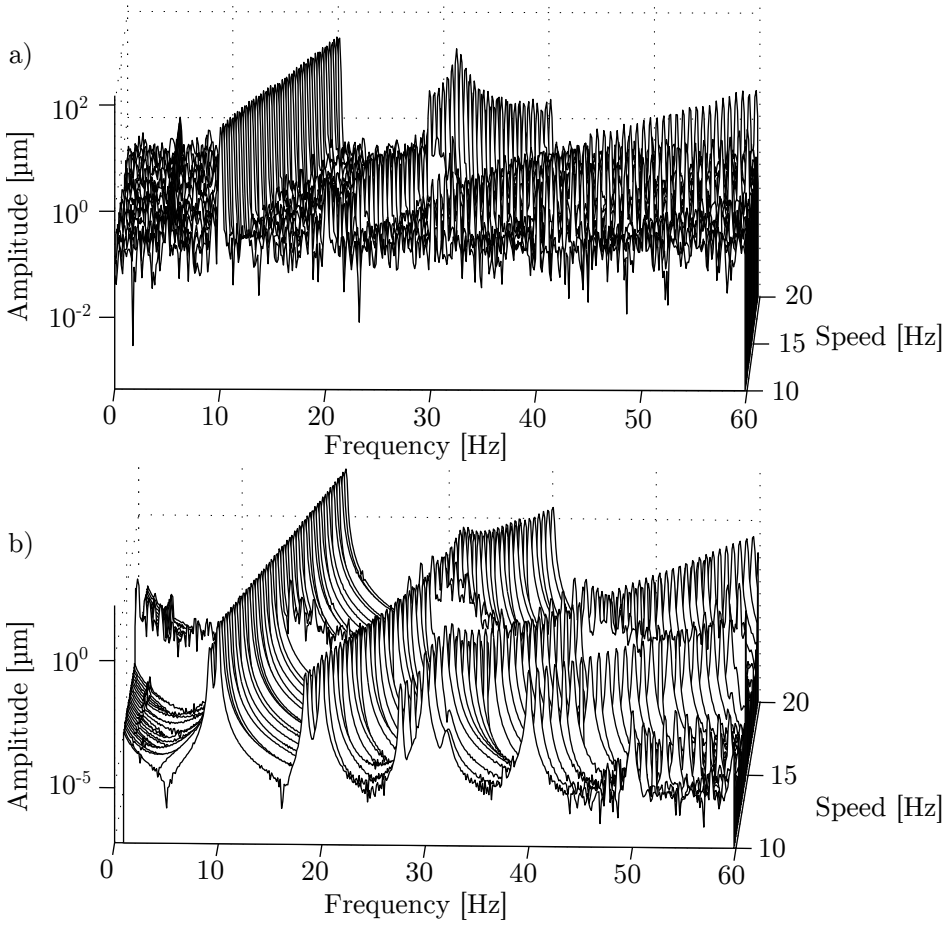

Kuva 4.35. a) Measured and b) simulated vibrations of the disk supported roll in the vertical direction in the logarithmic scale

Luku 5

Conclusions

The dissertation demonstrates the effects of imperfections arising from the manufacturing and assembling inaccuracies in rotating machines. Particularly, two types of rotating permanent magnet machines and a paper machine tube roll supported by two different methods have been introduced. The typical manufacturing methods cause some imperfections in the mechanical systems. In electric machines, the imperfections as well as the typical electromagnetic characteristics cause excitations that may excite the system to vibrate at the resonance frequency. In the case of paper machine tube roll studied, the excitations arose from the support structure and the vibrations were magnified by the uneven mass and stiffness distribution of the roll.

In the first case studied, a dynamic model of a direct-driven wind turbine with a permanent magnet synchronous generator was proposed. The model was used to study the torsional vibrations of the drive train under electromagnetic excitations. Two different permanent magnet generator rotor constructions were studied and analyzed. The cogging torque and torque ripple amplitudes of the different constructions were calculated and incorporated into the mechanical vibration model. The evaluated results consist of the steady state responses and transient responses during the start-up of the wind turbine at low wind speed.

The results show that another permanent magnet generator construction studied; namely the generator rotor with rectangular magnets buried inside a rotor lamination stack producing a sinusoidal air gap flux density, placed in two rows that were shifted by half a stator slot pitch from each other, is suitable for the studied system. The generator rotor construction with a rectangular rotor surface magnet construction placed in two rows that were shifted by half stator slot pitch from each other proved barely acceptable.

According to the calculations, the maximum allowable value of the cogging torque of a direct-driven permanent magnet wind generator is 1.5–2 % of the rated torque even when the corresponding resonance frequency does not occur in the operational speed range of the wind turbine. Furthermore, it was noticed that the resonance caused by the excitation torque should occur at the lowest possible speed. In the case of the system studied, this means that the cogging torque at $12f_s$ is not as harmful as the one occurring at $6f_s$. This observation favors permanent magnet skewing, or using at least two sets of magnets shifted tangentially from each other, as is the case in this study. In the system studied, the resonances caused by the torque ripple harmonics were not a significant design concern.

In the second case studied, a special application for wave energy harvesting was investigated in terms of rotor vibrations. The device is trans-rotary magnetic gear and it is referred to as TROMAG. It was modeled using the finite element method and the electromagnetic forces were defined using analytical equations and the finite element method. Torsional vibrations and how they are influenced by the number of magnetic poles and the air gap size were studied in details. In addition, translational vibrations and how it is influenced by small deviations in the roundness and concentricity of the rotor were investigated. The analysis results have been presented in both the time and the frequency domains.

The idealized TROMAG consists of a long tubular translator, and short and concentric inner rotor. The thin wall tubular translator supported on both ends is flexible and prone to bending. The imperfect geometries studied included a dynamically and statically eccentric rotor. The dynamically eccentric rotor coupled with a statically eccentric translator results in an excitation component with a frequency equal to the rotational speed. The tangential permanent magnet forces drive the rotor and produce its torque. The interaction is analogous to a non-linear spring situated between the translator and rotor. The PM forces cause the rotor to oscillate constantly close to the equilibrium state. The number of magnetic poles affects the amplitude of the oscillation. Without active damping or control, permanent magnet forces induce rotor oscillation at the frequency, which is proportional to the number of magnetic poles.

In the third study, the vibrations of a paper machine tube roll were investigated. The tube roll was studied with two different supports: spherical roller bearings and freely rotating discs on both ends. The study was mostly concerned with the twice-running-speed vibrations that occur below the operational rotation speed. Vibrations, including subcritical ones, have to be taken into account in applications such as paper machines in which the vibrations can influence the quality of the final product.

The rotor system was studied using two different simulation approaches. In the first simulation, the rotor was modeled using the finite element method, and the

rotor model did not include the uneven mass and stiffness distribution that were measured in the test rotor. The supporting system in this case were spherical roller bearings on pedestals. The bearings were modeled as forces that were defined using the Hertzian nonlinear contact theory. The bearings were measured and some roundness error was observed from the measurement results. The roundness errors were emulated in the bearing force description where the wavy rotor caused a varying force as a function of the rotor phase angle.

The disc supported tube roll was modeled using the flexible multibody simulation approach where the flexibility of the roll was modeled using the floating frame of reference formulation. In this case, the uneven mass and stiffness distribution of the tube roll was emulated into the finite element model that was used in describing the flexibility of the roll. The contact between the roll and the supporting disc structure, in which the discs have some measured roundness errors, was also modeled as forces defined using the Hertzian contact theory.

A set of spectrum maps depict measured and simulated vibrations in both the vertical and horizontal directions in both simulated cases. The results showed clear correspondence: the frequency at which the system strikes the resonance is similar in both the measurements and simulations. The results indicate that the subcritical vibrations that arise at half of the expected resonance frequency, can be obtained using both modeling methods. The more imprecise finite element model with spherical roller bearings showed clear responses in the subcritical operational speed range; this was expected based on the measurements that were carried out in the laboratory. The model did not include the imperfections in the tube roll and the only excitations in the system were the varying bearing forces. The results were close to those measured, but especially in the response amplitudes there was some mismatching. The simulation results of the more accurately modeled disc supported tube roll correspond well with the measured results in both resonance frequency and response amplitude.

Both of the methods studied are applicable for investigating the subcritical vibrations of the rotating systems. The former method is computationally cheaper but the accuracy suffers. The latter method can accurately predict the subcritical vibrations but modeling and emulating the measured results into the simulation model is rather complex.

Future Work

The main focus of future work in this field of analyzing the vibrations in imperfect rotating machinery should concentrate on additional disturbances, and unexpected impacts and excitations in the system. The proposed wind generator model could be extended to also include the excitations caused by the turbine blade vibrations,

and the power electronic converter. Moreover, the short-circuit situations of the power controller could be studied using the proposed model.

The development of the TROMAG itself is in the early stage and there is considerable work to do in every related field. From a dynamics viewpoint, the rotor-translator system studied is just the core of the wider energy conversion system. In addition, the drive train of the conversion system from the linear motion of the buoy to the electricity generating generator could be studied more accurately. The structure of the device should also be reconsidered from the structural and dynamical perspectives and the energy production of the system could be estimated taking into consideration the dynamics of the system as regards electrical performance.

The methodology that is used to study the paper machine tube roll should be further developed. The uneven mass and stiffness distribution could be considered in modeling using the description of asymmetry in the finite elements. The methods for investigating the stability and steady state responses of asymmetric rotors are introduced in the literature. These methods could be implemented into the transient analysis.

[1] Agrawal, O. P., and Shabana, A. A. Dynamic analysis of multibody systems using component modes. *Computers & Structures 21*, 6 (1985), 1303–1312.

[2] Bianchi, N., and Lorenzoni, A. Permanent magnet generators for wind power industry: an overall comparison with traditional generators. In *International Conference on Opportunities and Advances in International Electric Power Generation* (1996).

[3] Boesing, M., Schoenen, T., Kasper, K., and De Doncker, R. Vibration synthesis for electrical machines based on force response superposition. *IEEE Transactions on Magnetics 46*, 8 (2010), 2986–2989.

[4] Bracikowski, N., Hecquet, M., Brochet, P., and Shirinskii, S. V. Multiphysics modeling of a permanent magnet synchronous machine by using lumped models. *IEEE Transactions on Industrial Electronics 59*, 6 (2012), 2426–2437.

[5] Brewe, D. E., and Hamrock, B. J. Simplified solution for elliptical-contact deformation between two elastic solids. *Journal of Lubrication Technology 99* (1977), 485–487.

[6] Cao, M., and Xiao, J. A comprehensive dynamic model of double-row spherical roller bearing – model development and case studies on surface defects, preloads, and radial clearance. *Mechanical Systems and Signal Processing 22*, 2 (2008), 467–489.

[7] Chen, W. J., and Gunter, E. J. *Introduction to Dynamics of Rotor-Bearing Systems*. Trafford Publishing, 2005.

[8] Childs, D. W. Fractional-frequency rotor motion due to non-symmetric clearance effects. *Journal of Engineering for Power 104* (1982), 533–541.

[9] Childs, D. W. Twice-running-speed response due to elliptical bearing clearances. *Journal of Vibration and Acoustics 125*, 1 (2003), 64–67.

[10] Chin, Y., Kanninen, P., Maki-Ontto, P., Sakki, R., and Lendenmann, H. Phenomenon of magnetic force in permanent magnet wind turbine generators. In *International Conference on Electrical Machines and Systems (ICEMS2009)* (2009).

[11] Coenen, I., van der Giet, M., and Hameyer, K. Manufacturing tolerances: Estimation and prediction of cogging torque influenced by magnetization faults. *IEEE Transactions on Magnetics 48*, 5 (2012), 1932–1936.

[12] Craig, R. R., and Bampton, M. C. C. Coupling of substructures for dynamic analyses. *AIAA Journal 6*, 7 (1968), 1313–1319.

[13] Dorrell, D. Experimental behaviour of unbalanced magnetic pull in 3-phase induction motors with eccentric rotors and the relationship with tooth saturation. *IEEE Transactions on Energy Conversion 14*, 3 (1999), 304–309.

[14] Ehrich, F. Observations of subcritical superharmonic and chaotic response in rotordynamics. *Journal of Vibration and Acoustics 114*, 1 (1992), 93–100.

[15] Fang, C., Xu, H., Xue, S., and Xue, S. Research on vibration characteristics of rotor of high speed permanent magnet synchronous machine. In *15th International Conference on Electrical Machines and Systems (ICEMS)* (2012).

[16] Friberg, O. A method for selecting deformation modes in flexible multibody dynamics. *International Journal for Numerical Methods in Engineering 32*, 8 (1991), 1637–1655.

[17] Ganesan, R. Effects of bearing and shaft asymmetries on the instability of rotors operating at near-critical speeds. *Mechanism and Machine Theory 35* (2000), 737–752.

[18] Gasparin, L., Cernigoj, A., Markic, S., and Fiser, R. Additional cogging torque components in permanent-magnet motors due to manufacturing imperfections. *IEEE Transactions on Magnetics 45*, 3 (2009), 1210–1213.

[19] Genta, G. *Dynamics of Rotating Systems.* Mechanical Engineering Series. Springer, 2005.

[20] Ghalamchi, B., Sopanen, J., and Mikkola, A. Simple and versatile dynamic model of spherical roller bearing. *International Journal of Rotating Machinery 2013* (2013).

[21] Hairer, E., Nørsett, S., and Wanner, G. *Solving Ordinary Differential Equations I: Nonstiff Problems.* Springer, 1993.

[22] Hamrock, B. J. *Fundamentals of Fluid Film Lubrication.* McGraw–Hill, 1994.

[23] Hamrock, B. J., and Dowson, D. Isothermal elastohydrodynamic lubrication of point contacts: Part 1 - theoretical formulation. *Journal of Lubrication Technology 98* (1976), 223–228.

[24] Harsha, S. P. Non-linear dynamic response of a balanced rotor supported on rolling element bearings. *Mechanical Systems and Signal Processing 19*, 3 (2005), 551–578.

[25] Harsha, S. P. Nonlinear dynamic analysis of a high-speed rotor supported by rolling element bearings. *Journal of Sound and Vibration 290*, 1–2 (2006), 65–100.

[26] Harsha, S. P. Nonlinear dynamic response of a balanced rotor supported by rolling element bearings due to radial internal clearance effect. *Mechanism and Machine Theory 41*, 6 (2006), 688–706.

[27] Harsha, S. P., Sandeep, K., and Prakash, R. Non-linear dynamic behaviors of rolling element bearings due to surface waviness. *Journal of Sound and Vibration 272*, 3–5 (2004), 557–580.

[28] Heikkinen, J., Ghalamchi, B., Sopanen, J., and Mikkola, A. Twice-running-speed resonances of a paper machine tube roll supported by spherical roller bearings – analysis and comparison with experiments. In *Proceedings of the ASME 2014 International Design Engineering Technical Conferences (IDETC2014)* (2014).

[29] Heikkinen, J. E., and Pakdelian, S. Rotordynamics of a trans-rotary magnetic gear rotor. In *Proceedings of the ASME 2013 International Mechanical Engineering Congress & Exposition IMECE2013* (2013), ASME.

[30] Heikkinen, J. E., Sopanen, J. T., Ruuskanen, V. V., and Nerg, J. K. Dynamic analysis of a direct-driven permanent magnet generator drive train including flexible turbine blades. In *Proceedings of the ASME 2011 International Design Engineering Technical Conferences (IDETC2011)* (2011).

[31] Hertz, H. Ueber die Berührung fester elastischer Körper. *Journal für die reine und angewandte Mathematik 1882*, 92 (1882), 156–171.

[32] Holm, R. K., Berg, N. I., Walkusch, M., Rasmussen, P. O., and Hansen, R. H. Design of a magnetic lead screw for wave energy conversion. In *XXth International Conference on Electrical Machines (ICEM)* (2012).

[33] Ishida, Y., and Inoue, T. Internal resonance phenomena of the Jeffcott rotor with nonlinear spring characteristics. *Journal of Vibration and Acoustics 126*, 4 (2004), 476–484.

[34] Islam, M., Mir, S., and Sebastian, T. Issues in reducing the cogging torque of mass-produced permanent-magnet brushless DC motor. *Industry Applications, IEEE Transactions on 40*, 3 (2004), 813–820.

[35] Jang, G., and Jeong, S.-W. Nonlinear excitation model of ball bearing waviness in a rigid rotor supported by two or more ball bearings considering five degrees of freedom. *Journal of Tribology 124*, 1 (2002), 82–90.

[36] Jang, G., and Jeong, S.-W. Analysis of a ball bearing with waviness considering the centrifugal force and gyroscopic moment of the ball. *Journal of Tribology 125*, 3 (2003), 487–498.

[37] Jang, G., and Jeong, S.-W. Vibration analysis of a rotating system due to the effect of ball bearing waviness. *Journal of Sound and Vibration 269*, 3 (2004), 709–726.

[38] Kang, Y., Shih, Y.-P., and Lee, A.-C. Investigation on the steady-state responses of asymmetric rotors. *Journal of Vibration and Acoustics 114* (1992), 194–208.

[39] Khulief, Y. A., and Mohiuddin, M. A. On the dynamic analysis of rotors using modal reduction. *Finite Elements in Analysis and Design 26* (1997), 41–55.

[40] Kim, T.-J., Hwang, S.-M., Kim, K.-T., Jung, W.-B., and Kim, C.-U. Comparison of dynamic responses for ipm and spm motors by considering mechanical and magnetic coupling. *IEEE Transactions on Magnetics 37*, 4 (2001), 2818–2820.

[41] Kowal, D., Dupre, L., Sergeant, P., Vandenbossche, L., and De Wulf, M. Influence of the electrical steel grade on the performance of the direct-drive and single stage gearbox permanent-magnet machine for wind energy generation, based on an analytical model. *IEEE Transactions on Magnetics 47*, 12 (2011), 4781–4790.

[42] Krämer, E. *Dynamics of Rotors and Foundations*. Springler-Verlag, Berlin, 1993.

[43] Lalanne, M., and Ferraris, G. *Rotordynamics Prediction in Engineering.* John Wiley, 1998.

[44] Lazarus, A., Prabel, B., and Combescure, D. A 3D finite element model for the vibration analysis of asymmetric rotating machines. *Journal of Sound and Vibration 329*, 18 (2010), 3780–3797.

[45] Li, H., and Chen, Z. Transient stability analysis of wind turbines with induction generators considering blades and shaft flexibility. In *33rd Annual Conference of the IEEE Industrial Electronics Society (IECON2007)* (2007).

[46] Lindh, P., Jussila, H., Niemelä, M., Parviainen, A., and Pyrhönen, J. Comparison of concentrated winding permanent magnet motors with embedded and surface-mounted rotor magnets. *IEEE Transactions on Magnetics 45*, 5 (2009), 2085–2089.

[47] Liqin, W., Li, C., Dezhi, Z., and Le, G. Nonlinear dynamics behaviors of a rotor roller bearing system with radial clearances and waviness considered. *Chinese Journal of Aeronautics 21*, 1 (2008), 86–96.

[48] McDonald, A. S., Mueller, M. A., and Polinder, H. Structural mass in direct-drive permanent magnet electrical generators. *IET Renewable Power Generation 2*, 1 (2008), 3–15.

[49] MSC Software. *MD ADAMS 2010/Theory of Flexible Bodies*, 2010.

[50] Nelson, H. D., and McVaugh, J. M. The dynamics of rotor-bearing systems using finite elements. *ASME Journal of Engineering for Industry 98*, 2 (1976), 593–600.

[51] Özgüven, H. N., and Özkan, Z. Whirl speeds and unbalance response of multibearing rotors using finite elements. *Journal of Vibration, Acoustics, Stress, and Reliability in Design 106*, 2 (1984), 72–79.

[52] Pakdelian, S., Deshpande, Y., and Toliyat, H. A. An electric machine integrated with trans-rotary magnetic gear. In *IEEE Energy Conversion Congress and Exposition (ECCE)* (2012).

[53] Pakdelian, S., Frank, N. W., and Toliyat, H. A. Analysis and design of the trans-rotary magnetic gear. In *IEEE Energy Conversion Congress and Exposition (ECCE)* (2012).

[54] Pakdelian, S., Frank, N. W., and Toliyat, H. A. Principles of the trans-rotary magnetic gear. *IEEE Transactions on Magnetics 49*, 2 (2013), 883–889.

[55] Pyrhönen, J., Jokinen, T., and Hrabovcová, V. *Design of Rotating Electrical Machines*. John Wiley & Sons, Ltd, 2008, p. 538.

[56] Pyrhönen, J., Kurronen, P., and Parviainen, A. Permanent magnet 3 mw low-speed generator development. In *Proceedings of International Conference on Electrical Machines* (2006).

[57] Rahman, M. A., Masrur, M. A., and Uddin, M. N. Impacts of interior permanent magnet machine technology for electric vehicles. In *IEEE International Electric Vehicle Conference (IEVC)* (2012).

[58] Ramtharan, G., Jenkins, N., Anaya-Lara, O., and Bossanyi, E. Influence of rotor structural dynamics representations on the electrical transient performance of FSIG and DFIG wind turbines. *Wind Energy 10*, 4 (2007), 293–301.

[59] Rao, J. S. *Rotor Dynamics*. Wiley Eastern Limited, New Delhi, 1983.

[60] Schwertassek, R., Wallrapp, O., and Shabana, A. A. Flexible multibody simulation and choice of shape functions. *Nonlinear Dynamics 20* (1999), 361–380.

[61] Shabana, A. A. Resonance conditions and deformable body co-ordinate systems. *Journal of Sound and Vibration 192*, 1 (1996), 389–398.

[62] Shabana, A. A. *Dynamics of Multibody Systems*, 3 ed. John Wiley & Sons, New York, 2005.

[63] Shen, G., Xiao, Z., Zhang, W., and Zheng, T. Nonlinear behavior analysis of a rotor supported on fluid-film bearings. *Journal of Vibration and Acoustics 128*, 1 (2006), 35–40.

[64] Shi, M., Wang, D., and Zhang, J. Nonlinear dynamic analysis of a vertical rotor-bearing system. *Journal of Mechanical Science and Technology 27*, 1 (2013), 9–19.

[65] Smith, A., and Edey, K. Influence of manufacturing processes on iron losses. In *Seventh International Conference on Electrical Machines and Drives* (1995).

[66] Soleimani, J., Bafghi, M. B., and Shojaeepoor, M. IPM synchronous motor for traction applications: Performance analysis considering hysteresis loop characteristics variation. *International Review of Electrical Engineering 7*, 1 (2012), 3297–3303.

[67] Sopanen, J. Multibody simulation model of the roller test rig. Tech. rep., Lappeenranta University of Technology, Department of Mechanical Engineering, 2003.

[68] Sopanen, J. *Studies of Rotor Dynamics Using a Multibody Simulation Approach.* PhD thesis, Lappeenranta University of Technology, 2004.

[69] Sopanen, J., Heikkinen, J., and Mikkola, A. Experimental verification of a dynamic model of a tube roll in terms of subcritical superharmonic vibrations. *Mechanism and Machine Theory 64* (2013), 53–66.

[70] Sopanen, J., and Mikkola, A. Dynamic model of a deep-groove ball bearing including localized and distributed defects. Part 1: Theory. *Proceedings of the Institution of Mechanical Engineers, Part K: Journal of Multi-body Dynamics 217*, 3 (2003), 201–211.

[71] Sopanen, J., and Mikkola, A. Dynamic model of a deep-groove ball bearing including localized and distributed defects. Part 2: Implementation and results. *Proceedings of the Institution of Mechanical Engineers, Part K: Journal of Multi-body Dynamics 217*, 3 (2003), 213–223.

[72] Sopanen, J., Ruuskanen, V., Nerg, J., and Pyrhönen, J. Dynamic torque analysis of a wind turbine drive train including a direct-driven permanent-magnet generator. *IEEE Transactions on Industrial Electronics 58*, 9 (2011), 3859–3867.

[73] Sunnersjö, C. S. Rolling bearing vibrations - the effects of geometrical imperfections and wear. *Journal of Sound and Vibration 98*, 4 (1985), 455–474.

[74] Swann, S. Effect of rotor eccentricity on the magnetic field in the air-gap of a non-salient-pole machine. *Electrical Engineers, Proceedings of the Institution of 110*, 5 (1963), 903–915.

[75] Tandon, N., and Choudhury, A. An analytical model for the prediction of the vibration response of rolling element bearings due to a localized defect. *Journal of Sound and Vibration 205*, 3 (1997), 275–292.

[76] Tenhunen, A., Benedetti, T., Holopainen, T. P., and Arkkio, A. Electromagnetic forces of the cage rotor in conical whirling motion. *IEE Proceedings Electric Power Applications 150*, 5 (2003), 563–568.

[77] Tenhunen, A., Holopainen, T. P., and Arkkio, A. Impulse method to calculate the frequency response of the electromagnetic forces on whirling cage rotors. *Electric Power Applications, IEE Proceedings – 150*, 6 (2003), 752–756.

[78] Van der Giet, M., Schlensok, C., Schmulling, B., and Hameyer, K. Comparison of 2-D and 3-D coupled electromagnetic and structure-dynamic simulation of electrical machines. *IEEE Transactions on Magnetics 44*, 6 (2008), 1594–1597.

[79] Wang, J., Jewell, G. W., and Howe, D. A general framework for the analysis and design of tubular linear permanent magnet machines. *IEEE Transactions on Magnetics 35*, 3 (1999), 1986–2000.

[80] Yeh, H.-F., and Dopker, B. Deformation mode selection and mode orthonormalization for flexible body system dynamics. *Computers & Structures 34*, 4 (1990), 615–627.

[81] Yin, M., Li, G., Zhou, M., and Zhao, C. Modeling of the wind turbine with a permanent magnet synchronous generator for integration. In *IEEE Power Engineering Society General Meeting* (2007).

[82] Yoo, W. S., and Haug, E. J. Dynamics of flexible mechanical systems using vibration and static correction modes. *Journal of Mechanisms Transmissions and Automation in Design 108*, 3 (1986), 315–322.

[83] Zhu, Z. Q., and Howe, D. Electrical machines and drives for electric, hybrid, and fuel cell vehicles. *Proceedings of the IEEE 95*, 4 (2007), 746–765.

ACTA UNIVERSITATIS LAPPEENRANTAENSIS

553. LEHTOVAARA, MATTI. Commercialization of modern renewable energy. 2013. Diss.

554. VIROLAINEN, SAMI. Hydrometallurgical recovery of valuable metals from secondary raw materials. 2013. Diss.

555. HEINONEN, JARI. Chromatographic recovery of chemicals from acidic biomass hydrolysates. 2013. Diss.

556. HELLSTÉN, SANNA. Recovery of biomass-derived valuable compounds using chromatographic and membrane separations. 2013. Diss.

557. PINOMAA, ANTTI. Power-line-communication-based data transmission concept for an LVDC electricity distribution network – analysis and implementation. 2013. Diss.

558. TAMMINEN, JUSSI. Variable speed drive in fan system monitoring. 2013. Diss.

559. GRÖNMAN, KAISA. Importance of considering food waste in the development of sustainable food packaging systems. 2013. Diss.

560. HOLOPAINEN, SANNA. Ion mobility spectrometry in liquid analysis. 2013. Diss.

561. NISULA, ANNA-MAIJA. Building organizational creativity – a multitheory and multilevel approach for understanding and stimulating organizational creativity. 2013. Diss.

562. HAMAGUCHI, MARCELO. Additional revenue opportunities in pulp mills and their impacts on the kraft process. 2013. Diss.

563. MARTIKKA, OSSI. Impact of mineral fillers on the properties of extruded wood-polypropylene composites. 2013. Diss.

564. AUVINEN, SAMI. Computational modeling of the properties of TiO2 nanoparticles. 2013. Diss.

565. RAHIALA, SIRPA. Particle model for simulating limestone reactions in novel fluidised bed energy applications. 2013. Diss.

566. VIHOLAINEN, JUHA. Energy-efficient control strategies for variable speed controlled parallel pumping systems based on pump operation point monitoring with frequency converters. 2014. Diss.

567. VÄISÄNEN, SANNI. Greenhouse gas emissions from peat and biomass-derived fuels, electricity and heat – Estimation of various production chains by using LCA methodology. 2014. Diss.

568. SEMYONOV, DENIS. Computational studies for the design of process equipment with complex geometries. 2014. Diss.

569. KARPPINEN, HENRI. Reframing the relationship between service design and operations: a service engineering approach. 2014. Diss.

570. KALLIO, SAMULI. Modeling and parameter estimation of double-star permanent magnet synchronous machines. 2014. Diss.

571. SALMELA, ERNO. Kysyntä-toimitusketjun synkronointi epävarman kysynnän ja tarjonnan toimintaympäristössä. 2014. Diss.

572. RIUNGU-KALLIOSAARI, LEAH. Empirical study on the adoption, use and effects of cloud-based testing. 2014. Diss.

573. KINNARINEN, TEEMU. Pressure filtration characteristics of enzymatically hydralyzed biomass suspensions. 2014. Diss.

574. LAMMASSAARI, TIMO. Muutos kuntaorganisaatiossa – tapaustutkimus erään kunnan teknisestä toimialasta. 2014. Diss.

575. KALWAR, SANTOSH KUMAR. Conceptualizing and measuring human anxiety on the Internet. 2014. Diss.

576. LANKINEN, JUKKA. Local features in image and video processing – object class matching and video shot detection. 2014. Diss.

577. AL-SAEDI, MAZIN. Flexible multibody dynamics and intelligent control of a hydraulically driven hybrid redundant robot machine. 2014. Diss.

578. TYSTER, JUHO. Power semiconductor nonlinearities in active d*u*/d*t* output filtering. 2014. Diss.

579. KERÄNEN, JOONA. Customer value assessment in business markets. 2014. Diss.

580. ALEXANDROVA, YULIA. Wind turbine direct-drive permanent-magnet generator with direct liquid cooling for mass reduction. 2014. Diss.

581. HUHTALA, MERJA. PDM system functions and utilizations analysis to improve the efficiency of sheet metal product design and manufacturing. 2014. Diss.

582. SAUNILA, MINNA. Performance management through innovation capability in SMEs. 2014. Diss.

583. LANA, ANDREY. LVDC power distribution system: computational modelling. 2014. Diss.

584. PEKKARINEN, JOONAS. Laser cladding with scanning optics. 2014. Diss.

585. PELTOMAA, JYRKI. The early activities of front end of innovation in OEM companies using a new FEI platform as a framework for renewal. 2014. Diss.

586. ROZHANSKY, IGOR. Resonant tunneling effects in semiconductor heterostructures. 2014. Diss.

587. PHAM, THUY DUONG. Ultrasonic and electrokinetic remediation of low permeability soil contaminated with persistent organic pollutants. 2014. Diss.

588. HOKKANEN, SANNA. Modified nano- and microcellulose based adsorption materials in water treatment. 2014. Diss.

589. HINKKANEN, JUHA. Cooperative strategy in emerging markets – analysis of interfirm R&D cooperation and performance in Russian manufacturing companies. 2014. Diss.

590. RUSKOVAARA, ELENA. Entrepreneurship education in basic and upper secondary education – measurement and empirical evidence. 2014. Diss.

591. IKÄHEIMONEN, TUULI. The board of directors as a part of family business governance – multilevel participation and board development. 2014. Diss.

592. HAJIALI, ZUNED. Computational modeling of stented coronary arteries. 2014. Diss.

593. UUSITALO, VILLE. Potential for greenhouse gas emission reductions by using biomethane as road transportation fuel. 2014. Diss.

594. HAVUKAINEN, JOUNI. Biogas production in regional biodegradable waste treatment – possibilities for improving energy performance and reducing GHG emissions. 2014. Diss.